Investigation of Electrophysiological Interactions in the Human Heart

UNIVERSITY COLLEGE LONDON

DEPARTMENT OF MECHANICAL ENGINEERING

Author: Lei Xu Supervisor: Dr. Ben Hanson

Thesis submitted for the degree of MPhil

August 2, 2013

Declaration

I, Lei Xu confirm that the work presented in this thesis is my own. Where information has been derived from other sources, I confirm that this has been indicated in the thesis.

Signed by: Lei Xu

Acknowledgment

I'd like to thank my supervisor Dr. Ben Hanson and second supervisor Dr. Vanassa Diaz, who have given me not only endless help and acute criticism but also boundless encouragement. Thanks are also given to Dr. Malcolm Finlay, Dr. Peter Taggart, and Dr. Pier Lambiase from UCL Heart Hospital, who has provided me with a large amount of experimental data without which the work could never have been done. Special thanks to Malcolm Finlay, it is really a pleasure to work with him. Also, I am grateful to Dr. Ian Eames and Dr. Michael Curtis, who provided me invaluable advice and suggestions on my thesis.

Abstract

Ventricular fibrillation (VF) is the leading heart rhythm for causing sudden death worldwide, claiming 70,000 deaths per year in the UK alone. Understanding the mechanism for initiating fibrillation is crucial in progressing future therapies and risk stratification for implantable cardioverter-defibrillator therapy. Experimental studies and computerized simulations of cardiac activity have significantly contributed to the understanding of cardiac electrophysiology. Although these studies have been very successful at bridging the gap between basic research findings and understanding of arrhythmia, few studies have been made on the construction of an accurate simulation based on patient-acquired data. There remain some distances between computational modeling and clinical appreciation of arrhythmia generation.

The primary objective of this project was to develop new numerical procedures to carry out simulation studies based on patient-acquired data referring to the existing computational models. To achieve this objective, the research was divided into three parts: the first part is to create models for electrical restitution of cardiac tissue and conduction model of activation signal, which can be fitted with experimental data to obtain electrical restitution properties; the second approach is to validate the computational models on extra-stimuli demonstrating that accurate prediction can be made on complex interactions of the time dynamics of sequential premature beats; the last part is to carry out simulation studies focusing on initiation of functional block based on patient-specific computational models.

The main contribution of this work is that it provided a platform by which patient-specific experimental data can be incorporated into computerized simulation studies and served as a method by which the gap between fundamental cardiac simulation and clinical science can be bridged.

Contents

List of figures

List of tables

List of symbols

APD	Refractory period (action potential duration)
APD_{SS}	Steady-state APD
AT	Activation time
CI	Coupling interval
CV	Conduction velocity
CV_{SS}	Steady-state conduction velocity
DI	Diastolic interval
DI_{bound}	Biomarker for condition of functional block
EF	Ejection fraction
EDV	End-diastolic volume
ESV	End-systolic volume
$F(DI)$	Function for condition of functional block
$[Ca^{2+}]_i$	Intracellular calcium ion concentration
$[Ca^{2+}]_{ss}$	Concentration of calcium ion, in subspace compartment
$[Ca^{2+}]_{nsr}$	Concentration of calcium ion, in network SR compartment
$[Ca^{2+}]_{jsr}$	Concentration of calcium ion, in junctional SR compartment
$[Na^{+}]_i$	Intracellular sodium ion concentration
$[Na^{+}]_{ss}$	Concentration of sodium ion, in subspace compartment

$[K^+]_i$: Intracellular potassium ion concentration

$[K^+]_{ss}$ Concentration of potassium ion, in subspace compartment

I_{Na} Na^+ current

m Activation gate for fast I_{Na}

h_{fast} Fast development of inactivation gate for fast I_{Na}

h_{slow} Slow development of inactivation gate for fast I_{Na}

j Recovery from inactivation gate for fast I_{Na}

$h_{CaMK,slow}$ Slow development of inactivation gate for CaMK phosphorylated I_{Na}

j_{CaMK} Recovery from inactivation gate for CaMK phosphorylated I_{Na}

m_L Activation gate for late I_{Na}

h_L Inactivation gate for late I_{Na}

$h_{L,CaMK}$ Inactivation gate for CaMK phosphorylated I_{Na}

I_{to} Transient outward K^+ current

a Activation gate for I_{to}

i_{fast} Fast inactivation gate for I_{to}

i_{slow} Slow inactivation gate for I_{to}

a_{CaMK} Activation gate for CaMK phosphorylated I_{to}

$i_{CaMK,\,fast}$ Fast inactivation gate for CaMK phosphorylated I_{to}

$i_{CaMK,slow}$ Slow inactivation gate for CaMK phosphorylated I_{to}

I_{CaL} Ca^{2+} current through the L-type Ca^{2+} channel

d Activation gate for I_{CaL}

f_{fast} Fast voltage dependent inactivation gate for I_{CaL}

f_{slow} Slow voltage dependent inactivation gate for I_{CaL}

$f_{Ca,\,fast}$ Fast development of Ca^{2+} dependent inactivation gate for I_{CaL}

$f_{Ca,slow}$ Slow development of Ca^{2+} dependent inactivation gate for I_{CaL}

j_{Ca} Recovery from Ca^{2+} dependent inactivation gate for I_{CaL}

n Fraction in Ca^{2+} dependent inactivation mode for I_{CaL}

$f_{CaMK,\,fast}$ Fast development of Ca^{2+} dependent inactivation gate for CaMK phosphorylated I_{CaL}

$f_{Ca,CaMK,\,fast}$ Slow development of Ca^{2+} dependent inactivation gate for CaMK phosphorylated I_{CaL}

I_{Kr} Rapid delayed rectifier K^+ current

$x_{r,\,fast}$ Fast activation/deactivation gate for I_{Kr}

$x_{r,slow}$ Slow activation/deactivation gate for I_{Kr}

I_{Ks} Slow delayed rectifier K^+ current

x_{s1} Activation gate for I_{Ks}

x_{s2} Deactivation gate for I_{Ks}

I_{K1} Inward rectifier K^+ current

x_{K1} Inactivation gate for I_{K1}

$J_{rel,NP}$ Non-phosphorylated Ca^{2+} release, via ryanodine receptors, from jsr to myoplasm

$J_{rel,CaMK}$ CaMK phosphorylated Ca^{2+} release, via ryanodine receptors, from jsr to myoplasm

$CaMK_{trap}$ Fraction of autonomous CaMK binding sites with trapped calmodulin

RT Repolarisation time

SV Stroke volume

V Membrane voltage

1 Introduction

The cardiovascular system is formed by the heart and blood vessels; coordinated beating activity enables the heart to act as a pump, transporting oxygen, nutrients, waste products and heat around the body via the blood. The mechanical activity of the heart is driven by electrical activity: a propagating electrical impulse (the action potential) generated triggers mechanical contraction; this action potential (AP) is conducted from cell to cell via intracellular gap junctions, forming electrical waves that activate and synchronize the pumping action of the heart. Any interruption to the repetitive cardiac function can lead to failure to act as an effective pump, and ultimately cause death.

The most common scenario where such disorder of electrical activity of the ventricles may occur is during cardiac ischemia, a narrowing or occlusion of coronary arteries causes a reduction in blood supply to regions of myocardium. In patients with cardiac ischemia, potential differences between ischemic and normal region allow “injury currents” to flow at the border zone between regions. These currents, caused by the potential differences between the two areas, allow resting depolarization and spontaneous cardiac activity, a chief trigger of tachyarrhythmias in myocardial infaction. Later, scar formation in the area of infracted tissue causes interruption of normal electrical conduction, this can manifest as substrate for abnormal conduction patterns, particularly re-entry. Cardiac ectopic activity such as ventricular premature beat (VPB) and ventricular tachycardia (VT), is common after an acute myocardial infarction (Ahuja et al., 1968). In more imminently dangerous situation, ventricular fibrillation (VF) can develop; the chaotic electrical activity destroys the coherent contraction of the ventricular muscle and its pumping function. This results in death within minutes unless the arrhythmia is immediately controlled (e.g. by defibrillation therapy).

The mechanisms of clinical ventricular arrhythmias have been difficult to investigate by clinical studies on patients, because arrhythmias usually occur before patient arrives at hospital. Even if arrhythmia occurs during hospital admission, the primary concern is resuscitation rather than arrhythmogenesis studies. The development of animal models has partially overcome this limitation of clinical studies, and provided invaluable insight into electrophysiological changes associated with cardiac ischemia and how they initiate ventricular tachycardia and fibrillation (Wit and Janse, 1992, Carmeliet, 1999). However, animal models have certain limitations. For instance, species difference means even mammalian animal models are different from human heart in terms of size and pressure, as well as ion channel expression etc. Also, limitations of current experimental techniques for electrical recording lead to insufficient spatial resolution within ventricular wall (Rodriguez et al., 2006b), proposing the question of whether the electrophysiological behaviour within ventricular wall can be simulated using computational models.

In order to further the knowledge of the mechanism of cardiac arrhythmia, computational models have been developed at all levels: from ion channel to cell to whole heart. At the cellular level, the AP was first described using computational models by Hodgkin and Huxley (Hodgkin and Huxley, 1952) for the nerve axon. Hodgkin and Huxley made a fundamental stride in describing the voltage-dependent conductance change in excitable cells using the voltage-clamp technique on the nerve axon. Their experiments showed that the inward sodium (Na^+) current is responsible for depolarization while the outward potassium (K^+) current leads to repolarisation to the resting potential. Based on Hodgkin-Huxley model, McAllister et al. (McAllister et al., 1975) constructed the first cardiac AP models for the Purkinje fibre, while Beeler and Ruter (Beeler and Reuter, 1977) formulated the first cardiac AP models for ventricular myocyte. For these first generation cardiac AP models, it was assumed that intracellular ion concentration remained constant during AP. However, in myocyte, intracellular ion concentration does change during AP (e.g. when cells are paced at a high rate).

The first model taking detailed information of intracellular ion concentration changes into consideration was the DiFrancesco-Noble model (DiFrancesco and Noble, 1985) of the Purkinje fibre AP; similar models were formulated by Rasmusson et al. (Rasmusson et al., 1990) for the bullfrog atrial cell; the Luo-Rudy dynamic (LRd) model (Luo and Rudy, 1994) described these process for a guinea pig ventricular AP. These 'second generation' AP models were widely used to carry out detailed mechanistic study of phenomena including the effect of drugs on specific ion channels (Clancy and Rudy, 1999, Clancy and Rudy, 2001), the mechanism of after-depolarization (Faber and Rudy, 2000), and the development of regional ischemia (Shaw and Rudy, 1997).

At the tissue level, computational models can be divided into two types: monodomain models and biodomain models. The Monodomain model assumes that the tissue behaves as an excitable medium, while biodomain model consider the tissue as two-phase medium comprising intracellular and extracellular spaces. The AP models at tissue level are of monodomain type: the Hodgkin-Huxlexy model provides one-dimensional conduction analysis; Luo-Rudy model includes two-dimensional conduction. Monodomain models are widely used for simulation of wave propagation in the heart. Compared with monodomain models, biodomain models are more complicated and are mostly based on finite element analysis (Vigmond et al., 2002). Although biodomain models are more computational expensive, they provide a more detailed description of the tissue (Austin et al., 2006).

At the whole ventricle level, the modelling process requires the detailed geometry and fibre orientation information, which can be obtained by high-resolution dissection and histology or high-resolution magnetic resonance imaging (MRI). The most commonly used models include: rabbit ventricle (Vetter and McCulloch, 1998), canine ventricle (Nielsen et al., 1991), pig ventricle (Stevens et al., 2003). These models have been widely used for the purpose of arrhythmia studies: the canine ventricle model was used to simulate re-entry VF (Berenfeld

and Pertsov, 1999, Clayton and Holden, 2002, Panfilov, 1999, Xie et al., 2004) and a rabbit ventricle model used to study the mechanism of arrhythmia (Cherry and Fenton, 2004, Rogers, 2002), and defibrillation (Rodriguez et al., 2006a, Trayanova, 2006).

The existing computational models provided invaluable insight into the mechanism of cardiac arrhythmia. However, most computational models are not suitable for the purpose of developing towards individual patient analysis, due to their being either computational highly expensive or their requiring impossibly high resolution detail of the heart to be studied. For example, cardiac cell models were developed principally based on the Hodgkin-Huxley formulation, in which ion channel dynamics can be modeled using 'gating variables' that are functions of potential and represent the open probability of any given ion channel. The first generation of cardiac cell models only included two or three variables, but as more ion channels were discovered, large numbers of nonlinear ordinary differential equations (ODEs) were introduced into these models (e.g. Nobel et al. (Noble et al., 1998), included 23 ODEs). Although the individual solution for each ODE can be computed very quickly, the number of individual complex cell models can rise to enormous numbers when simulation is required in a tissue or organ level model.

Furthermore, most computational models were developed based on experimental data acquired in-vitro. Simulation studies based on these computational models may not be an accurate representation of behavior observed in-vivo. For instance, three-dimensional simulations were carried out based on anatomic canine ventricular models or a human ventricular model. Based on these simulations, wave-break and re-entry could be simulated, furthering the understanding of ventricular arrhythmia. However, for individual patients, the existing models may not accurately predict patterns of conduction in a given in-vivo heart. The anatomy and geometry are acquired using magnetic resonance imaging (MRI), but many of the parameters of existing models used describe the function of ion channels, pumps, and

exchangers cannot be measured in a 3D ventricular mass, which in practice will exhibit local variation, remaining unaccounted for in the model (Clayton and Panfilov, 2008). It is frequent that such parameters use data acquired experimentally from other species. Also, the experimental settings (such as temperature, stable voltage clamp conditions) for obtaining parameters will be different from the in-vivo heart.

As discussed above, a large body of work exists in modeling cardiac electrophysiological behavior. This has provided fairly detailed information about mechanisms of arrhythmia. Yet, there is a gap between the existing modeling techniques and patient-specific analysis. The patient-specific analyses in this thesis refer to electrophysiological studies (EPS) that are carried out on patients who have already been identified as suffering from cardiac arrhythmia. Currently, EPS are frequently used in the clinical diagnosis of arrhythmia. Treatments may be influenced as a result of these studies (e.g. decision for ablation and medical treatment, as well as influencing decisions regarding implantable cardioverter defibrillator (ICD) therapy). Simulations studies based on EPS could provide the clinical electrophysiologist with a more detailed assessment of a patient's arrhythmia, perhaps without even requiring tachycardia initiation. Simulation studies could also be used to identify the site where therapy (e.g. ablation therapy) is needed based on predicted electrophysiology properties, rather than relying on the direct observation of abnormal electrical conduction during an arrhythmia.

It is therefore crucial to find an effective way to combine computational models with patient-specific measurements. The computational models obtained from patient-specific measurements could give the cardiologist novel insights into the mechanisms of their patients' ventricular arrhythmia and possibly provide a simple computational biomarker, used to influence drug treatment or ICD implantation decision making. Besides, such studies may allow new investigations into mechanisms of ventricular arrhythmia in specific diseases by comparing different patient groups.

1.1 Objectives of the research

This research investigates the electrophysiological behavior of human ventricle, especially the abnormal electrical conduction behavior that may lead to ventricular arrhythmia. As later shown (Chapter 2), very little prior work has been done in carrying out computational studies based on human in-vivo experiments. Existing computational models have certain limitations that may restrict their use on patient-specific studies. The biggest of these is parameter acquisition: on one hand some parameters are hard to obtain; on the other parameters may exhibit local variation, which certainly increases both uncertainty and complexity of the modeling process. There exists a gap between existing computational models and patient-specific analysis, which is critical in terms of identifying arrhythmia risks, preventing arrhythmia, and providing a solution for specific patient. Further development of the existing computational models is required for this purpose. Consequently, the aims of this thesis are to:

I. Review existing computational models, and identify the specific improvements required for existing models which would allow them to be used on patient-specific studies.

II. Create analytical models to represent local electrophysiology based on experimental measurements from human patients.

III. Develop software tools for carrying out simulation studies using computational models based on experimental human data, and for interpretation of the simulation result.

IV. Evaluate the accuracy of the computational models by simulating experimental protocols and comparing to measured data in-vivo.

V. Use patient-specific computational models based on in-vivo data to evaluate the validity of existing hypotheses about ventricular arrhythmia.

VI. Use patient-specific computational models to simulate the effect of a variety of arrhythmic scenarios, including rapid beat intervals, in order to access patient-specific risk and to identify how local electrophysiological properties relate to potential arrhythmic risk.

VII. Investigate the feasibility of creating a simple computational biomarker based on patient-specific electrophysiology to predict risk of ventricular arrhythmia.

VIII. Further validate and refine computational models and simulation techniques using experimental data from patient group having pharmacological intervention (ajmaline) and disorder of the myocardium such as arrhythmogenic right ventricular cardiomyopathy (ARVC).

1.2 Scope of the research

In this project, clinically acquired data was used to observe and explain the complex interactions of activation and repolarisation arise from sequential extra-stimuli. All the experimental works were carried out by professional cardiologists, which were not included in this project. The work presented in this work focused on analyses of the experimental data, modeling restitution properties, and simulation studies. The experimental data was acquired as part of the normal clinical procedure, some of which have been used for separate studies (Hanson et al., 2009, Lambiase et al., 2009, Gomes et al., 2012). All the experimental data used in this project was under the permission of the investigators.

The computational models used assumed the electrophysiological properties are uniform along the conduction pathway of the investigated electrode. This is a simplified model compared to the physiological situation, which inevitably include different types of cardiac cells (Purkinje fibre, normal ventricular cell, bundle of His, etc.) on the conduction pathway.

The slowed-down conduction velocity investigated only reflects the decrease in conduction velocity around the area very close to the pacing site where the electrical stimulus is given. The decrease cannot indicate how conduction velocity can be changed on the site far away from the pacing site. This means the simulation can only be done under the situation of pacing from the same site. It could be improved by pacing from different site during the experiment.

Moreover, one dimensional conduction simulation can only simulate activation conduction along a one dimensional conduction pathway. However, in the real situation the activation conduction occurs in a three dimensional tissue, which means the activation signal is not only conducted along the cardiac fibre but across the fibre. Especially when functional block is initiated on the original conduction pathway, the activation signal will be conducted from its neighbouring region. The one dimensional simulation study can only show functional block but could not simulate the activation conduction after the block. Consequently, this technique can predict block, which is risky, but cannot predict whether the block can develop into VF.

1.3 Organization of the thesis

This thesis has the following structure:

Chapter 2 provided a review of ventricular arrhythmia, including the mechanism for ventricular arrhythmia. This chapter evaluated existing computational models and techniques for studying ventricular arrhythmias, and reveals the limitations of previous work. The later part of this chapter indentified how the existing computational models and techniques can be further developed by incorporating human in-vivo experiments in order that the models may better-represent real human in-vivo behavior.

Chapter 3 briefly described the sources of experimental data, and the techniques used for experimental data analysis.

Chapter 4 described the development of computational models employed in this research to model cardiac electrical properties. These models included APD restitution model, CV restitution model, and a one-dimensional conduction model. A biomarker for predicting risk for ventricular arrhythmia was introduced in this chapter based on cardiac electrical properties. Also, the influence of ventricular cellular electrophysiological properties on APD restitution properties were discussed at the end of this chapter aiming to provide a practical method to fit the ion channel model with experimental data of APD restitution.

Chapter 5 presented the results of computational studies. By comparing the simulation result for the extra-stimuli with the experimental data, the accuracy of the computational models on predicting time kinetics of extra-stimuli was investigated.

Chapter 6 offered insights into the existed hypothesis about ventricular arrhythmia by carrying out simulation studies using the cardiac electrical properties obtained from experimental data. The biomarker for predicting cardiac arrhythmia risk was presented as an example of application on pharmaceutical testing (effect of ajmaline drug).

Chapter 7 summarized the conclusions of the computational model enhancements, the simulation studies, and evaluation of the work. Suggestions were made for further development of the technique and computational models in future work.

2 Literature Review

2.1 Introduction

A multitude of studies have been performed aiming to investigate both the mechanical and electrical behavior of the heart, which could in turn be used to study the mechanism of cardiac arrhythmia. Application of computational models has enabled detailed insight into the cardiac electrophysiological behavior. These have greatly increased the body of knowledge regarding mechanisms of cardiac arrhythmia. However, when it comes to clinical investigations, patient-specific analysis is highly restricted, commonly only the electrocardiogram (ECG) analysis and EPS are used as electrophysiological investigations, both of which have very limited ability to correctly risk stratify for cardiac arrhythmia, especially for lethal arrhythmias such as VF. In practice, assessments of cardiac pumping function are used to guestimate risk based on overall cardiac damage. There is thus proposes a gap between theoretically well established computational models and patient-specific analysis. To help to describe the mechanism of cardiac arrhythmias, basic mechanical and electrical behaviors of the heart are introduced in section 2.2.

In section 2.3, details about different hypotheses of ventricular fibrillation were reviewed, including their mechanism, techniques currently used for diagnosing arrhythmia, and therapies used. Cardiac arrhythmia can be divided into two types: non-reentrant arrhythmia (AV heart block, electrical alternant, etc) and reentrant arrhythmia. This thesis focuses on reentrant arrhythmia (ventricular tachycardia, ventricular fibrillation, etc). The most commonly acknowledged mechanisms for reentrant arrhythmia include heterogeneity of electrophysiological properties and activation/repolarisation interactions. As stated previously, various approaches such as animal models and computational models have been used to investigate the mechanisms of arrhythmia. With the fast development of computing

technologies, computational models have been widely used in modeling electrophysiological behavior of the heart from cellular level to organ level. The most commonly used computational models are reviewed in section 2.4, aiming to answer 4 questions: how are the models constructed; what are the results of computational modeling; what are their limitations; how can they be linked with EPS.

The concluding section 2.5 highlights the new aspects of the research relating the current techniques used to diagnose arrhythmia and existing computational models. The conclusion also includes achievements that could be done using the new techniques and models.

2.2 Mechanical and Electrical Behaviour of the Heart

The heart lies obliquely across the midline of the chest, and consists of four chambers: two atria and two ventricles (Figure 2.1). The basic function of the heart is to act as a pump that transports oxygen, nutrients, waste products and heat around the body via the blood. During the pumping process, the ventricles are filled from the atria, acting as contractile reservoirs. The right ventricle pumps deoxygenated blood through the pulmonary trunk to the lungs, after which the oxygenated blood from the lungs returns to the left atria. This relatively short and low pressure (around 15 mmHg) circulation is called pulmonary circulation. Filled through left atrium, the left ventricle pumps oxygenated blood to the tissues of the body. The tissues extract some of the oxygen, and the partly deoxygenated blood returns to the right atrium via two great veins, the superior vena cava and interior vena cava. This systemic circulation takes place at high pressure (around a mean of 90 mmHg) through the arterial system. The heart valves allow the ventricles to act as an effective pump. Corresponding to the pressure difference of the two circulations, the left ventricular wall is thicker than the right ventricular wall, which allows the left ventricular wall to generate more contractile force than the right ventricular wall.

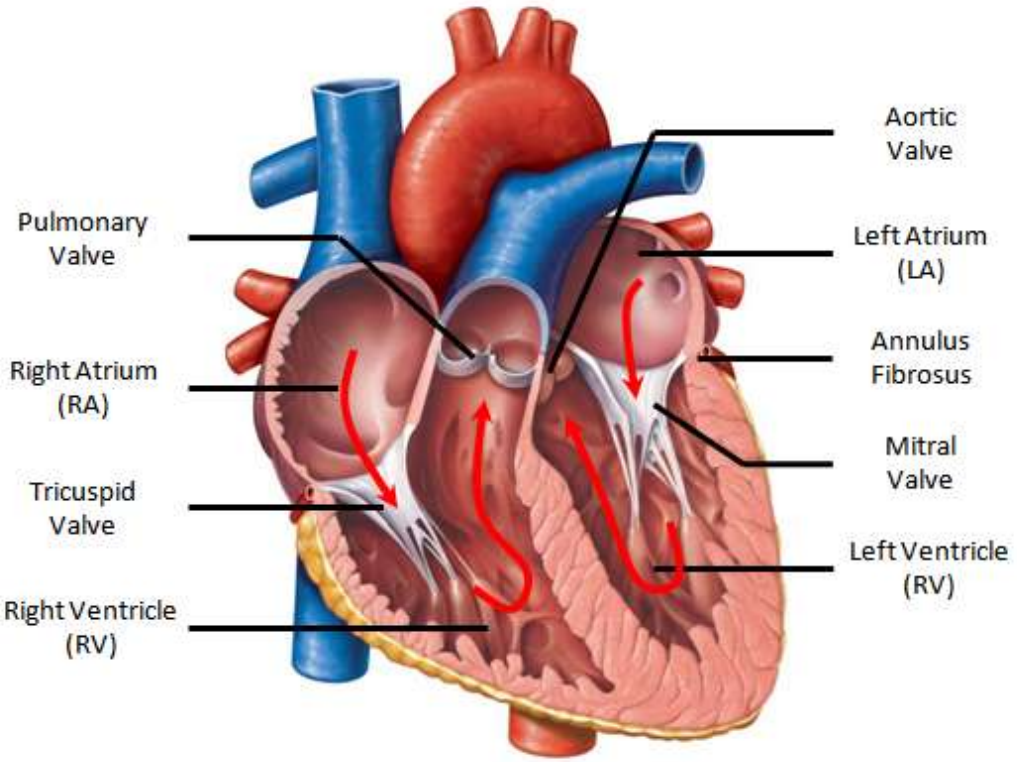

Figure 2.1: Structure of the heart (Red arrows indicate the direction of the blood flow). (The picture of the heart was obtained from online resource: http://www.tutorvista.com)

The pumping activity of the heart can be divided into two parts depending on their function: mechanical behavior and electrical behavior. The mechanical behavior refers to the contraction process generated by the cardiac muscle, which result in the pressure changes inside the heart and enables the blood flow; the electrical behavior act as the control mechanism for the mechanical behavior in terms of its timing. The mechanical behavior and electrical behavior can influence each other through a phenomenon called mechanoelectrical feedback (Kohl and Sachs, 2001). The mechanical behavior has been studied in detail over the last few centuries with pressure changes (Noble, 1968) and pressure-volume analysis (Burkhoff et al., 2005, Baan et al., 1984). The electrical behavior of the heart, on the other hand, has not

been fully studied, especially the abnormal electrical behavior responsible for causing arrhythmia.

2.2.1 Mechanical Behavior of the Heart

The pumping behavior of the heart consists of precisely timed electrical and mechanical behaviors that are responsible for rhythmic heart contraction. Figure 2.2 showed the pressure changes in the left-side chambers of the heart. Systole refers to the contraction of the ventricle; while diastole indicates ventricular relaxation and filling. During diastole, blood flows from atria to ventricle after mitral valve (MV) opens, which lead to a rapid filling process and a slow filling process afterward. In later stage of diastole, atrial contraction (phase 1) as indicated by the *a* wave in the atrial pressure curve, pushes an extra amount of blood into the ventricle (about 10% of ventricular filling at rest). However, this extra amount of blood can be increased up to 40% of ventricular filling during excise, because the time for passive ventricular filling process will be shortened as heart rate is increased.

After the atrial contraction, the ventricle starts to contract, which consequently increases the pressure rapidly within the ventricle. Mitral valve is forced to close after the pressure in the ventricle exceeds atrial pressure. As the ventricular pressure rise further, it exceeds the pressure within aorta, forcing the aortic valve (AV) open, after which blood starts to flow from the ventricle into aorta. At the end of ventricular ejection, ventricular pressure falls below aortic pressure, and consequently forces aortic valve to close. Following this process, ventricular pressure continues to fall during its relaxation phase. As it drops below atrial pressure, the mitral valve opens, which initiate diastolic ventricular filling and repetition of the cycle described above.

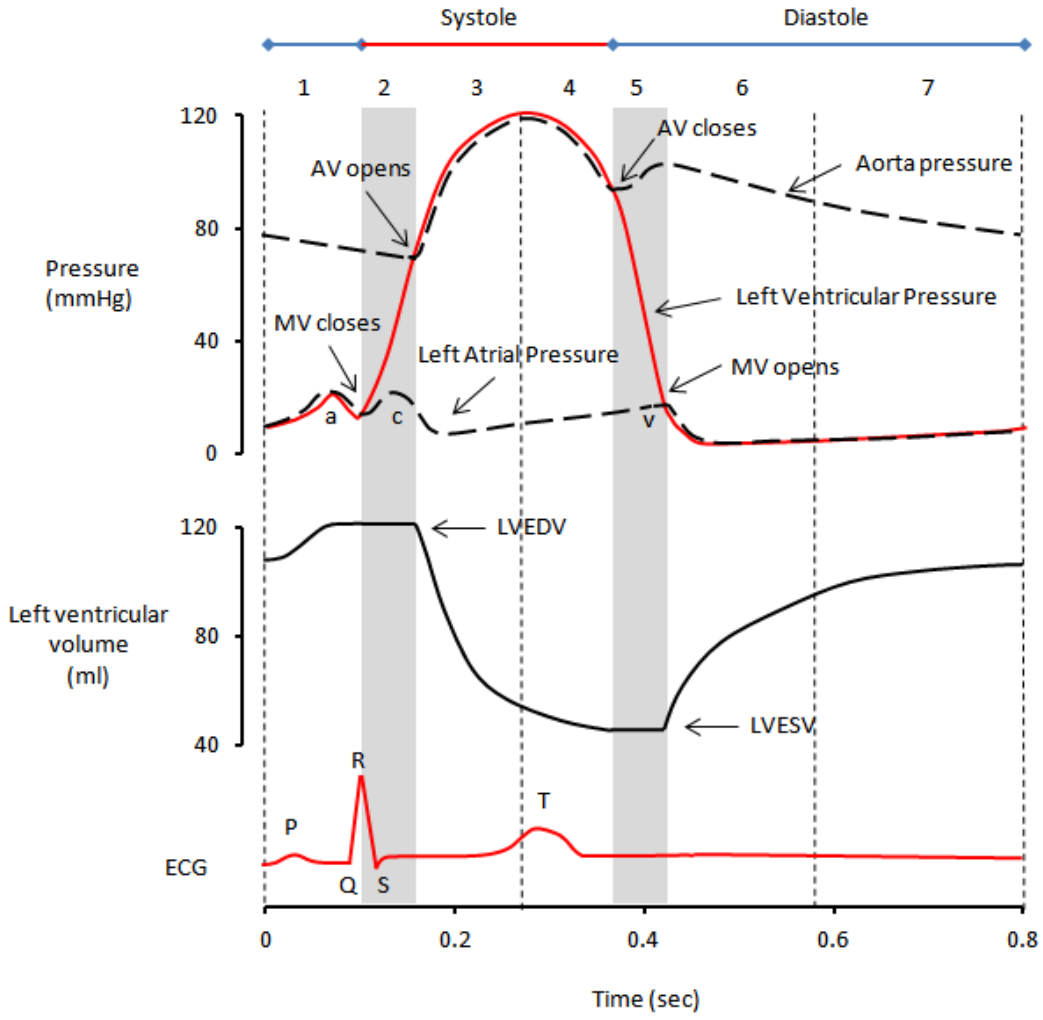

Figure 2.2: The normal cardiac cycle, showing pressure relationships between the left-sided heart chambers. Phase 1 indicates contraction of left atrium (LA); phase 2 shows the isovolumic ventricular contraction (mitral valve (MV) and aortic valve (AV) are both closed); phase 3 is the rest period of ventricular contraction after isovolumic contraction; phase 4 is the first half of ventricular relaxation before AV closes; phase 5 shows the isovolumic ventricular relaxation process (MV and AV are both closed); phase 6 is the rapid ventricular fill process; phase 7 is the slow ventricular filling process; in phase 1, 6, and 7, ventricular pressure is roughly the same with atrial pressure because MV is open; during phase 3 and 4, ventricular pressure is roughly the same with aortic pressure due to opening of AV; LVEDV: left ventricular end-diastole volume; LVESV: left ventricular end-systole volume.

Notably, there are two positive waves on the atrial pressure curve despite *a* wave: c wave indicates the small increase in atrial pressure after mitral valve is closed; *v* wave is the result of passive atrial filling from veins. Figure 2.2 describes the pressure change in left side of the heart. The right side of the heart has similar patterns but lower pressures (systolic: 15-30mmHg in right ventricle, 100-140mmHg in left ventricle).

Early researchers depended largely on the pressure changes to study the behavior of the heart. For example, the ejection fraction (EF), defined as fraction of blood ejected by the ventricle relative to its filled volume (end-diastolic volume (EDV)), is used as a measure of the ability of the heart to eject blood. EF can be expressed as below:

$$EF = \frac{SV}{EDV} = \frac{EDV - ESV}{EDV} \tag{2.1}$$

Where, SV is the stroke volume; ESV is the end-systolic volume. As shown in Figure 2.2, *EDV-ESV* indicates volume of blood ejected by the ventricle (stroke volume). EF is normally about 0.5-0.65. Typically, cardiac arrhythmia such as myocardial infarction and atrial fibrillation have a great influence on the pumping function of the heart and consequently result in decrease in EF, likewise reduction of EF often reflects preexisting cardiac disease and thus acts as a marker for predisposition to cardiac arrhythmia. Many clinical researches (Moss et al., 2002, Zornoff et al., 2002, Owan et al., 2006, Shah et al., 1980) used EF as a standard to separate different group of patients. However, recent researches (Owan et al., 2006, Bhatia et al., 2006) indicated that preserved EF does not mean free of risk for heart failure.

Research (Mason et al., 1971) indicated that the first derivative of systolic ventricular pressure curve (dp/dt) is greatly influenced by the myocardial contractility, which represents the intrinsic ability of the myocardium to contract. Therefore, the maximum dp/dt (dp/dt_{max}) was widely used as a fundamental property of myocardium related with contractility in early

researches (Mason et al., 1971, Taylor et al., 1968, Parmley et al., 1972). Studies (Kass and Maughan, 1988) showed that dp/dt_{max} decreases as EDV is decreased (Figure 2.3 (C)).

Another method for studying the mechanical behavior of the heart is to relate ventricular pressure change and volume change. The pressure-volume relationship can be divided into four parts depending on the open-closure state of the valves: isovolumetric contraction, ejection phase, isovolumetric relaxation, filling phase (Figure 2.3 (A)). The area of the pressure-volume loop represents the stroke work, which is the energy generated by the ventricle within one cardiac cycle. Similar to dp/dt_{max}-EDV relationship, the stroke work decreases as EDV is decreased (Figure 2.3 (C)). The relationship between stroke work and EDV is used clinically as an index of contractility. When EDV is changed, there's another linear relationship between the end-systolic pressure (ESP) and ESV as shown by the dashed line in Figure 2.3 (B).

In early studies, the pressure-volume relationships have been extensively used on cardiac surgical patients. Pressure-volume loops have been used to evaluate ventricular function after heart transplant (von Scheidt et al., 1991). In addition, the stroke work has been used to investigate changes in cardiac function after valve replacement (Harpole et al., 1989) or valvuloplasty (Harpole et al., 1990). For ESP-ESV relationship, Kass et al. indicated that ventricular hypertrophy depresses the slope of ESP-ESV relationship(Kass et al., 1988), pacing-induced ischemia can reduce the slope of ESP-ESV relationship (Spaccavento et al., 1990); indeed, a complex polynomial relationship exists between ESP-ESV relationship and EF(Starling et al., 1988).

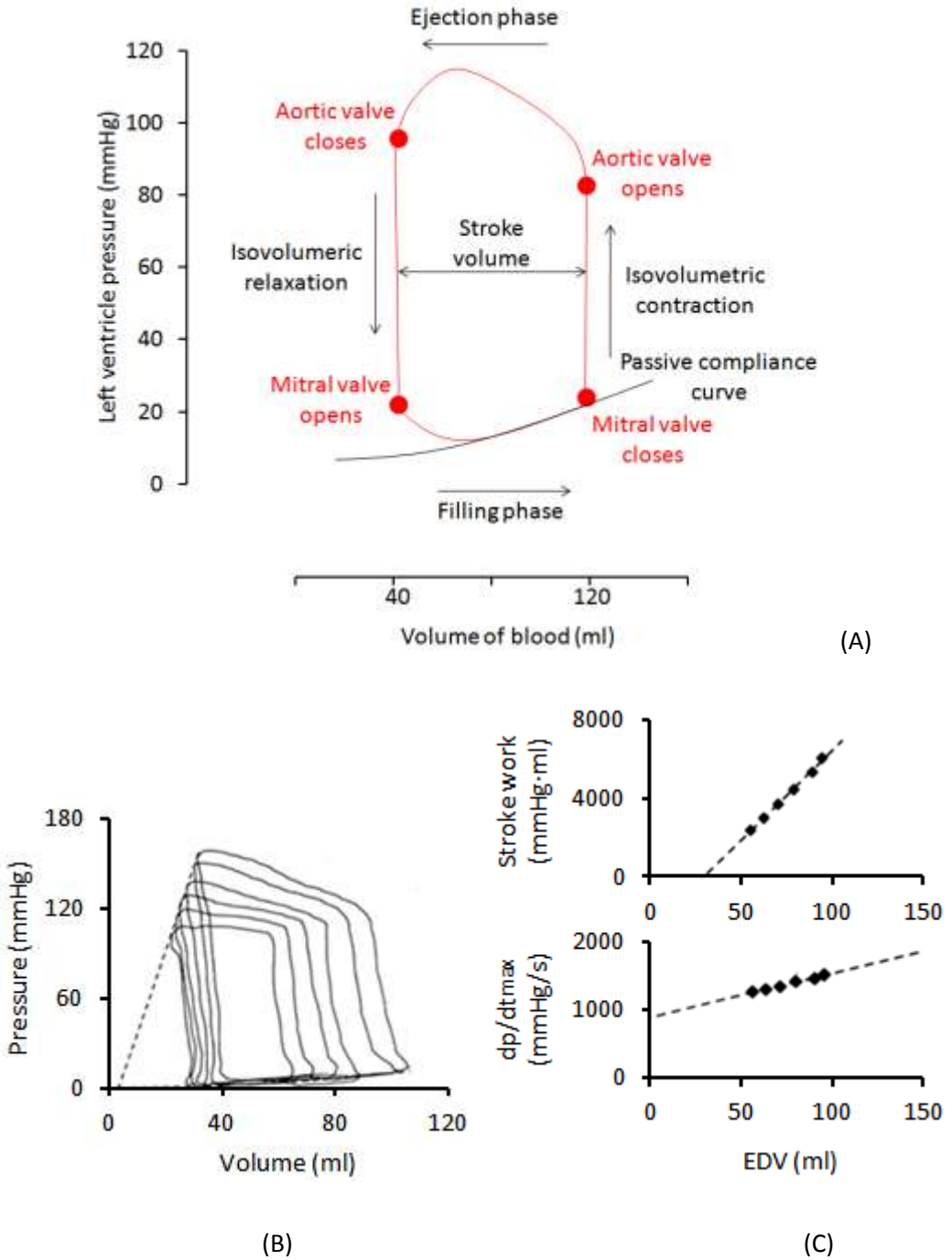

Figure 2.3: Pressure-volume cycle of left ventricle.(A) Pressure-volume cycle of left ventricle; (B) Pressure-volume cycle under different end-diastolic volume; (C) relationship between stroke work, dP/dt_{max} and EDV (reproduced with permission of Kass and Maughan (Kass and Maughan, 1988)).

There are many other techniques and methods used for analyzing the mechanical behavior of the heart. Most analyses are based on changes in ESV and EDV, which is highly related with timing of cardiac contractions. For example, if the ventricular filling time is decreased by high heart rate due to atrial fibrillation, EDV will be decreased, which consequently depresses EF, dp/dt_{max}, and stroke work. Therefore, it is critical to study the timing of cardiac contraction, which is determined by the electrical behavior of the heart.

2.2.2 Electrical Behavior of the Heart

Rhythmic pumping behavior of the heart relies on the propagation of electrical impulses within the heart. The electrical signal starts from the sinoatrial (SA) node in the right atrial wall, adjacent to the entrance of the superior vena cava. From SA node, the electrical signal is conducted along the atrial walls and spreads through both atria, which initiate contraction of atria. The annulus fibrosus electrically insulates the ventricles from the atria, thus the electrical impulse is transmitted to the ventricles solely through the atrialventricular (AV) node and "bundle of His" as shown in Figure 2.4.

The electrical activity of the heart originates from the myocytes, whose excitation is tightly coupled with its mechanical contraction. The electrical excitation of the myocytes is created by a sequence of ion fluxes through specific channels. The propagation of electrical excitation between myocytes is achieved by intercellular transport of ions via gap junctions. The change in extracellular potentials resulting from the myocardial electrical activity is called cardiac action potential, which modulate the electrical impulse propagation and initiate the excitation of myocytes. In this section, details of cardiac electrical activities are reviewed.

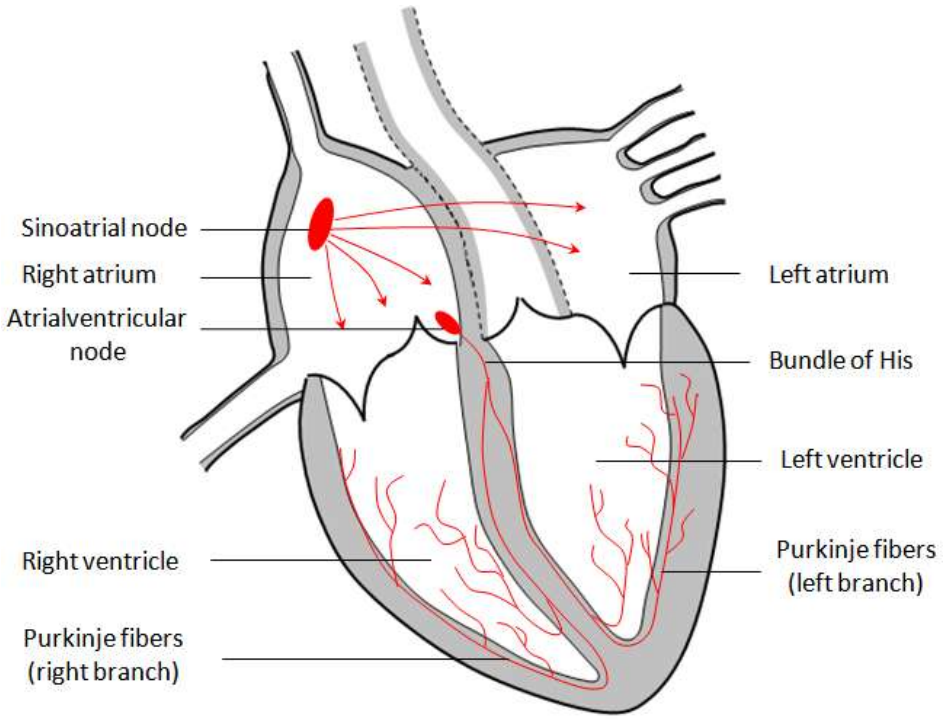

Figure 2.4: Main components of the cardiac electrical conduction system. Sinoatrial (SA) node is located to the right of the superior vena cava entrance; Atrialventricular (AV) node lies beneath the endocardium in the inferoposterior part of the interatrial septum; together with AV node, Bundle of His forms the only electrical conduction pathway from atria to ventricles.

The cardiac action potential was first recorded by Coraboeuf and Weidmann (Coraboeuf and Weidmann, 1949a, Coraboeuf and Weidmann, 1949b), it became possible to relate properties of membrane ion channels to the generation of action potential based on computational models of nerve excitation created by Hodgkin and Huxley (Hodgkin and Huxley, 1952). The classic work of Hodgkin and Huxley and other computational models for cardiac electrophysiological behavior are reviewed in section 2.4. Later low-resistance gap junctions were revealed as the primary mechanism by which the electrical impulse propagates between cardiac cells (Weidmann, 1952, Weidmann, 1966, Weidmann, 1970). Further insights into the molecular mechanism and ion channel determinants of cardiac action potential were provided by the patch clamp and related techniques (Neher and Sakmann, 1976, Reuter, 1983, Reuter and Scholz, 1968), including the Ca^{2+} inward current as a mediator of electromechanical

coupling. Based on these techniques and knowledge, various ion channels, pumps, and exchangers that contribute to generation of action potential have been discovered.

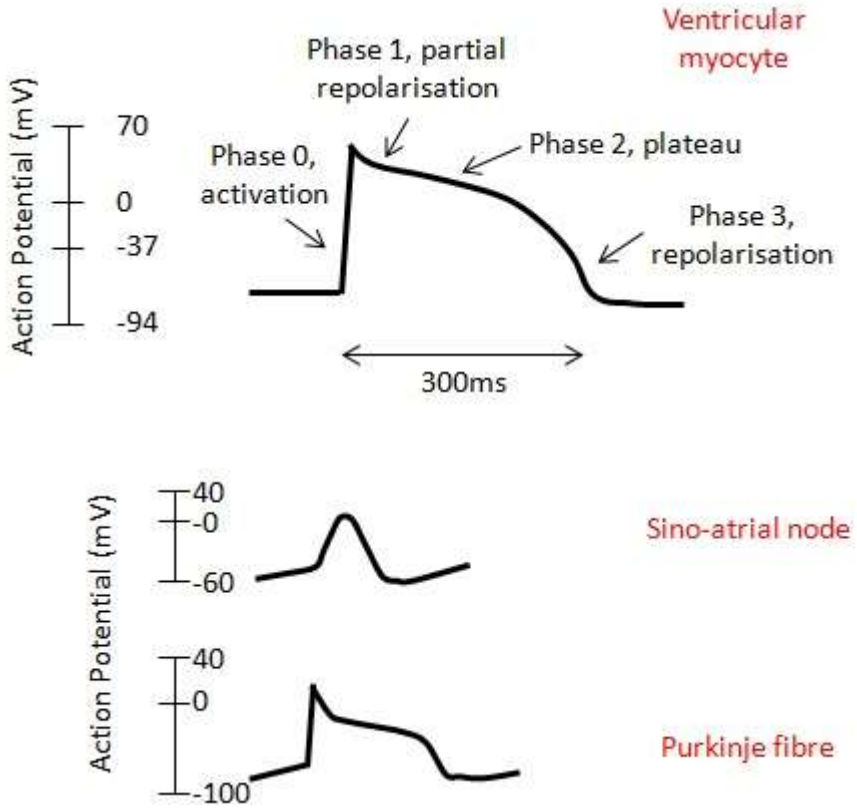

Figure 2.5: Action potential for cardiac myocytes (reproduced with permission of Levick (Levick, 2003)). (a) Action potential for ventricular endocardial myocyte; (b) action potential for non-contractile myocytes (SA node and Purkinje fiber).

As shown in Figure 2.5 (a), action potential for ventricular endocardial myocyte can be divided into four phases: in phase 0, the fast inward sodium current (I_{NA}) depolarizes the membrane at a fast rate (dV_m/dt=393 V/s), which generates the fast AP upstroke; after the potential reaches the positive voltage range, the outward flow of K^+ ions acts as a repolarisation current that decreases the membrane potential (phase 1); in phase 2, the depolarizing current provided by the inward L-type calcium current ($I_{ca(L)}$) (this depolarizing current starts in phase 0 when the

membrane voltage reaches approximately -40 mV, which allows calcium ions to flow down their concentration gradient into the cell) supports the AP plateau against the repolarizing current provided by the outward potassium currents I_{Kr} (r indicates rapid) and I_{Ks} (s indicates slow); finally (phase 3), a large increase of the outward potassium current (I_{K1}) dominates the late repolarisation phase and return the membrane to its resting state. The AP and major ionic currents that generate AP are shown in Figure 2.6.

Consequently, it is the movement of ions that generates the AP. The ion movement depends on two major factors: ion concentration and permeability of the membrane for the cell. Ion concentration provided the energetic factor that responsible for ion movement. For example, when a cell is in resting state, extracellular Na^+ concentration is around 145 mM while intracellular Na+ concentration is about 15 mM (Table 2.1). Therefore, there is a tendency for Na+ to enter the cell because of the ion concentration gradient. The cell membrane potential is about -90 mV in resting state. The membrane resting potential is maintained by the permeability of the membrane: ion channels, through which ions move between intracellular and extracellular space, remain close in resting state and consequently prevent ions from moving into or out of cell. The ion channel is either open or closed (gated) at any moment, which means an ion can only pass through when the ion channel is open. The membrane voltage determines the gating of the ion channels. In another word, the ion channels are voltage sensitive.

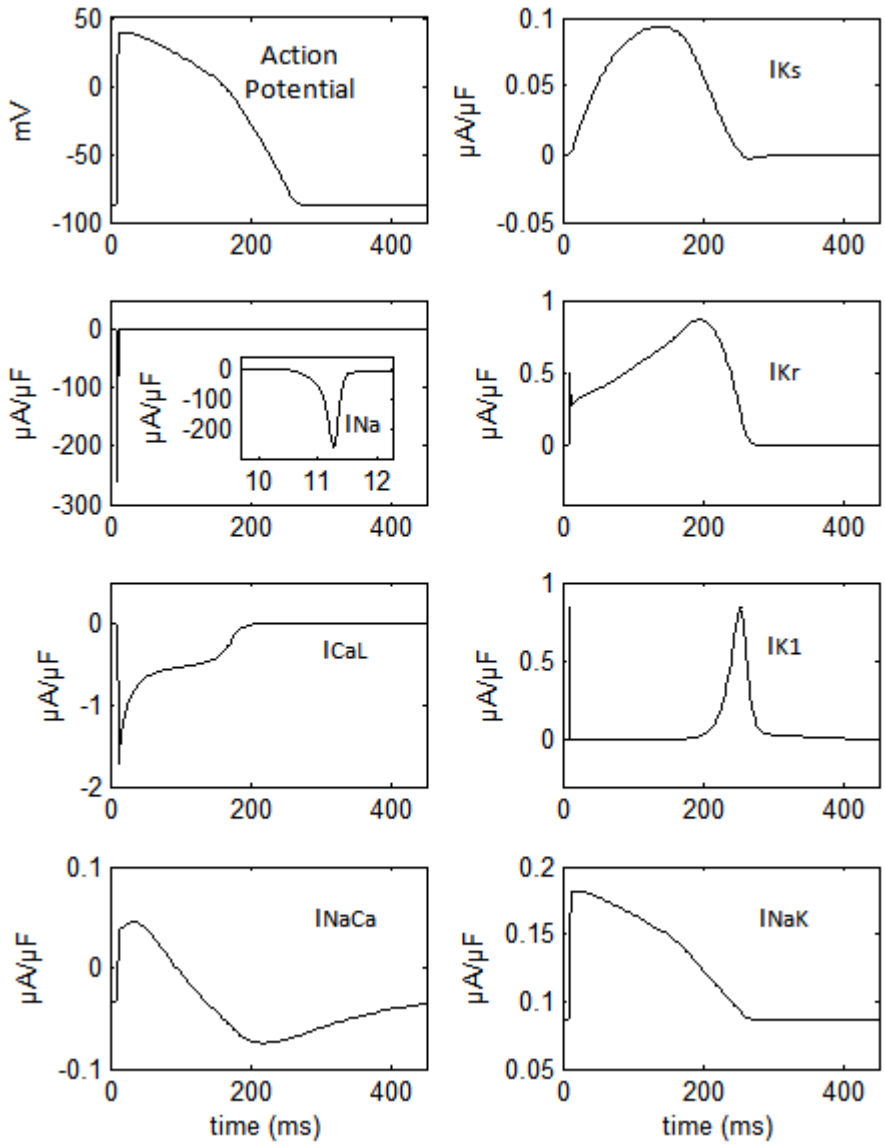

Figure 2.6: Major ionic currents during the AP. Major ionic currents during the AP. I_{Na} is shown on an expanded time scale (inset); AP and ionic currents were reproduced using the LRd model for ventricular myocyte (Luo and Rudy, 1994) with the steady-state pacing at a constant cycle length of 450 ms.

As the membrane voltage changes during AP, specific ion channels open and close, generating different inward and outward ion currents. For example, when a depolarization wave increases the membrane voltage, the resting channels change into open state, which lead to an inward

Na^+ current because of the ion concentration gradient. The opening state of the ion channels only last a few thousandths of second, and then return to close state (inactivated state). The inactivated state lasts for about 200ms, during which the channels cannot be converted back to open state and prevent any flow of sodium ions. Only when the membrane voltage has repolarized nearly back to its original resting level, can the ion channels return to the resting state and can be opened again.

Therefore, for a depolarized cell, it cannot conduct current again until the membrane has nearly fully repolarized and the channels transferred back to closed state from inactivated sate. The period within which the muscle cannot be restimulated is called refractory period (RP). RP is critical for ventricular pumping because it ensures sufficient time for ventricle to pump out blood and refill before the next contraction.

	Na^+	K^+	Ca^{2+}
Intracellular concentration (mM)	7.23	143.79	$8.54*10^{-5}$
Extracellular concentration (mM)	140	5.4	1.8

Table 2.1: Intracellular and extracellular ion concentration (O'Hara et al., 2011).

For cardiac cell, the degree of refractoriness depends on the number of Na+ channels that have recovered from inactivated state and ready to reopen. The period in which the cell is completely unexcitable to a new stimulation is called absolute refractory period. In phase 3, there is a small interval within which stimulation can produce a localized action potential that is not strong enough to propagate as shown in Figure 2.7. The period including this small

interval in phase 3 and absolute refractory period is called effective refractory period (ERP), which is also referred as action potential duration (APD).

In latter part of phase 3 (relative refractory period), the cell can be activated and generate a propagating AP. However, because the cell is stimulated from a membrane potential that is less negative than the resting potential, there are some changes in the AP: upstroke is less steep; the amplitude of the AP is smaller; conduction velocity of the AP is reduced; APD is decreased. The changes in conduction velocity and APD are referred as restitution properties of cardiac cell.

2.3 Ventricular fibrillation (VF)

Ventricular fibrillation (VF) is the leading abnormal heart rhythm for causing sudden death worldwide, claiming 70,000 deaths in the UK alone (Janse et al., 1995). Back in 1849, Ludwig and Hoffa demonstrated that VF can be initiated by the application of strong constant currents or faradic currents to the ventricles of the dog's heart (Wiggers, 1940). When VF occurs, the ventricle is thrown into a quivering state, whilst there is a great fall in the arterial blood pressure, which refers to insufficient blood pumping from the ventricle.

The first detailed visual description of VF is provided by McWilliam (McWilliam, 1887), who subsequently showed that VF in human could be terminated by applying repetitive electric shocks(McWilliam, 1887). McWilliam was not the first to use electrical shocks to rescue human life, this procedure was first reported by Charles Kite in 1788, when a 3-year-old girl, a victim of a fall, was shocked through the chest by an electric generator and a Leyden jar (Cakulev et al., 2009). However, McWilliam was the first one to suggest that VF was the mechanism for sudden death in humans.

2.3.1 Critical mass hypothesis

Based partly on McWilliam's research (McWilliam, 1889), Garrey published the first systematic study on the relationship between VF and the size of the heart (Garrey et al., 1914). Garrey's well-known hypothesis of the "critical mass" stated that the ease of fibrillation and defibrillation is inversely proportional to the mass of fibrillating tissue. Garrey indicated that any part of the mass of ventricular tissue would cease fibrillating if its surface area is smaller than 4 cm^2 (Garrey et al., 1914). Moreover, Garrey presented the reentry mechanism, similar to the one described independently by Mines (Mines, 1913), which laid the foundation for current studying the mechanisms and dynamics of VF.

In 1930, Wiggers carried out high-speed cinematographic studies on the evolution of VF initiated by faradic stimulation in the dog's heart (Wiggers et al., 2003), and summarized that uninterrupted arrhythmia goes through four stages (Wiggers et al., 2003): (a) the initial tachysystolic phenomena: VF usually start with a few peristaltic waves sweeping rapidly (less than 1 second) over the ventricular surfaces; (b) stage of convulsive incoordination: waves of contraction with rhythm and sequence distinctly different from the initial stage pass over the ventricles (15-40 seconds); (c) stage of tremulous incoordination: the entire surface of the ventricles presents the appearance of multiple rapid shivering motions; (d) stage of progressive atonic incoordination: shivering motions of the ventricular surface slow down, while the ventricular pressure is no longer maintained. Latter in 1941, Moe did electrographic studies on the mechanism of reentry, and indicated that as reentry is initiated there were a progressive decrease in refractory period and an increase in conduction time due to the repetitive impulses (Spielman et al., 1978).

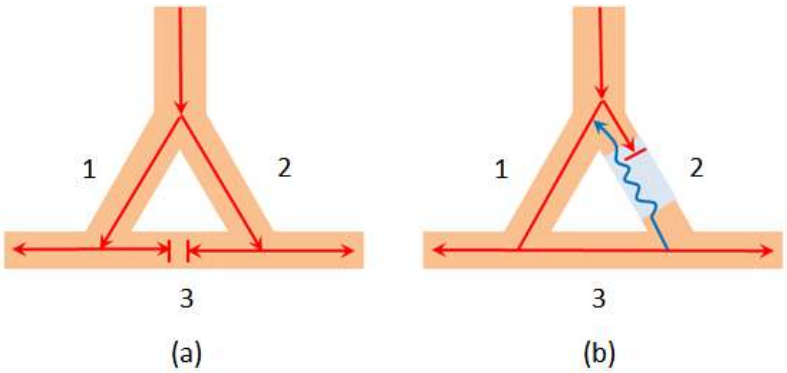

Figure 2.7: Reentry mechanism. (a): If a normal tissue (e.g. Purkinje fiber) forms two branches (1 and 2), the action potential will travel down each branch. If branch 1 and 2 are connected by a connecting pathway (branch 3), the action potentials conducted from the two branches will cancel each other out in branch 3; (b) if branch 2 has a unidirectional block (e.g. regional ischemia) as indicated by the cyan area, action potential can travel back into branch 2 from branch 3. If action potential from branch 2 continues travelling down branch 1, a circular pathway of high frequency impulse will spread through a region of the heart or the entire heart.

2.3.2 Multi-wavelet hypothesis

When the time comes to 1946, Weiner and Rosenblueth presented a theoretical description of the mechanism of fibrillation (Wiener and Rosenblueth, 1946). Their research assumed that the reentry mechanism could lead to wave rotation (spiral wave) around single or multiple obstacles, which was necessary to initiate and maintain arrhythmia. Also, they carried out simulation studies on conductions between two overlapping regions in a two-dimensional excitable sheet, and demonstrated that sustained wave rotation could not be initiated in a homogeneous two-dimensional sheet. Based on Weiner and Rosenblueth's model, Selfridge showed a spiral wave in a two-dimensional medium (Selfridge, 1948). Heterogeneity of excitable medium obviously became an important factor in the studies of fibrillation.

In 1959, Moe and Abildskov demonstrated the importance of heterogeneity of cardiac tissue in their studies of atrial fibrillation (AF) (Moe et al., 1964). In the well-known "multiple-wavelet hypothesis" constructed by Moe (Moe et al., 1964), he demonstrated that the occurrence of fibrillation results from the heterogeneity in the refractory periods, and is initiated by a series of stimuli with extremely short coupling intervals that are close to the minimum refractory period. During the process of excitation wave propagation, cells with refractory periods larger than the coupling interval result in blockage of wave propagation due to not having enough time to recover, which consequently leads to formation of multiple wavelets. Based on their simulation studies, they stated that AF could be self-sustaining and independent of its initiating agency if the tissue size and the number of wavelets are large enough, but AF could not terminate by its self without the presence of inhomogeneous repolarisation. Although Moe's works aimed to study AF, a number of researches were carried out assuming the "multi-wavelet hypothesis" also applies to the mechanism of VF (Krinsky, 1966, Downar et al., 1988, Witkowski et al., 1998).

In 1966, Krinsky showed that increased heterogeneity in refractory periods may lead to initiation of VF (Krinsky, 1966). On the other hand, large heterogeneity in refractory periods may also cause fragmentation in re-entry circuits, which may result in termination of self-sustained fibrillation. Moe's hypothesis successfully explained the mechanism of initiation and maintenance of fibrillation. However, this hypothesis was short of quantitative predictions that could be tested in experiments. Various studies have been undertaken to justify the relationship between the extent of tissue heterogeneity and the incidence of VF (Zipes and Jalife, 2009). Due to technical limitation (measurement of refractory periods cannot be made at a large number of points), these studies only revealed a positive correlation between increased heterogeneity in refractory period and fibrillation, but was not sufficient to truly prove this is a necessary condition for both initiation and maintenance of VF (Janse et al., 1995).

2.3.3 Single source hypothesis

The development of advanced optical mapping methods for visualizing the excitation patterns on the surface of the heart such as unipolar recording and non-contact mapping technique have led to studies of excitation patterns during VF (Witkowski et al., 1998, Gray et al., 1998, Rogers et al., 1999, Gray et al., 1995). Gray's study demonstrated movement of a single spiral wave over the surface of the ventricles, and showed that the excitation patterns can be different from the ones predicted by the multi-wavelet hypothesis (Gray et al., 1998). Their studies indicated that a single spiral wave can produce VF, and VF is maintained not by multiple wavelets but by some stable rapid sources of re-entrant circuit (Tabereaux et al., 2009). Moreover, based on Gray's work, during VF, most spiral waves do not form complete re-entry loops (Gray et al., 1998).

2.3.4 Spiral breakup hypothesis

With the development of computer modelling techniques, studies of excitation propagation in cellular automata models have been significantly extended by using ionic models of cardiac tissue, which is pioneered by the experimental work of the giant squid axon conducted by Hodgkin and Huxley (Hodgkin and Huxley, 1952). The ionic models provide a more accurate description of interactions between adjacent cells and transmembrane ionic currents. Simulation studies based on computational models indicted how spiral wave could breakup into complicated activation pattern that is from by many wavelets of various sizes. Different from multi-wavelet hypothesis and single-source hypothesis, simulation studies showed spiral breakup can occur in homogeneous cardiac tissue (Kuramoto and Koga, 1981, Qu et al., 1999). In homogeneous cardiac tissue, fragmentation of spiral wave normally occurs close to its centre, after which the region of chaotic patterns extends to the whole cardiac tissue.

Research showed that spiral breakup only occur if the tissue is large enough, otherwise, the spiral wave will remain stable or alternatively break up but not be able to maintain fibrillation (Karma, 1993). This conclusion is restricted in two-dimensional cardiac tissue. In the heart, excitation conduction occurs in three-dimensional tissue, which largely extends the possibility of occurrence of spiral breakup (Panfilov, 1999).

The three-dimensional simulation of spiral breakup was carried out in the anatomical model of the heart that includes detailed structure of the ventricle obtained from extensive experiments. Currently, available anatomical models commonly used include rabbit ventricular model (Vetter and McCulloch, 1998), canine ventricular model (Nielsen et al., 1991), pig ventricular model (Stevens et al., 2003), and human ventricular model (Hren et al., 1998).

Computational studies of spiral breakup presented valuable explanations in terms of its formation and maintenance. However, this is highly restricted to computational studies. Until recently, there was no experimental work supporting spiral breakup hypothesis. Moreover, computational models have certain limitations: fibre orientation of human ventricular anatomical model was fitted from canine model (Hren et al., 1998); in human ventricular ionic model (ten Tusscher et al., 2004), kinetics in the calcium/calmodulin-dependent protein kinase model adopted the ones used in dog model (Hund and Rudy, 2004) due to the absence of human ventricular specific measurements. These limitations together with the complexity of anatomical structure of individual patient determine three-dimensional computational study is not appropriate for patient-specified experimental studies.

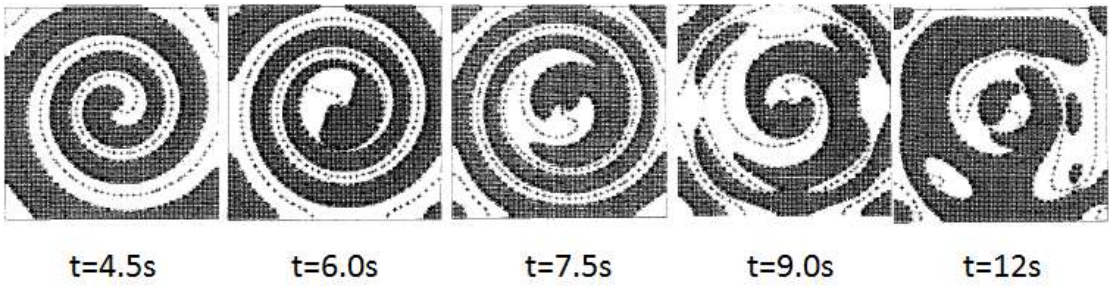

(a)

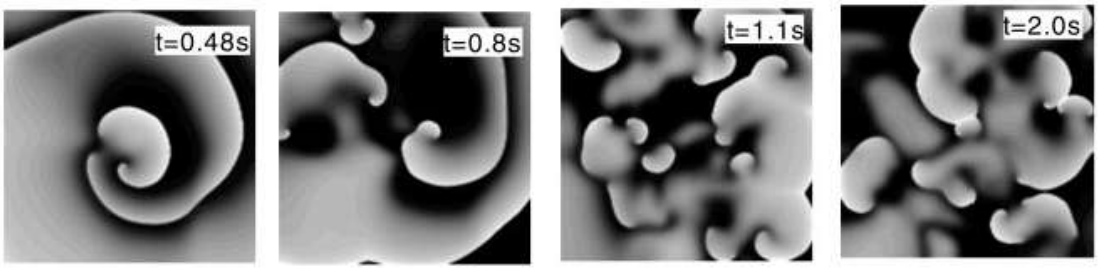

(b)

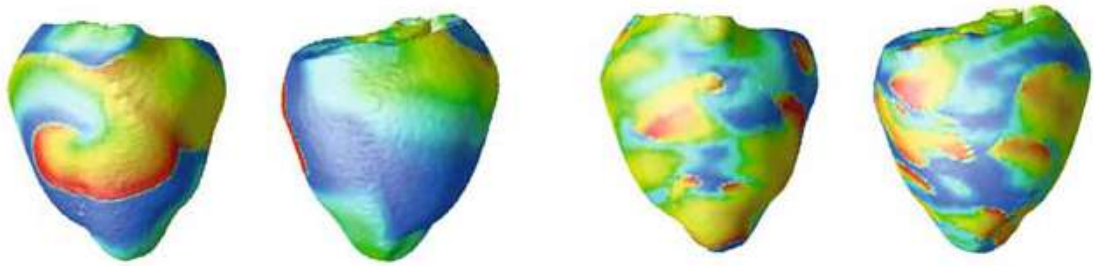

(c)

Figure 2.8: Spiral wave breakup in 2D cardiac tissue and in the anatomic heart model. (a) the first computational studies of spiral wave break was carried out by Kuramoto and Koga in 1981 based on a model called $\lambda - \omega$ system that is different from current used ionic model (reproduced with permission of Kuramoto and Koga (Kuramoto and Koga, 1981)); (b) 2D spiral wave break simulation studies based on cardiac ionic model (reproduced with permission of Qu et al. (Qu et al., 1999)); (c) 3D simulation of spiral wave and spiral wave breakup in the anatomic heart model (reproduced with permission of Sato et al. (Sato et al., 2009)).

2.3.5 Restitution hypothesis

As stated in section 2.2.2, APD decreases as short coupling interval is introduced. Research (Bass, 1975, Marculs L. Koller, 1998, Qu et al., 1999, Huang et al., 2004) showed APD is related with its preceding diastolic interval (DI), which is the time between the repolarisation time of preceding beat and activation time of current beat. This phenomenon is called APD restitution, and has been regarded as a key mechanism in analyzing the stability of re-entry (Kobayashi et al., 1992, Qu et al., 1999, Swissa et al., 2002). APD restitution hypothesis stated that APD restitution curve relating APD to DI with its slope large than one could lead to wavebreak and re-entry. Its mechanism is very simple: large slope of APD restitution curve means small change in DI (due to slow conduction velocity in premature beat) results in large variance in APD, which creates a larger change in DI for the next wave propagation, and APD alternates between long and short. This phenomenon is referred as APD alternans, and is regarded as a key mechanism for spiral breakup (Karma, 1993).

The relationship between steep APD restitution and APD alternans was presented back in 1968 by Nolasco and Dahlen (Nolasco and Dahlen, 1968). When the time comes to 1993, Karma showed that this mechanism could lead to spiral breakup based on a simplified FitzHugh-Nagumo model (Karma, 1993, Karma, 1994). Qu et al. obtained similar results using more detailed cardiac ionic models (Qu et al., 1999). Except the simulation studies, large amount of experimental works have been carried out demonstrating APD restitution hypothesis. Experimental works showed certain drugs (diacetyl monoxime and verapamil (Riccio et al., 1999), bretylium (Garfinkel et al., 2000)) can flatten the restitution curve and prevent the occurrence of VF. These findings proved that APD hypothesis can well be used for screening new anti-arrhythmic drugs. More importantly, different from previous hypothesis, this method can be easily achieved by using existing experimental techniques.

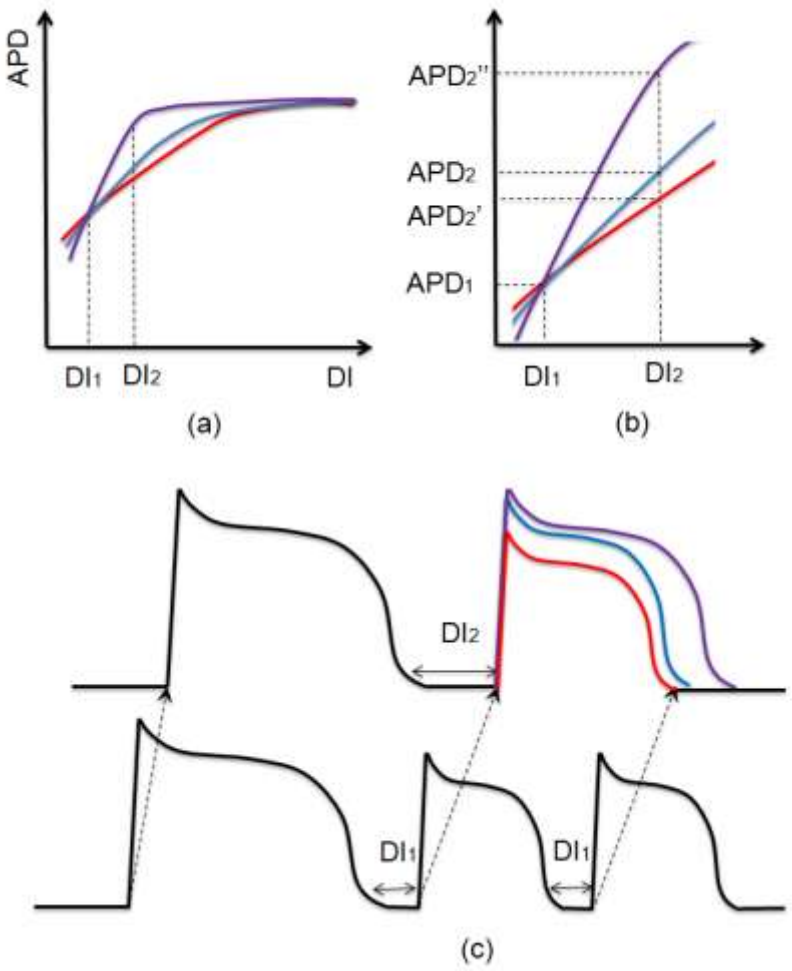

Figure 2.9: Influence of APD restitution properties on instability of activation propagation. (a) Three APD restitution curves with different slopes (red: APD restitution curve with its maximum slope smaller than 1; blue: APD restitution curve with its maximum slope equal to 1; purple: APD restitution curve with its maximum slope larger than 1); (b) Amplified figure of (a): the slope of APD restitution equalling to 1 means increase in DI equals to the increase in APD (APD_2-APD_1=DI_2-DI_1). Consequently, APD_2'-APD_1<DI_2-DI_1, and APD_2''-APD_1>DI_2-DI_1; (c) small variance in APD (red) decreases the possibility of wave-break, while large variance in APD (purple) increases the possibility of wave-break (dashed arrow indicates activation conduction).

Although it has been proved that APD restitution hypothesis can be used in analyzing spiral breakup, and plays an important role in initiation and maintenance of VF, it should be noted that APD restitution may not be sufficient to explain the mechanism of spiral breakup. Research showed that APD restitution curve with its maximum slope large than one cannot initiate breakup in some cases (Karma, 1994, Qu et al., 1999). Also, some studies showed spiral breakup can be initiated without a steep APD restitution curve (Chudin et al., 1999, Fenton et al., 2002). Moreover, APD restitution properties are not uniform across the heart: experimental studies have documented regional differences exist at different locations within the ventricular wall (Viswanathan et al., 1999, Gima and Rudy, 2002), between two ventricles (Banville and Gray, 2002), and in chronically ischemic hearts (Yuuki et al., 2004). Regional differences in APD restitution properties have been shown to be highly related with occurrence of arrhythmias in both experimental (Han and Moe, 1964, Kuo et al., 1983) and computational studies (Sampson and Henriquez, 2001, Clayton and Taggart, 2005).

While APD restitution properties are key factors in determining stability of wave-break and re-entry, restitution of conduction velocity (CV) that is another fundamental property of cardiac tissue relating local wavefront velocity to the preceding DI also affects the instability of excitation conduction of cardiac tissue (Weiss et al., 1999, Qu et al., 1999, Cao et al., 1999, Fenton et al., 2002). Studies indicated CV slows down due to reduced availability of Na^+ channels (e.g. ischemia (Kleber et al., 1986, Kodama et al., 1984), tachycardia (Veenstra et al., 1987)). CV restitution affects excitation conduction by producing spatial variations in DI (Qu et al., 1999, Cao et al., 1999, Watanabe et al., 2001), which consequently leads to variations in APD due to APD restitution properties. Also, research showed that decreasing CV at long coupling interval and the slope of CV restitution curve increase the stability of excitation conduction (Watanabe et al., 2001).

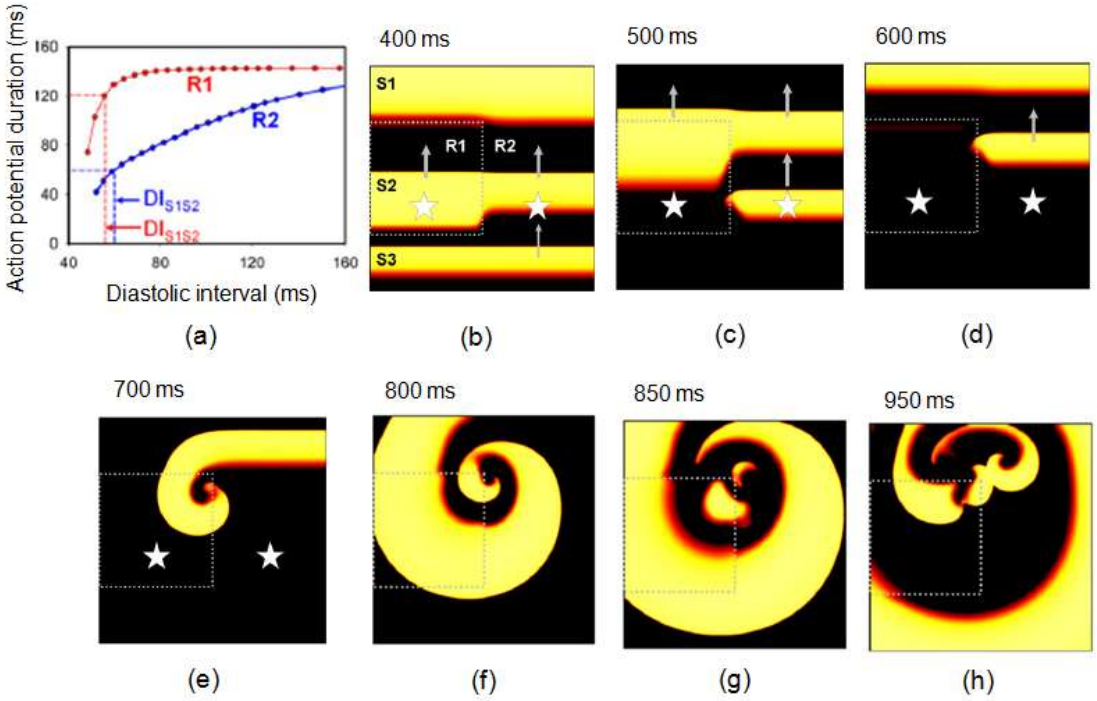

Figure 2.10: Snapshot showing formation of spiral wave and spiral breakup caused by regional difference in APD restitution properties (reproduced with permission of Clayton and Taggart (Clayton and Taggart, 2005)). Dotted line shows boundary between region R1 and R2 (as indicated in (b)), in which APD restitution properties are different (as shown in (a)); (b)-(C) are the snapshot of the process of spiral wave formation ((a)-(e)) and spiral breakup ((f)-(h)), in which black indicates resting state, while brighter colours indicate depolarized tissue; stars shown in (b)-(e) are the two locations where action potentials are recorded.

Consequently, interaction of APD restitution and CV restitution plays an important role in initiation of wave-break and re-entry (Cao et al., 1999, Jordan and Christini, 2004, Banville and Gray, 2002). However, CV restitution has not been studied as well as APD restitution. This is due to the difficulty of measuring CV without knowing the exact anatomic structure of cardiac tissue in experimental studies. Despite all this, APD restitution hypotheses including steepness of APD restitution curve and heterogeneity of restitution properties provide valuable and practical methods in explaining the mechanism of wave-break and re-entry, and in analyzing experimental data.

2.4 Computational models of cardiac electrophysiology

The first computational model describing the AP was presented by Hodgkin and Huxley, who characterized voltage-dependent conductance changes in excitable cells using the voltage-clamp technique to the squid nerve axon (Hodgkin and Huxley, 1952). Their experiments indicated that inward movement of Na^+ is responsible for depolarization of AP, while outward flow of K^+ leads to repolarisation. This process was described by a circuit diagram shown in figure 2.11 in the computational model formulated by Hodgkin and Huxley (Hodgkin and Huxley, 1952). The membrane potential (V_m) can be described by the following equation:

$$\frac{dV_m}{dt} = -\frac{1}{C_m} \cdot I_{ion} \tag{2.2}$$

Where t is the time; C_m is the membrane capacitance per unit area of membrane ($\mu F / cm^2$); I_{ion} is the total transmembrane ionic current per unit area of membrane ($\mu A / cm^2$).

Hodgkin-Huxley model assumes space-clamp conditions and does not include external stimulus. In the model, I_{ion} is the sum of inward Na^+ current (I_{Na}), outward K^+ current (I_K), and leakage current (I_L). The equilibrium potentials are described by the following equations:

$$E_{Na} = \frac{R \cdot T}{F} \cdot \ln\left(\frac{[Na^+]_o}{[Na^+]_i}\right) \tag{2.3}$$

$$E_K = \frac{R \cdot T}{F} \cdot \ln\left(\frac{[K^+]_o}{[K^+]_i}\right) \tag{2.4}$$

Where E_{Na} (mV) and E_K (mV) are the equilibrium potentials for Na^+ and K^+; R ($J/(kmol \cdot K)$) is the gas constant; T (K) is the temperature; F ($C \cdot mol^{-1}$) is Faraday's constant; $[Na^+]_o$ (mM) and

$[K^+]_o$ (Mm) are the extracellular Na^+ concentrations and K^+ concentrations; $[Na^+]_i$ (mM) and $[K^+]_i$ (Mm) are the intracellular Na^+ concentrations and K^+ concentrations.

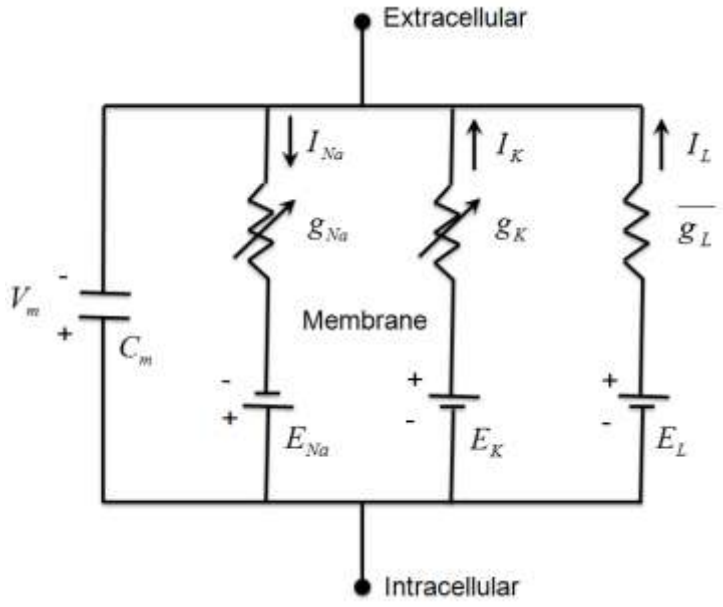

Figure 2.11: Circuit diagram of Hodgkin-Huxley model (reproduced with permission of Hodgkin and Huxley (Hodgkin and Huxley, 1952)). There are three types of currents: inward Na^+ current (I_{Na}), outward K^+ current (I_K), and leakage current (I_L). The capacitive effect of the membrane (C_m) provides charge separation. The electrical properties of the membrane are represented by two voltage-dependent conductances (sodium conductance g_{Na}, and potassium conductance g_K) and one voltage-independent conductance ($\overline{g_L}$). The differences between the transmembrane potential (V_m) and the equilibrium potentials (E_{Na}, E_K, and E_L) provide the driving force for each current.

Based on Ohm's law, the currents can be calculated as bellow:

$$I_{Na} = g_{Na} \cdot (V_m - E_{Na}) \tag{2.5}$$

$$I_K = g_K \cdot (V_m - E_K) \tag{2.6}$$

Where, g_{Na} ($\mu A/cm^2$) and g_K ($\mu A/cm^2$) are the Na^+ conductance and the K^+ conductance. The conductance for I_{Na}/I_K is defined as a function of a number of voltage dependent gates and the maximum conductance for Na^+/K^+. The state of each gate changes between open and close depending on the membrane potential. An ion can only be conducted through the gate when it is in open position. The maximum conductance is the conductance when all gates are open.

For the Na^+, the conductance can be expressed as bellow:

$$g_{Na} = g_{Na\max} \cdot m^3 \cdot h \tag{2.7}$$

Where $g_{Na\max}$ ($mS/\mu F$) is the maximum conductance; m and h are the open probabilities of the activation gate ranging from 0 (closed position) to 1 (open position). The time-dependent open probabilities can be described by the following first order differential equations:

$$\frac{dm}{dt} = \alpha_m \cdot (1-m) - \beta_m \cdot m \tag{2.8}$$

$$\frac{dh}{dt} = \alpha_h \cdot (1-h) - \beta_h \cdot h \tag{2.9}$$

Where α_m, β_m, α_h, and β_h (ms^{-1}) are potential-dependent transition rates between closed and open state. Under the boundary conditions: $m = m_0$, $h = h_0$ at $t = 0$, the solutions of differential equation 2.8 and 2.9 can be expressed as bellow:

$$m = m_\infty - (m_\infty - m_0) \cdot \exp(-t/\tau_m) \tag{2.10}$$

$$h = h_\infty - (h_\infty - h_0) \cdot \exp(-t/\tau_h) \tag{2.11}$$

Where, $m_\infty = \alpha_m/(\alpha_m + \beta_m)$, $\tau_m = 1/(\alpha_m + \beta_m)$, $h_\infty = \alpha_h/(\alpha_h + \beta_h)$, $\tau_h = 1/(\alpha_h + \beta_h)$.

Similar to Na^+, conductance of K^+ is described as bellow:

$$g_K = g_{K\max} \cdot n^4 \tag{2.12}$$

Where n is the open probability of the activation gate. The time-dependent open probability n can be described as:

$$\frac{dn}{dt} = \alpha_n \cdot (1-n) - \beta_n \cdot n \tag{2.13}$$

Where α_n and β_n (ms^{-1}) are potential-dependent transition rates between closed and open state. Under the boundary condition $n = n_0$ at $t = 0$, solving equation 2.13, open probability can be calculated as:

$$n = n_\infty - (n_\infty - n_0) \cdot \exp(-t/\tau_n) \tag{2.14}$$

Where, $n_\infty = \alpha_n / (\alpha_n + \beta_n)$, $\tau_n = 1/(\alpha_n + \beta_n)$

In Hodgkin-Huxley model, the leakage conductance is defined to be current not carried by I_{Na} or I_K, and is assumed to be constant. The leak current I_L can be expressed as:

$$I_L = g_{L\max} \cdot (V_m - E_L) \tag{2.15}$$

Where $g_{L\max}$ is the leakage conductance; E_L is the equilibrium potential for leakage current.

Although the detailed mechanism of voltage-dependent and time-dependent AP remained undiscovered at the time of Hodgkin-Huxley model, the pioneering work carried out by Hodgkin and Huxley provided a fundamental basis for future studies on computational models of AP, simulation studies of AP conduction, and the analysis of mechanism of wave-break and re-entry. However, Hodgkin-Huxley model has certain limitations: firstly, the model only includes two types of ion currents, while there are a number of other ion currents needed to

be taken into account for AP simulation (e.g. Ca^{2+} current through the L-type Ca^{2+} channel, Na^{+} current through the L-type Ca^{2+} channel, K^{+} current through the L-type Ca^{2+} channel, rapid delayed rectifier K^{+} current, slow delayed rectifier K^{+} current, inward rectifier K^{+} current, Na^{+}/Ca^{2+} exchange current et al.); secondly, Hodgkin-Huxley model assumed that the intracellular ion concentrations ($[Na]_i$, $[K]_i$) remain constant, while changes in ion concentration can be considerably important for AP simulation (e.g. changes in ion concentration affect resting potential of the cell; the conductivities of the intracellular and extracellular solutions depend on the charge-carrying ion concentrations (Nygren and Halter, 1999)).

2.4.1 First-generation cardiac action potential models

Based the Hodgkin-Huxley model, McAllister et al. presented the first cardiac AP model of the Purkinje fibre in 1975 (McAllister et al., 1975), after which Beeler and Reuter created a model for ventricular cell in 1977 (Beeler and Reuter, 1977). Similar to the Hodgkin-Huxley model, these models assumed that intracellular ion concentrations remain constant. These models can be expressed by the following equations:

$$\frac{dV_m}{dt} = -\frac{1}{C_m} \cdot \sum_S I_S \tag{2.16}$$

$$I_S = g_{S\max} x_{S1} x_{S2} \ldots x_{Sn} (V_m - E_S) \tag{2.17}$$

$$\frac{dx_{Sn}}{dt} = \frac{x_{Sn\max} - x_{Sn}}{\tau_{Sn}} \tag{2.18}$$

Where S indicates ionic species (Na^{+}, Ca^{2+}, K^{+} et al.); I_S represents the ion current; $g_{S\max}$ is the maximal conductance; x_{Sn} is the gating variable describing the open possibility of the

activation gate Sn; x_{Snmax} (voltage-dependent) is the steady-state value of gating variable x_{Sn}; τ_{Sn} is a time constant (voltage-dependent).

2.4.2 Second-generation cardiac models

As mentioned previously, Hodgkin-Huxley model and the first-generation cardiac model assumed that intracellular ion concentrations remain constant. However, in cardiac cells, there are dramatic changes in ion concentrations (e.g. ion concentration change due to entry of Ca^{2+} through the L-type calcium channel (Fabiato, 1992)). Moreover, changes in intracellular potassium concentration ($[K]_i$) and intracellular sodium concentration ($[Na]_i$) can lead to changes in morphology of AP if the cardiac cell is paced at fast rate (Rudy and Silva, 2006). In 1985, DiFrancesco and Nobel presented the first model of the Purkinje fibre (DiFrancesco-Nobel model) incorporating dynamic changes in intracellular ion concentrations (DiFrancesco and Noble, 1985). Latter on a number of models were created for various types of cardiac cells and species: e.g. atrial cell model for bullfrog (Rasmusson et al., 1990), Luo-Rudy dynamic model for guinea pig ventricular myocyte (Luo and Rudy, 1994), human ventricular model (ten Tusscher et al., 2004, O'Hara et al., 2011).

Compared with the first-generation models, these second-generation cardiac models provided detailed descriptions of changes in ion concentrations. At the same time, these second-generation cardiac models included more ion channels and exchanger currents that were discovered in experimental studies. The general form of the second-generation cardiac model is the same with the first generation cardiac model (equation 2.16-2.18), while there's an additional equation describing the changes in ion concentrations shown as below:

$$\frac{d[S]}{dt} = \sum_k I_{Sk}(V_m, S) \tag{2.19}$$

Where k is the number of ion channels, pumps, and exchanger currents carrying ion specie S; $I_{Sk}(V_m, S)$ that is a function of V_m and ion concentration represents ion channel, pump, or exchanger current carrying ion specie S.

In the human ventricular model created by ten Tusscher et al. there are 16 types of currents, and 30 ionic gates included (ten Tusscher et al., 2004). Consequently, the complexity of the model determines the second generation cardiac models are far more computational intensive. As a result, certain reduced models were developed, which only capture the important features such as excitability and refractory without including too much description of biophysical details (Clayton and Holden, 2002, Cherry and Fenton, 2004, Clayton and Taggart, 2005). The simplified model only includes three ion currents: a fast inward sodium current, a slow inward calcium current, and a slow outward potassium current. The gating variables are simplified as three variables determining the activation and inactivation state of the current.

2.4.3 Action potential conduction model

As mentioned in section 2.2, cardiac cells are connected by gap junctions, through which action potential propagates due to local current flowing ahead of the action potential upstroke. Most computational models of action potential conduction are based on two assumptions: one is to assume that cardiac tissue can be represented as several excitable elements connected by intracellular and extracellular resistances (Gima and Rudy, 2002, Conrath et al., 2004); the other one is to assume membrane voltage propagates through the tissue smoothly (ten Tusscher et al., 2004).

Under the second assumption, the simplest model for AP propagation between adjacent cells in a linear chain can be express as bellow:

$$\frac{\partial V_m}{\partial t} = -\frac{I_{ion} + I_{stim}}{C_m} + \frac{1}{\rho_x \cdot S_x \cdot C_m} \cdot \frac{\partial^2 V_m}{\partial x^2} \tag{2.20}$$

Where I_{ion} is the sum of all transmembrane currents; I_{stim} is the stimulus applied externally; ρ_x is the cellular resistivity; S_x is the surface-to-volume ratio. Notably, in this model V_m is a function of both time (t) and space (x). For the situation of single cell, Vm is constant in space ($\frac{\partial^2 V_m}{\partial x^2} = 0$), under which equation 2.20 reduces to equation 2.16. Equation 2.20 describes the AP propagation along a one-dimensional cardiac tissue. For two-dimensional and three-dimensional conduction, the model can be described as the following equation:

$$\frac{\partial V_m}{\partial t} = -\frac{I_{ion} + I_{stim}}{C_m} + \nabla \cdot (D \nabla V_m) \tag{2.21}$$

Where ∇ is the gradient operator; D is a coefficient that describes the effective diffusion of voltage through the medium (detailed form is the same with the one in equation 2.20). This model is called monodomain model, and the one-dimensional monodomain model is usually referred as cable theory.

As mentioned in section 2.3.5, CV restitution together with APD restitution plays an important role in initiation of wave-break and re-entry. Although it is difficult to measure conduction velocity in experimental studies due to lack of detailed information of anatomical structure of the heart from individual patient or animal. Computational studies provided an effective way for studying conduction velocity and its restitution properties. For one-dimensional conduction

model, equation 2.20 can change into the following form under the assumption of constant conduction velocity ($\frac{d^2x}{dt^2} = 0$):

$$\frac{\partial V_m}{\partial t} = -\frac{I_{ion} + I_{stim}}{C_m} + \frac{1}{\rho_x \cdot S_x \cdot C_m} \cdot \frac{\frac{\partial^2 V_m}{\partial t^2}}{CV^2} \tag{2.22}$$

Here, CV is conduction velocity ($CV = \frac{dx}{dt}$).

Notably, conduction velocity is not constant in the situation of premature beat with very short coupling intervals, in which case equation 2.22 becomes the following form:

$$\frac{\partial V_m}{\partial t} = -\frac{I_{ion} + I_{stim}}{C_m} + \frac{1}{\rho_x \cdot S_x \cdot C_m} \cdot \frac{\frac{\partial^2 V_m}{\partial t^2} - \frac{\partial V_m}{\partial t} \cdot \frac{d^2x}{dt^2}}{CV^2} \tag{2.23}$$

Under the assumption of constant conduction velocity, computational studies indicated that conduction velocity is proportional to the square root of the maximal upstroke of AP ($dV_m / dt_{\max}$), and reversely proportional to the square root of cellular resistivity (ρ_x) (Hodgkin, 1954, Tasaki and Hagiwara, 1957, Walton and Fozzard, 1983).

2.4.4 Ionic model for human ventricular tissue

In 2011, O'Hara et al. presented a model for undiseased human ventricular tissue (ORd model), in which most major currents (fast Na^+ current (I_{Na}), L-type Ca^{2+} current (I_{CaL}), transient outward current (I_{to}), rapid delayed rectifier current (I_{Kr}), slow delayed rectifier current (I_{Ks}), and inward rectifier K^+ current (I_{K1})) are based on human experimental data (O'Hara et

al., 2011). The general form of this model is similar to equation 2.2 and 2.16, which can be expressed as follow:

$$\frac{dV}{dt} = -\frac{I_{ion} + I_{stim}}{C_m} \tag{2.24}$$

The sum of all transmembrane ionic currents (I_{ion}) is given by the following equation:

$$I_{ion} = I_{Na} + I_{K1} + I_{to} + I_{Kr} + I_{Ks} + I_{CaL} + I_{NaCa} + I_{NaK} + I_{CaK} + I_{pCa} + I_{pK} + I_{bCa} + I_{bNa} \tag{2.25}$$

Reversal potentials:

$$E_{Na} = \frac{RT}{F}\ln\left(\frac{[Na^+]_o}{[Na^+]_i}\right) \tag{2.26}$$

$$E_K = \frac{RT}{F}\ln\left(\frac{[K^+]_o}{[K^+]_i}\right) \tag{2.27}$$

$$E_{Ks} = \frac{RT}{F}\ln\left(\frac{[K^+]_o + PR_{Na,K}\cdot[Na^+]_o}{[K^+]_i + PR_{Na,K}\cdot[Na^+]_i}\right) \tag{2.28}$$

Where $[Na^+]_o$ and $[K^+]_o$ are the extracellular ion channel concentrations, $[Na^+]_i$ and $[K^+]_i$ are the intracellular ion channel concentrations, $PR_{Na,K}$ is a constant ($PR_{Na,K} = 0.001833$).

Detailed descriptions of the ion currents included in the ORd model and initial conditions were presented in the appendix (appendix 11). The ORd model was used in this project to deduce APD restitution model (section 4.1) and CV restitution model (section 4.2), and carry out simulation studies for the purpose of studying influence of cellular ionic properties on APD

restitution (section 4.5), validating restitution models on extra-stimuli (section 5.4), and fitting ion channel model with patient-specific experimental data (section 6.5).

2.5 Conclusion

The literature review has shown that a great number of experimental studies and computational studies have been concentrated on furthering understanding of the mechanism of VF. Previous studies indicated that the electrical restitution properties of cardiac tissue and their interactions during AP propagation are good predictors of spiral wave stability in homogeneous and electrically continuous models of cardiac tissue. However, properties of cardiac tissue are not homogeneous in reality (e.g. structural discontinuities, heterogeneities of membrane properties and gap junction distribution).

As presented by restitution hypothesis, heterogeneity of restitution properties is an important determinant of initiation of wave-break and re-entry. Nevertheless there is no standard linking the extent of heterogeneity with initiation of VF. Computational ionic model of cardiac tissue provided an effective way to simulate AP and its conduction, but current models are mostly restricted in theoretical studies and applications of these models in clinical studies are still facing the problem of computationally expensive.

The new aspect of this study is that it provided a simple and effective method to integrate experimental data acquired from human electrophysiological studies into patient-specific models. Validation of this approach was done by testing whether electrophysiological responses to sequential premature stimuli can be predicted in a quantitatively accurate manner. Using a combination of physiological measurement and simulation studies, this work demonstrated that the complex interactions between activation and repolarisation induced by

sequential extra-stimuli can be approximated in terms of APD and CV restitution. This serves as a strong validation of a personalized computational approach incorporating biologically acquired variables. Moreover, condition for functional block that act as a key mechanism in initiation of VF and other cardiac arrhythmia were quantified. This study provided a platform by which individual patient data can be incorporated into computerized simulations and bridged the gap between fundamental cardiac simulation and clinical studies.

The work was accomplished using three approaches. The first approach was construction of restitution model based on experimental data. APD restitution properties were directly obtained from experimental data, while CV restitution properties were obtained by fitting a one-dimensional conduction model with the experimental data. Condition for functional block was deduced based on one-dimensional conduction model. Ventricular ionic model (O'Hara et al., 2011) was fitted with experimental data aiming to show heterogeneity of cellular ionic properties.

The second approach was verification of restitution models, which included two methods. One was to use computational ionic model to test the accuracy of restitution model under the situation of multi premature beats; the other one was to compare the simulation result with experimental data of the second premature beat. The third approach was to carry out simulation studies based on models obtained from experimental data.

3 Experimental datasets

All the clinical experiments referred in this project were done by consultant cardiologist at UCL Heart Hospital and St Thomas Hospital. Two types of recording catheter were used in the experiments: the noncontact mapping system (Ensite 3000, Endocardial Solutions Inc.) and contact mapping system (St Jude Pathfinder). The experimental data include two parts: one is electrogram for investigated sites around the inner surface of the ventricle; the other one is the geometry data of these sites. The electrogram data was digitalized and stored at 1200Hz for noncontact mapping recordings and 1000Hz for contact mapping recordings. Certain publications have been made based on these experimental data focusing on studies of ventricular arrhythmia (Gomes et al., 2012, Hanson et al., 2009). Research for this project included analysis of the experimental data obtained from these clinical studies, modelling of electrical restitution properties based on experimental data, and simulation studies using the modelled restitution properties.

3.1 Stimulation protocol

A standard S_1-S_2 restitution stimulation protocol was used in all experiments. Following three minutes of steady-state pacing at a coupling interval of 600ms, a drivetrain of ten beats was followed by an extrastimulus (S_2). The coupling interval of S_1-S_2 was decreased by 20ms to 300ms, after which it was decreased by 5ms until effective refractory period (ERP) was reached. In experiments undergoing a second extrastimulus (S_3), the coupling interval of S1-S2 was set at 10ms above the observed refractory period, and coupling interval of S_2-S_3 was decreased from 600ms to a minimum of 180ms. Experimental data obtained from S_1-S_2 stimulation was used to model restitution properties, while data from S_2-S_3 stimulation was used to test the accuracy of restitution model on predicting activation and repolarisation time in the second extrastimulus.

3.2 Waveform analysis

The aim of waveform analysis is to identify the activation and repolarisation time from the electrograms obtained from the experiments. Two methods are available for measuring activation time and repolarisation time: the traditional Wyatt method and an "alternative method" (Yue et al., 2004, Haws and Lux, 1990, Hanson et al., 2009). For electrogram analysis, the refractory period is normally named activation repolarisation interval (ARI), while in cellular ion channel model it is called APD. To avoid confusion, in the following chapters, APD is used to represent the refractory period of cardiac tissue.

Generally, the unipolar electrogram (UEG) is calculated as the difference between membrane potential (V_m) of investigated site and a location-independent potential (V_R). As shown in figure 3.1, the variance between V_m (black line in the first row) and V_R (dashed line in the first row) is very close to UEG shown in the third row of figure 3.1. In Potse's research (Potse et al., 2009), membrane potentials from 3 different locations were taken and compared with the location-independent V_R to produce different types of T wave (in figure 3.1, A: positive T wave; B: biphasic T wave; C: negative T wave). Based on Potse's work, the instance when the T wave reaches its maximum slope is the best estimate of repolarisation time (Wyatt method) regardless of type of T wave. Consequently, waveform analysis method can be summarized as:

Activation time: the instance of QRS wave reaching its minimum slope.

Repolarisation time: the instance of T wave reaching its maximum slope.

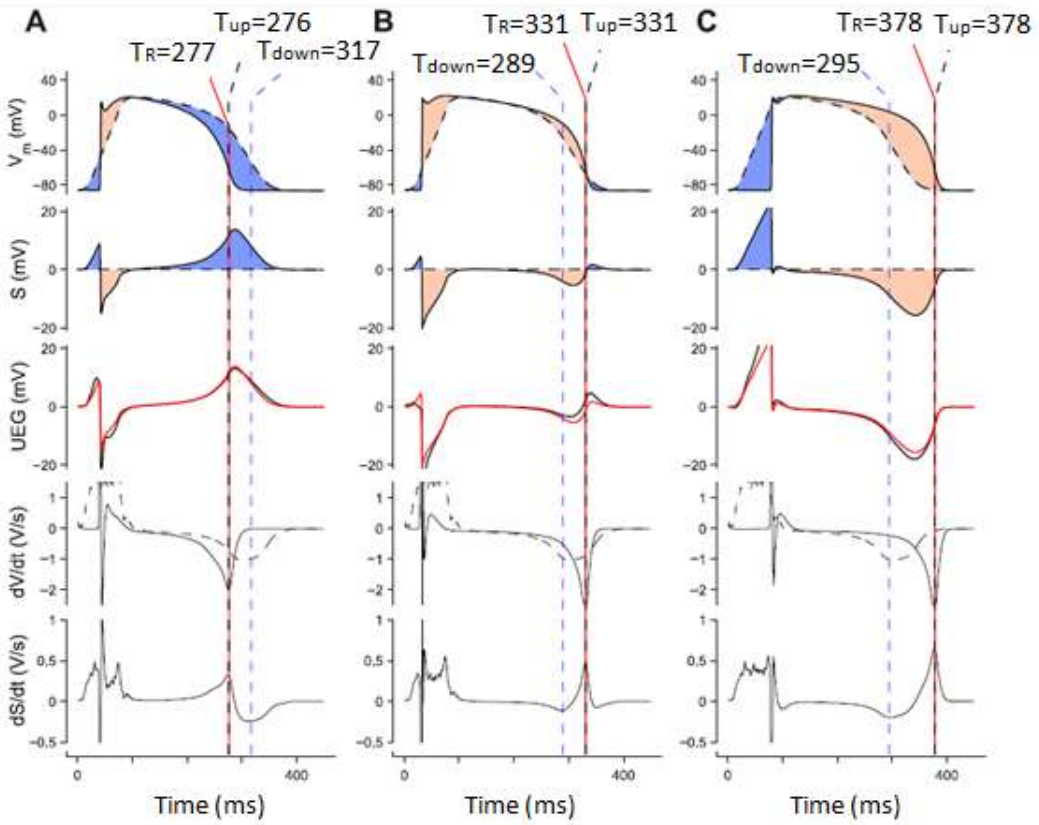

Figure 3.1: Different types of unipolar electrogram (reproduced with permission from Potse et al. (Potse et al., 2009). In the first row, the black lines indicate membrane potential V_m, while the dashed lines represent the location-independent V_R; in the second row, S is the variance calculated between V_m and V_R; in the third row UEG simulated from the simplified model (red lines) is compared with UEG obtained from realistic model (black lines); in the fifth row, solid lines indicate the temporal derivative of V_m, while the dashed lines indicate the temporal derivative of V_R; the fifth row shows the temporal derivative of UEG (dS/dt). (T_{up}: instance of maximum dS/dt in T wave; T_{down}: instance of minimum dS/dt in T wave; T_R: the instance of minimum dV/dt)

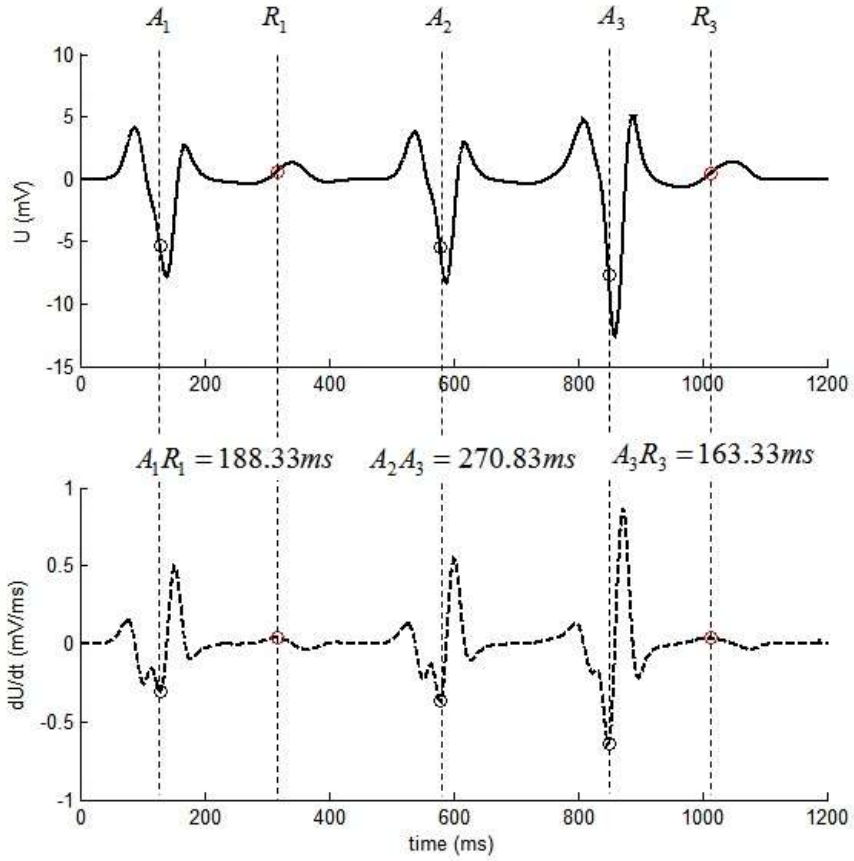

Figure 3.2: Waveform analysis. U indicates the electrogram, while dU/dt represent its temporal derivative; A_1 and A_2 are the activation times of two steady-state beats (S_1), while A_3 is the activation time of premature beat (S_2); R1 is the repolarisation time of steady-state beat (S_{1A1}), while R_3 is the repolarisation time of premature beat (S_2).

For each electrogram, five steady-state beats (S_1) and one premature beat (S_2) were analysed, in which activation time and repolarisation time were identified using the method mentioned above (as shown in figure 3.2). Based on the identified activation times and repolarisation times, certain restitution properties can be calculated as bellow (A_1 and A_2 are both steady-state beat with same coupling interval, hence their APDs are same):

Steady-state APD: $APD_{SS} = A_1R_1$

Diastolic interval: $DI = A_2A_3 - A_1R_1$

APD of premature beat: $APD = A_3 R_3$

Consequently, variables obtained from experimental data (UEG) include: coupling interval (CI), activation time (AT), repolarisation time (RT), diastolic interval (DI), refractory period (APD) for steady-state beat (S_1) and premature beat (S_2)

4 Numerical formulation

4.1 APD Restitution model for human ventricular tissue

In order to build up restitution model, simulation based on human ventricular ionic model (Appendix 11 (O'Hara et al., 2011)) was carried out, and APD restitution properties were obtained based on simulation result as shown in figure 3.1 (APD is defined as action potential duration at 90% repolarisation (APD_{90}) (Qu et al., 1999, Kim et al., 2002, ten Tusscher et al., 2004)). Theoretically, the initial conditions at the instance of pacing determine APD and CV. These initial conditions include the membrane potential, ion concentrations, ionic gate variables. It is very difficult to deduce the relationship between DI and APD based on the whole ionic model because of the complexity of the model (changes in APD and CV are the result of combined effect of all kinds of initial conditions). However, some simplified approximate relationships could be indentified between initial conditions and restitution properties. Comparisons were made between the value of 41 variables (as listed in table A.11.1) at the instance of premature beat initiation and APD afterward. Some examples were presented in figure 3.2. The comparisons indicated the slow development of Ca^{2+} dependent inactivation gate variable ($f_{Ca,slow}$) for I_{CaL} showed an approximately linear relationship with APD (coefficient of determination R^2=0.9982, root mean squared error=0.3618). Consequently, a linear relationship can be assume between $f_{Ca,slow}$ and APD. Referring to the steady-state values of the two variables (APD_{ss} , $f_{Ca,slow,ss}$), the following relationship can be obtained:

$$\frac{APD_{ss} - APD}{f_{Ca,slow,ss} - f_{Ca,slow}} = C \tag{4.1}$$

Here, C is a constant that equals to the slope of $f_{Ca,slow}$-APD relationship.

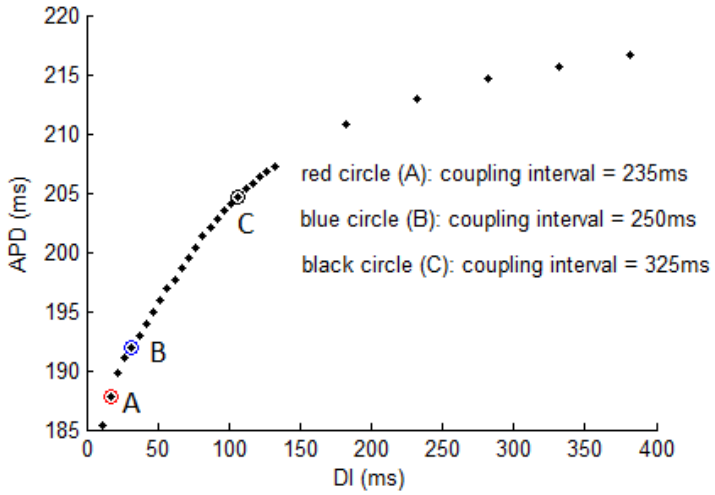

(a)

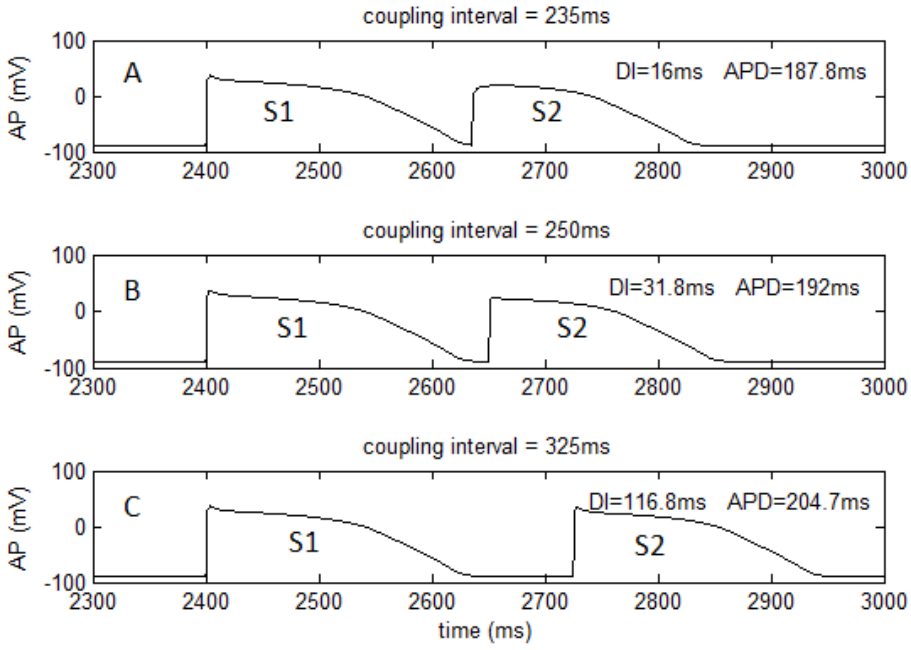

(b)

Figure 4.1: APD restitution and action potential under different coupling intervals (simulation based on human ventricular ionic model (ten Tusscher et al., 2004)). (a) APD restitution (three example data were picked up to show the difference of AP under different coupling intervals); (b) changes in AP under different coupling intervals (S1 indicates steady-state beat (coupling interval = 600ms), while S2 indicates premature beat).

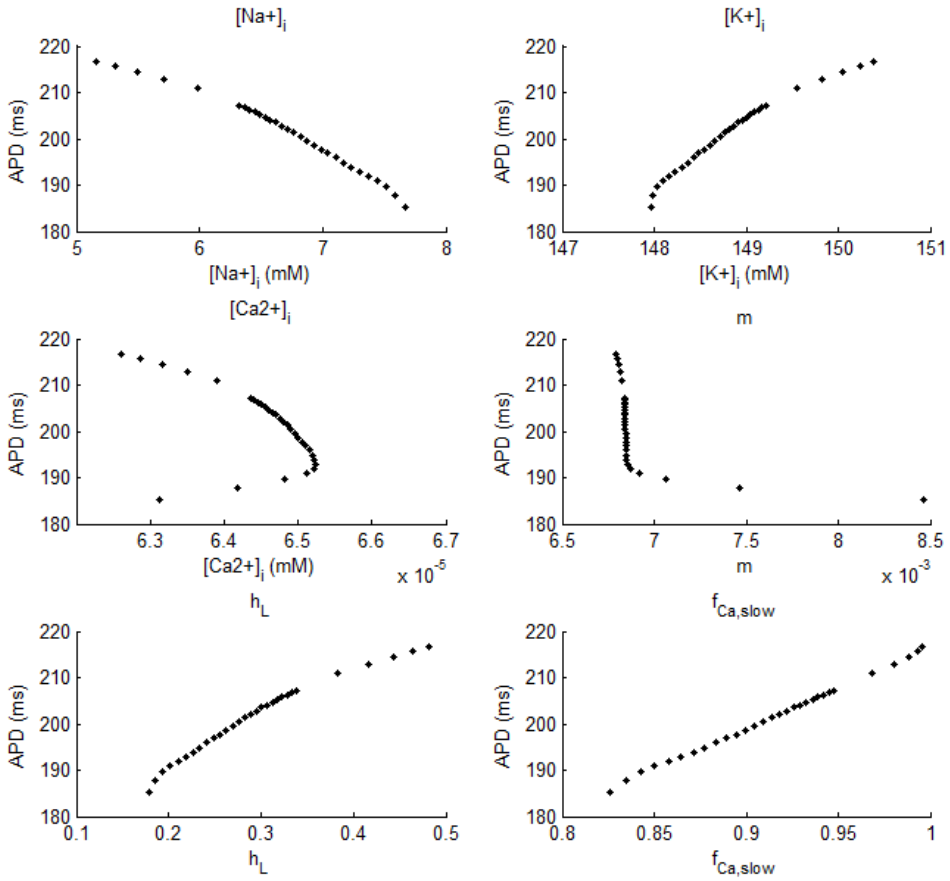

Figure 4.2: Relationships between initial conditions for some variables at the instance of premature beat initiation and APD. $[Na^+]_i$: intracellular sodium ion concentration; $[K^+]_i$: intracellular potassium ion concentration; $[Ca^{2+}]_i$: intracellular calcium ion concentration; m: activation gate for fast Na+ current ($I_{Na,fast}$); h_L: inactivation gate for late Na+ current ($I_{Na,late}$); $f_{Ca,slow}$: slow development of Ca^{2+} dependent inactivation gate for Ca^{2+} current through the L-type Ca^{2+} channel (I_{CaL}).

As showed by equation A.11.76-A.11.87, $f_{Ca,slow}$ is a function of V. Hence, APD can also be expressed as a function of V. Early research used exponential equations to describe the upstroke of action potential (Walton and Fozzard, 1983). Similarly, if the instance of repolarisation from steady-state beat S1 is defined to time 0, then V can also be expressed by

an exponential equation, in which case DI equals to the time when pacing signal of premature beat is introduced (as shown in figure 4.3). Consequently V at the instance of pacing can be expressed as bellow:

$$V = C_1 \cdot \exp(C_2 \cdot DI) + C_3 \tag{4.2}$$

Here, C_1, C_2, and C_3 are three constants. According to equation A.11.76-A.11.87, the relationship between $f_{Ca,slow}$ and V can be expressed as:

$$f_{Ca,slow,\infty} = \frac{1}{1+\exp\left(\frac{V+C_4}{C_5}\right)} \tag{4.3}$$

$$\tau_{fCa,slow} = C_6 + \frac{1}{C_7 \cdot \exp(C_8 \cdot V) + C_7 \cdot \exp(C_9 \cdot V)} \tag{4.4}$$

$$\frac{df_{Ca,slow}}{dt} = \frac{f_{Ca,slow,\infty} - f_{Ca,slow}}{\tau_{fCa,slow}} \tag{4.5}$$

Here, C_4-C_9 are constants. The solution of ordinary differential equation 4.5 can be expressed as bellow:

$$f_{Ca,slow}(DI) = e^{-\int P(DI)dDI} \cdot \left(\int Q(DI) \cdot e^{\int P(DI)dDI} dDI + C_{11} \right) \tag{4.6}$$

Here,

$$P(DI) = \frac{1}{C_6 + \frac{1}{C_7 \cdot \exp(C_8 \cdot (C_1 \cdot \exp(C_2 \cdot DI) + C_3)) + C_7 \cdot \exp(C_9 \cdot (C_1 \cdot \exp(C_2 \cdot DI) + C_3))}} \tag{4.7}$$

$$Q(DI) = \frac{\dfrac{1}{1+\exp\left(\dfrac{(C_1 \cdot \exp(C_2 \cdot DI) + C_3) + C_4}{C_5}\right)}}{C_6 + \dfrac{1}{C_7 \cdot \exp(C_8 \cdot (C_1 \cdot \exp(C_2 \cdot DI) + C_3)) + C_7 \cdot \exp(C_9 \cdot (C_1 \cdot \exp(C_2 \cdot DI) + C_3))}} \quad (4.8)$$

The solution equation 4.6 is too complicated to solve. In order to obtain the APD restitution model, simplifications were made on equation 4.7 and 4.8 in terms of approximate replacements.

Calculation based on human ventricular ionic model demonstrates changes in P(DI) and Q(DI) are very small ($1.0233 \cdot 10^{-5}$ for P(DI), and $1.0234 \cdot 10^{-5}$ for Q(DI) when DI change from 1ms to 200ms) compared with their averaged value ($P(DI)_{mean} = Q(DI)_{mean} = 0.01$). Here, P(DI) and Q(DI) are regarded as constants. Consequently, equation 3.6 can be expressed as:

$$f_{Ca,slow}(DI) = 1 + C_{10} \cdot \exp(C_{11} \cdot DI) \quad (4.7)$$

Combining equations 4.1 and 4.7, the relationship between DI and APD can be expressed as bellow:

$$APD = APDss - C \cdot (f_{Ca,slow,ss} - 1 - C_{10} \cdot \exp(C_{11} \cdot DI)) \quad (4.8)$$

For specific ventricular tissue, APD_{ss} and $f_{Ca,slow,ss}$ are constants ($f_{Ca,slow,ss} = 1$ as shown in figure 4.2). Therefore, the general form of APD restitution model can be expressed as:

$$APD = APD_{SS} - B_{APD} \cdot e^{C_{APD} \cdot DI} \quad (4.9)$$

Here, B_{APD} and C_{APD} are constants. Notably, C_{APD} and C_{11} should equal to the negative of the averaged value of P and Q (-0.01 for the ionic model used here). As shown in figure 4.4, in the fitted exponential model, B_3=-0.0088, which is very close the expected value.

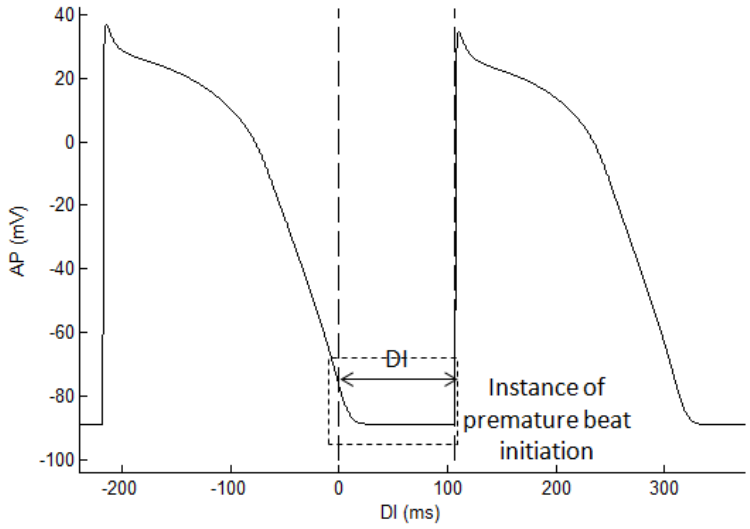

(a)

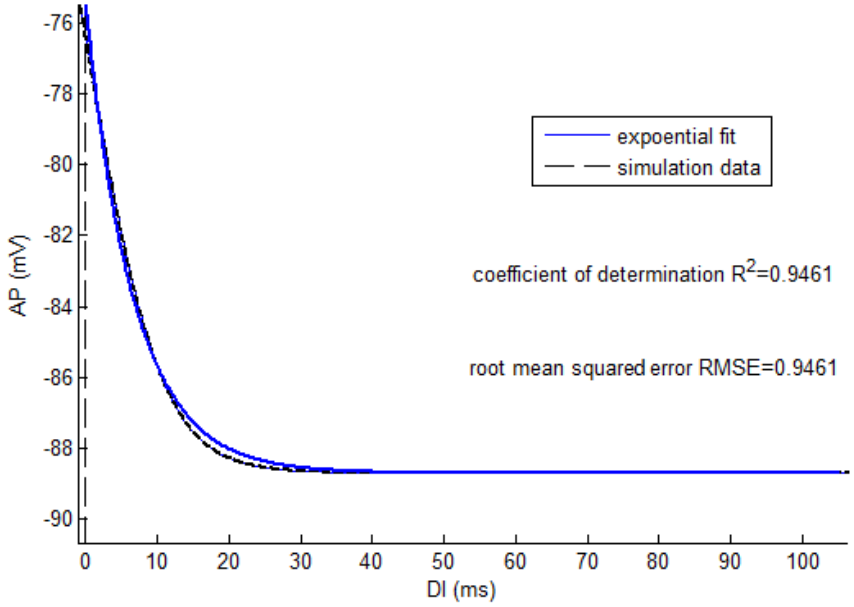

(b)

Figure 4.3: Express V at the instance of premature beat initiation using DI. (a) diagram of AP; (b) exponential fit of V between the instance of repolarisation of steady-state beat and initiation of premature beat (as indicated by the boxed area of (a)).

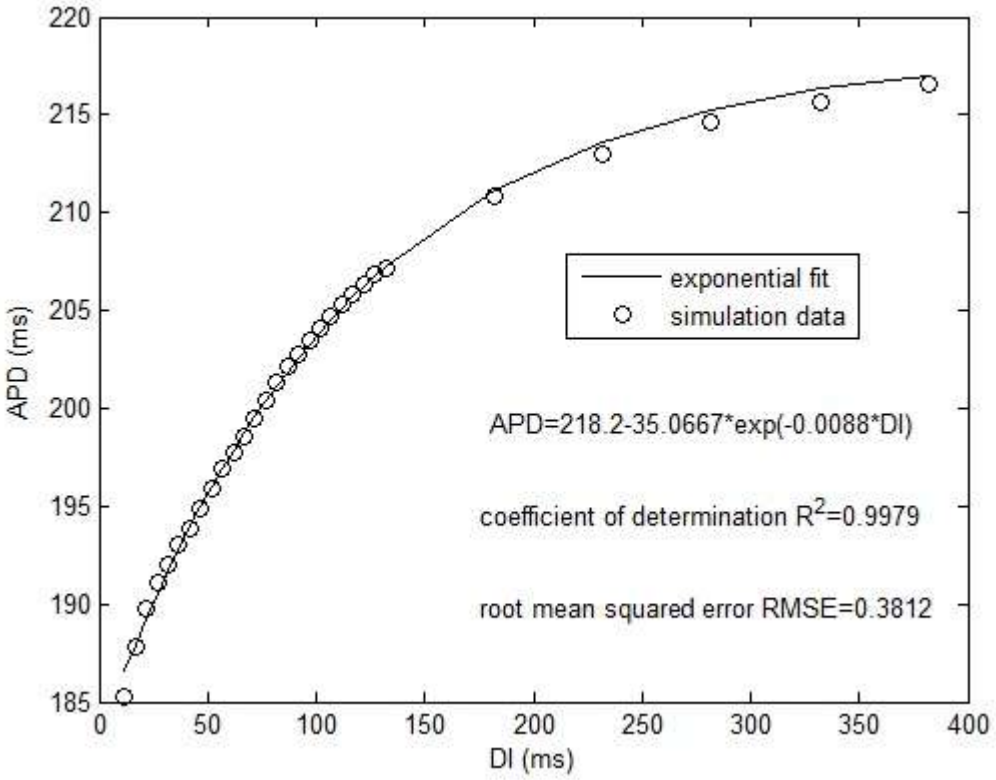

Figure 4.4: APD restitution obtained from human ventricular ionic model and the exponential APD restitution model fitted. Restitution data was obtained using S1-S2 pacing protocol, with steady-state coupling interval equalling to 600ms.

4.2 CV restitution model for human ventricular tissue

As mentioned in section 2.4.3, conduction velocity is proportional to the square root of the maximal upstroke of AP ($dV_m / dt_{\max}$), and reversely proportional to the square root of cellular resistivity (ρ_x). As shown by equation 2.22, conduction velocity can be calculated under fixed time step (Δt) and space step (Δx). However, it is hard to obtain the exact relationship between conduction velocity and DI due to the complexity of ionic conduction model (Hodgkin, 1954).

Research demonstrated that the conduction velocity can be approximately expressed by the following equation(Walton and Fozzard, 1983):

$$CV = \sqrt{\frac{2r_{cell}}{R_i \cdot C_m}} \cdot \sqrt{\frac{V'_{\max}}{V_{peak}}} \tag{4.10}$$

Where, $r_{cell} = 0.0011cm$ is the cellular radius; $R_i = 181\Omega \cdot cm$ is the cellular resistivity; $C_m = 2\mu F / cm^2$ is the cell capacitance per unit surface area (ten Tusscher et al., 2004); $V'_{\max}$ is the maximum upstroke velocity of AP; V_{peak} is the peak membrane potential at the end of AP upstroke.

Referring to previous research (Banville and Gray, 2002), CV restitution was presented by an exponential model in the following form:

$$CV = CV_{SS} - B_{CV} \cdot \exp(C_{CV} \cdot DI) \tag{4.11}$$

Where, CV_{SS} is the steady-state conduction velocity defined to be 0.72 according to literature (Taggart et al., 2000); B_{CV} and C_{CV} are two constants determining the steepness of CV restitution curve.

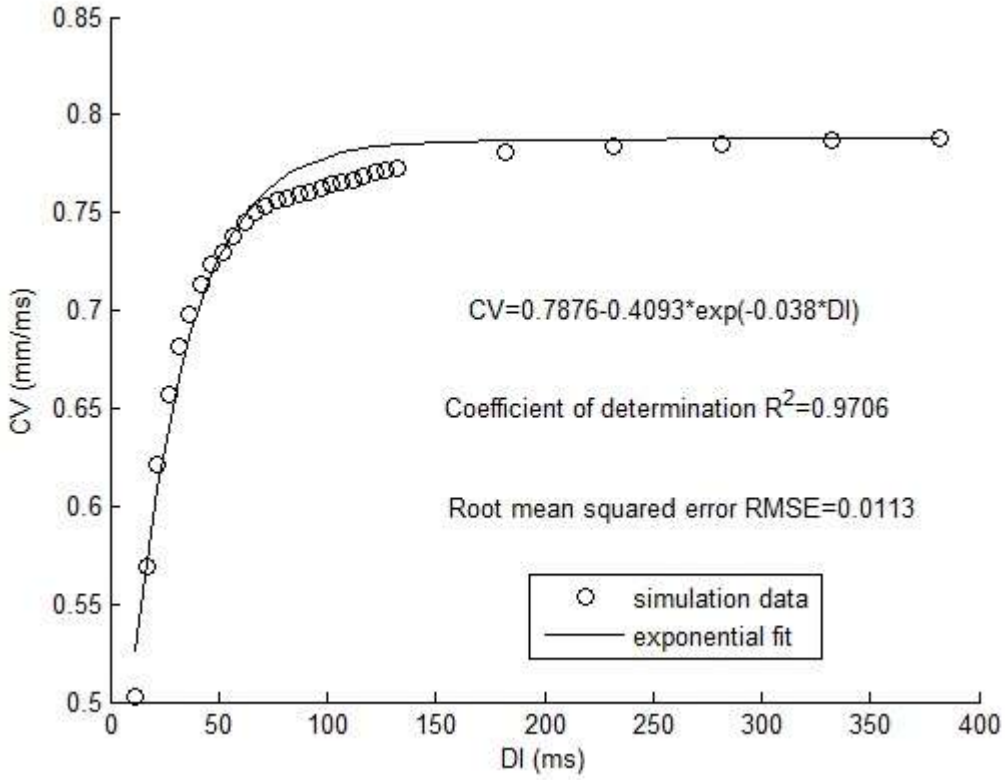

Figure 4.5: CV restitution (obtained from simulation studies based on human ventricular ion channel model (O'Hara et al., 2011)) and exponential curve fitted to the restitution data.

4.3 One-dimensional conduction model

As discussed above, one-dimensional ion channel model is too complicated for analyzing experimental data without detailed information of changes in ion currents and ion concentrations. In this project, simplified one-dimensional conduction model was used to build up CV restitution based on experimental data. This simplified one-dimensional model was developed based on the work of Fox, et al., in which the model is referred as coupled-map model (Fox et al., 2002).

If the length of a tissue unity (e.g. ventricular myocyte) is assumed as Δx, the activation time and repolarisation time of a cell x_i can be expressed as bellow:

Activation time: $AT_n(x_i) = AT_n(x_{i-1}) + \frac{\Delta x}{CV_n(x_{i-1})}$ (4.12)

Repolarisation time: $RT_n(x_i) = AT_n(x_i) + APD_n(x_i)$ (4.13)

Where, AT and RT are the activation time and repolarisation time; n is the number of beat.

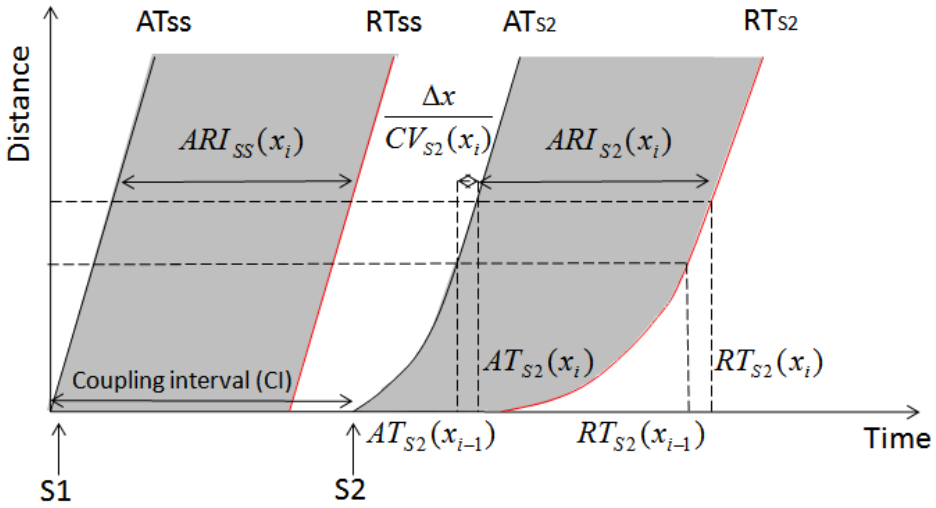

Figure 4.6: Diagram of activation conduction and repolarisation for steady-state beat (S_1) and premature beat (S_2). The black lines indicate propagations of activations, while the red lines represent repolarisation; shaded areas indicate the refractory periods for S_1 and S_2; x_i and x_{i-1} represent two adjacent sites with distance Δx.

Knowing the activation time at the stimulation site x_0 for beat S_n, the activation time and repolarisation time at cell x_i can be expressed as:

$$AT_n(x_i) = AT_n(x_0) + \sum_{j=0}^{i-1} \frac{\Delta x}{CV_n(x_j)} \tag{4.14}$$

$$RT_n(x_i) = AT_n(x_0) + \sum_{j=0}^{i-1} \frac{\Delta x}{CV_n(x_j)} + APD_n(x_i) \tag{4.15}$$

Thus, the period between activation n and activation n+1 for site x_i can be calculated as:

$$AT_{n+1}(x_i) - AT_n(x_i) = AT_{n+1}(x_0) - AT_{n+1}(x_0) + \sum_{j=0}^{i-1} \left(\frac{\Delta x}{CV_{n+1}(x_i)} - \frac{\Delta x}{CV_n(x_i)} \right) \tag{4.16}$$

Here, the period between activation n and activation n+1 for site x_0 equals to the coupling interval (CI_{n+1}) applied at site x_0 :

$$AT_{n+1}(x_0) - AT_n(x_0) = CI_{n+1} \tag{4.17}$$

For site x_i, the period between activation n and activation n+1 can be calculated as:

$$AT_{n+1}(x_i) - AT_n(x_i) = APD_n(x_i) + DI_{n+1}(x_i) \tag{4.18}$$

Combining equations 4.16-4.18, the basic equation for one-dimensional conduction model can be expressed as:

$$DI_{n+1}(x_i) = CI_{n+1} + \sum_{j=0}^{i-1} \left(\frac{\Delta x}{CV_{n+1}(x_j)} - \frac{\Delta x}{CV_n(x_j)} \right) - APD_n(x_i) \tag{4.19}$$

Corresponding to the experimental data, $DI_{n+1}(x_i)$ is the DI of premature beat S_2, APD_n is the APD of steady-state beat S1 ($APD_n = APD_{SS}$), CI_{n+1} is the coupling interval of

premature beat S_2. These three parameters were obtained directly from experimental data. $CV_n(x_i)$ is the steady-state conduction velocity (CV_{SS}).

For each investigated site, the activation conduction pathway from the pacing site to the investigated site was assumed to be an independent one-dimensional conduction pathway with uniform restitution properties. From the experimental data, the length of the conduction pathway can be calculated by the product of the steady-state conduction velocity and the steady-state conduction time ($AT_{SS}(x_i)$) form the stimulation site to the investigated site:

$$L(x_i) = CV_{SS} \cdot AT_{SS}(x_i) \tag{4.20}$$

Hence, the number of cells included in the conduction pathway can be calculated as $i = \frac{L(x_i)}{\Delta x}$.

Therefore, equation 4.19 can be changed into the following form relating to the experimental data:

$$DI_{S2}(x_i) + APD_{SS}(x_i) - CI_{S2} + AT_{SS}(x_i) = \sum_{j=0}^{i-1} \frac{\Delta x}{CV_{S2}(x_j)} \tag{4.21}$$

All the dynamics in the left hand side of equation 4.21 are those obtained from experimental data. For each investigated site, one-dimensional conduction model and CV restitution model can be fitted with dynamics from experimental data by adjusting B_{CV} and C_{CV} in equation 4.11 using the least-square method.

4.4 Condition for functional block

Based on one-dimensional conduction model and restitution properties, simulation of activation conduction and repolarisation enables analysis of function block by applying different coupling intervals of several premature beats (5 premature beats used in previous research (Fox et al., 2002, Fox et al., 2003, Otani, 2007)). The condition defined by Fox et al. is that function block occurs when DI is smaller than the minimum DI (2ms was used in Fox's study) (Fox et al., 2003). In Otani's work, repolarisation wavefront was compared with conduction velocity vectors (Otani, 2007). When conduction velocity vector runs into repolarisation wavefront, function block is initiated (as indicated by the green arrow in figure 4.7). Although both studies demonstrated that sequential premature beats can lead to functional block, it is not clear enough to show the relationship between interactions of restitution properties and initiation of functional block. In this section, condition for functional block is quantified by presenting a mathematical equation.

As shown in figure 4.7, at location x_i, minimum DI is reached for beat n+1. If the minimum conduction velocity is larger than the slope of repolarisation wavefront of beat n (as indicated by the green arrow), activation wavefront of beat n+1 "runs into" repolarisation wavefront, which consequently initiate functional block. In another case, if the minimum conduction velocity is smaller than the slope of repolarisation wavefront of beat n (as indicated by the black arrow). Activation wavefront will be separated with repolarisation wavefront of beat n, in which case no functional block occurs. Therefore, condition for functional block can be expressed as: if $\frac{dx}{dRT} < CV_{\min}$, function block can be initiated.

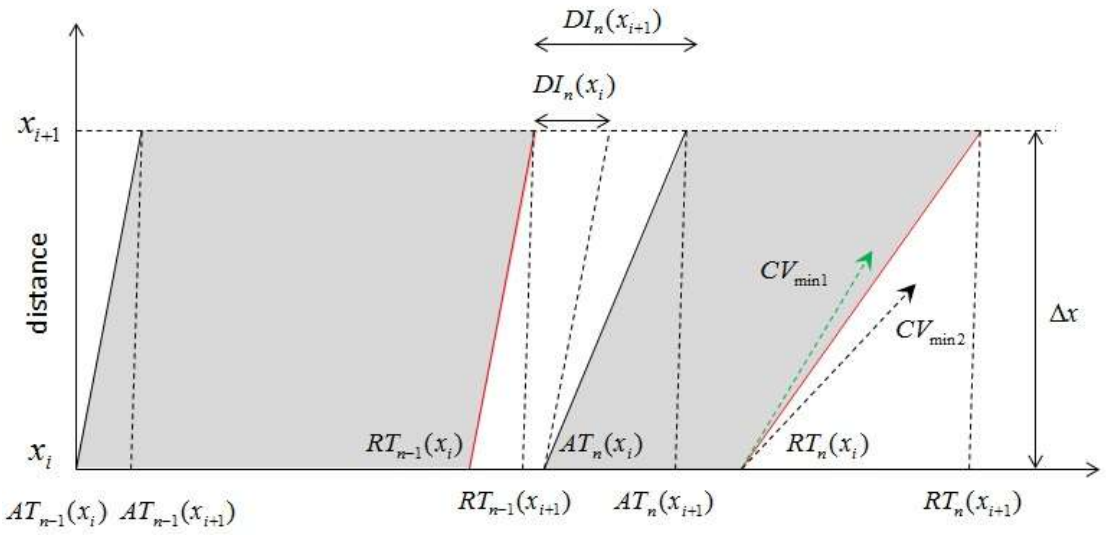

Figure 4.7: Diagram showing relationship of activation time and repolarisation time between two adjacent sites x_i and x_{i+1}. $CV_{\min 1}$ (green arrow) and $CV_{\min 2}$ (black arrow) indicate two situations with different minimum conduction velocities, in which $CV_{\min 1}$ will be blocked while $CV_{\min 2}$ will not be blocked; solid black lines indicate activation, while solid red lines indicate repolarisation; the gray areas represent the refractory period.

For two adjacent location x_i and x_{i+1}, referring to equation 4.13, the slope of repolarisation wavefront can be calculated as:

$$\frac{\Delta x}{RT_n(x_{i+1}) - RT_n(x_i)} = \frac{\Delta x}{AT_n(x_{i+1}) - AT_n(x_i) + APD_n(x_{i+1}) - APD_n(x_i)} \tag{4.22}$$

According to equation 4.12, variance between activation times of two sites can be expressed as:

$$AT_n(x_{i+1}) - AT_n(x_i) = \frac{\Delta x}{CV_n(x_i)} \tag{4.23}$$

Referring to APD restitution model (equation 4.9), the following relationship can be obtained:

$$APD_n(x_{i+1}) - APD_n(x_i) = -B_{APD} \cdot \exp(C_{APD} \cdot DI_n(x_{i+1})) + B_{APD} \cdot \exp(C_{APD} \cdot DI_n(x_i)) \quad (4.24)$$

According to equation 4.19,

$$DI_n(x_i) = CI_n + \sum_{j=0}^{i-1}\left(\frac{\Delta x}{CV_n(x_j)} - \frac{\Delta x}{CV_{n-1}(x_j)}\right) - APD_{n-1}(x_i) \quad (4.25)$$

$$DI_n(x_{i+1}) = CI_n + \sum_{j=0}^{i}\left(\frac{\Delta x}{CV_n(x_j)} - \frac{\Delta x}{CV_{n-1}(x_j)}\right) - APD_{n-1}(x_{i+1}) \quad (4.26)$$

Therefore, relationship between DIs of the two sites can be expressed as:

$$DI_n(x_{i+1}) = DI_n(x_i) + \frac{\Delta x}{CV_n(x_i)} - \frac{\Delta x}{CV_{n-1}(x_i)} - (APD_{n-1}(x_{i+1}) - APD_{n-1}(x_i)) \quad (4.27)$$

If beat n-1 is defined to be a steady-state beat (S_1), beat n is defined to be a premature beat (S_2), $APD_{n-1}(x_{i+1})$ and $APD_{n-1}(x_i)$ in equation 4.27 both equal to the steady-state APD (APD_{SS}), and $CV_{n-1}(x_i)$ equals to the steady-state conduction velocity (CV_{SS}). Consequently, equation 4.27 can be changed into the following equation:

$$DI_n(x_{i+1}) = DI_n(x_i) + \frac{\Delta x}{CV_n(x_i)} - \frac{\Delta x}{CV_{SS}} \quad (4.28)$$

Combining equations 4.22, 4.23, 4.24, 4.28, and the CV restitution model (equation 4.11), the slope of repolarisation wave-front can be expressed as:

$$\frac{\Delta x}{RT_n(x_{i+1}) - RT_n(x_i)} =$$

$$\frac{\Delta x}{\frac{\Delta x}{CV_n(x_i)} - B_{APD} \cdot \exp(C_{APD} \cdot (DI_n(x_i) + \frac{\Delta x}{CV_n(x_i)} - \frac{\Delta x}{CV_{SS}})) + B_{APD} \cdot \exp(C_{APD} \cdot DI_n(x_i))} \tag{4.29}$$

As Δx approaches 0, limit of equation 4.29 can be deduced using L'Hopital's rule:

$$\lim_{\Delta x \to 0} \frac{\Delta x}{RT_n(x_{i+1}) - RT_n(x_i)} =$$

$$\frac{1}{\frac{1}{CV_n(x_i)} - B_{APD} \cdot C_{APD} \cdot \exp(C_{APD} \cdot DI_n(x_i)) \cdot (\frac{1}{CV_n(x_i)} - \frac{1}{CV_{SS}})} \tag{4.30}$$

Therefore, a function F(DI) can be defined as:

$$F(DI) = \frac{1}{\frac{(1 + APD(DI)')}{CV(DI)} - \frac{APD(DI)'}{CV_{SS}}} - CV_{\min} \tag{4.31}$$

Where, $APD(DI)'$ is the slope of APD restitution curve at given DI:

$$APD(DI)' = -B_{APD} \cdot C_{APD} \cdot \exp(C_{APD} \cdot DI) \tag{4.32}$$

CV(DI) is the conduction velocity at given DI:

$$CV(DI) = CV_{SS} - B_{CV} \cdot \exp(C_{CV} \cdot DI) \tag{4.33}$$

The minimum conduction velocity $CV_{\min}$ can be calculated as:

$$CV_{\min} = CV_{SS} - B_{CV} \cdot \exp(C_{CV} \cdot DI_{\min}) \tag{4.34}$$

For a given DI, if F(DI) is smaller than 0, then functional block can be initiated. Otherwise, there will be no functional block. If there exist DIs, under which F(DI) is smaller than 0, a DI_{bound} can

be found under which $F(DI_{bound})$ equals to 0. Then, DI_{bound} can be defined as range of DI for S_2 within which functional block can be initiated if DI_{min} is reached at the location after the repolarisation.

In order to give an example, restitution properties obtained from ion channel model was used to calculate F(DI). Here, $DI_{\min}$ is defined to be 2ms. Restitution properties obtained from ion channel model are given in table 4.1. The calculated F(DI) is shown in figure 4.8, and DI_{bound} is 19.71ms. Referring to equation 4.31, when DI is very large, CV(DI) approaches CV_{SS}, in which case $F(DI) = CV_{SS} - CV_{\min}$. In this example, the maximum value for F(DI) is 0.3793 as indicated by the red dashed line in figure 4.8.

The physical meaning of F(DI) and DI_{bound} is the relationship between interactions of restitution properties and occurrence of functional block. Notably, F(DI) and DI_{bound} is calculated under the situation of one steady-state beat (S_1) followed by a premature beat (S_2). The possible appearance of functional block discussed here is after the repolarisation of S_2. Under the situation of sequential premature beats, $APD_{n-1}(x_{i+1}) - APD_{n-1}(x_i)$ in equation 4.27 does not equal to 0, and $CV_{n-1}(x_i)$ does not equal to CV_{SS}. These two are determined by accumulated effects of restitution interactions from all the previous premature beats.

Based on equation 4.31, it can be seen that the steepness of APD restitution curve and the value of conduction velocity are the key factor determining occurrence of functional block. For the steepness of APD restitution, the steeper the APD restitution curve is, the easier it is to initiate functional block. For CV restitution, under the same DI and CV_{SS}, the smaller the CV is, the easier it is to initiate functional block. These effects indicate how APD restitution and CV restitution are related with functional block on their own. It is the interactions of APD

restitution and CV restitution that determines occurrence of functional block. As for DI_{bound}, the larger it is, the more possibility there is for initiation of functional block.

APD restitution: $APD = APD_{SS} - B_{APD} \cdot \exp(C_{APD} \cdot DI)$		CV restitution: $CV = CV_{SS} - B_{CV} \cdot \exp(C_{CV} \cdot DI)$	
APD_{SS}	218.2	CV_{SS}	0.7876
B_{APD}	35.0667	B_{CV}	0.4093
C_{APD}	-0.0088	C_{CV}	-0.038

Table 4.1: Restitution properties obtained from simulation based on ion channel model (O'Hara et al., 2011)

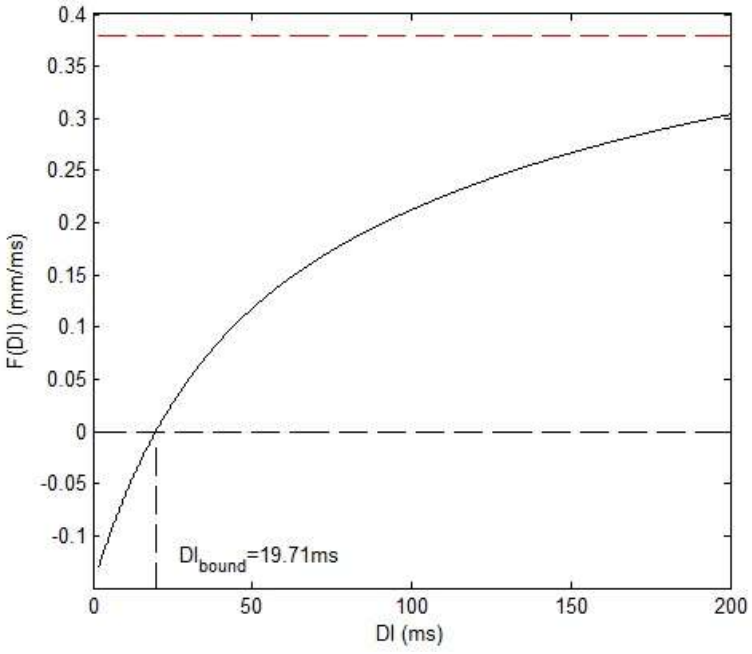

Figure 4.8: Diagram of function for condition of functional block (F(DI)) calculated based on restitution properties obtained from ion channel model (as shown in table 4.1).

4.5 Influence of cellular ionic properties on APD restitution

As discussed in section 4.1, APD restitution properties are determined by cellular ionic properties. Using ion channel model simulation studies, influences of cellular ionic properties on APD restitution properties were investigated. Theoretically, if the initial conditions such as cellular ion concentrations and gate variables and equations for gating variables remain unchanged, the APD restitution properties remain the same. Hence, ion channel model can be fitted with APD restitution properties by adjusting parameters and variables inside the model. Obviously, it is extremely difficult to fit the whole ion channel model with experimental data for APD restitution, because too many conditions and variables are included in the ion channel model not to say the amount of equations for gate variable. Similar to section 4.1, some key parameters determining APD restitution properties were selected. Ion channel model was fitted with experimental data of APD restitution by only adjusting these key parameters. Although this fitted model may not be accurate enough to describe the realistic cellular ionic properties of cardiac tissue, it still can demonstrate heterogeneity of cellular ionic properties across the inner surface of the ventricle, based which further work can be made in terms of two-dimensional conduction simulation studies.

In the following sections, initial conditions for ion concentrations and gate variables in ORd model presented in section 2.4.4 were changed in order to study the influences of these parameters on APD restitution properties. For each investigated parameter, its initial condition was changed by applying certain different values, while all the other initial condition of ORd model remained the same as listed in table A.11.1. Simulations were made using S_1-S_2 protocol, in which 5 steady-state beats (coupling interval=600ms) were introduced before one premature beat was introduced. Slope of APD restitution curve is calculated based on the fitted exponential model (equation 4.9) at DI=10ms:

$$slope_{APD} = -B_{APD} \cdot C_{APD} \cdot \exp(C_{APD} \cdot DI) \tag{4.35}$$

4.5.1 Intracellular ion concentrations ($[Na^+]_i$, $[K^+]_i$, and $[Ca^{2+}]_i$)

The initial condition for intracellular sodium ion concentration applied in the ORd model range from 3.615mM to 14.46mM as shown in table 4.2. As discussed in section 2.2.2, the biggest contribution of sodium ion is the formation of fast inward Sodium current that depolarizes the membrane at a fast rate (AP upstroke), compared with its other contributions such as Sodium/Calcium exchange current, Sodium/Potassium ATPase current and background current. The simulation results (figure 4.9) indicated that variation in $[Na^+]_i$ has certain influence on the steady-state APD (APD_{SS}), however the maximum slope of the APD restitution curve is relatively less affected (standard deviation: 1.1873 for APD_{SS} compared with 0.0066 for slope of APD restitution curve). Generally speaking, $[Na^+]_i$ on APD only has limited effect on ADP restitution properties

Similar to $[Na^+]_i$, intracellular Potassium ion concentration ($[K^+]_i$) also has limited influence on APD restitution properties (larger impact on APD_{SS}, and relatively little influence on the steepness of APD restitution curve) as shown in table 4.3. As for intracellular Calcium ion concentration ($[Ca^+]_i$), it almost has no influence on APD restitution properties (as indicated in table 4.4). Consequently, it can be summarized that intracellular ion concentrations only have limited effect on APD restitution properties. The main function of ion concentrations is to maintain the resting potential.

	$[Na^+]_i$ (mM)	Resting potential (mV)	APD_{SS} (ms)	B_{APD}	C_{APD}	Slope of APD restitution curve (DI=10ms)
	3.615	-88.3201	219	34.3257	-0.0089	0.28
	5.061	-88.5727	218.7	34.2487	-0.0087	0.273
	7.23	-88.9493	218.2	35.0667	-0.0088	0.283
	8.676	-89.1989	217.6	34.4608	-0.0087	0.2742
	10.845	-89.5720	216.6	34.8953	-0.0091	0.2886
	14.46	-90.1903	216	34.72	-0.0085	0.2717
Mean	8.3145	-89.1339	217.6833	34.6195	-0.0088	0.2784
SD	3.9534	0.6817	1.1873	0.3272	0.000204	0.0066

Table 4.2: Influence of intracellular Sodium ion concentration on APD restitution properties. SD: standard deviation; slope of APD restitution is calculated at DI=10ms. Shaded row indicates initial conditions used in simulation studies are the same with those in ORd model (O'Hara et al., 2011).

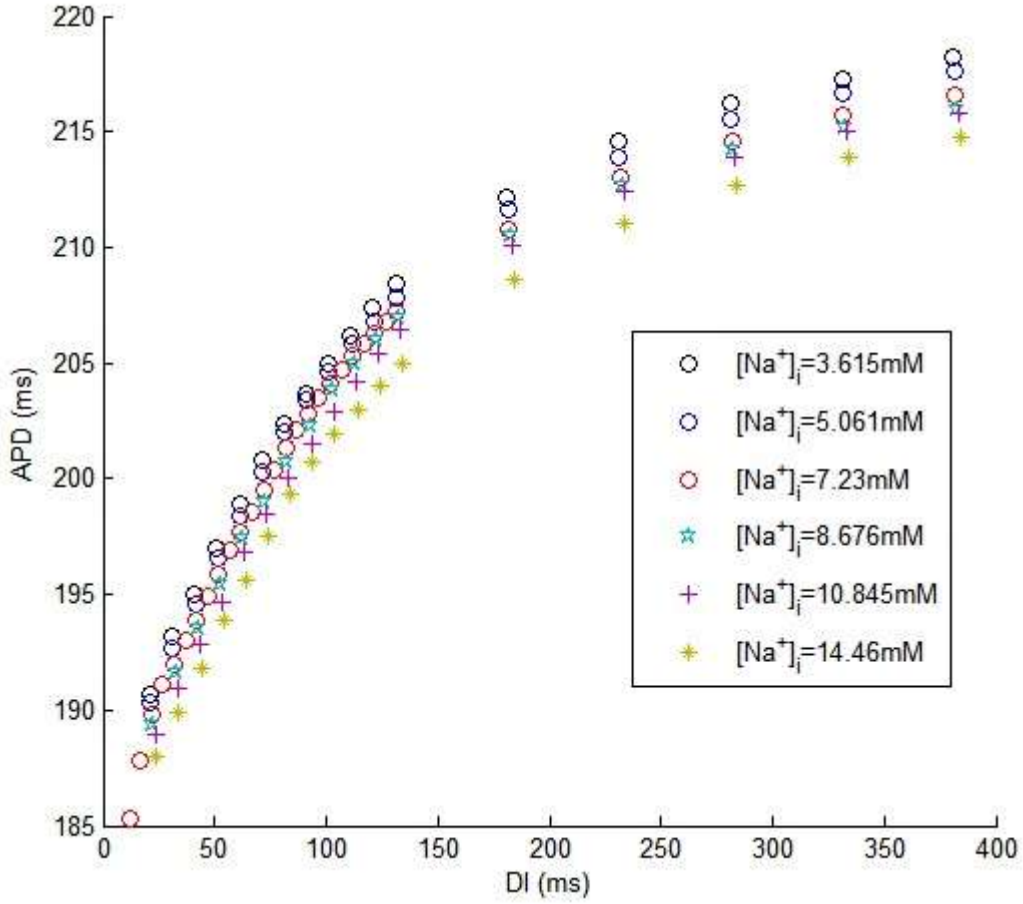

Figure 4.9: Influence of intracellular Sodium ion concentration on APD restitution properties. Restitution simulation studies were carried out under S_1-S_2 protocol (steady-state coupling interval=600ms).

	$[K^+]_i$ (mM)	Resting potential (mV)	APD_{SS} (ms)	B_{APD}	C_{APD}	Slope of APD restitution curve (DI=10ms)
	115.032	-87.84	230.1	32.9476	-0.0097	0.2908
	143.79	-88.9493	218.2	35.0667	-0.0088	0.283
	158.169	-91.3917	214.1	34.9371	-0.0085	0.2735
	172.548	-93.7706	210.8	34.8432	-0.0087	0.2767
	210.306	-97.5413	210.9	32.2078	-0.0079	0.2363
Mean	159.969	-91.8986	216.82	34.0004	-0.0087	0.2721
SD	35.2717	3.8978	8.0148	1.3273	0.00065	0.0211

Table 4.3: Influence of intracellular Potassium ion concentration on APD restitution properties. SD: standard deviation; slope of APD restitution is calculated at DI=10ms. Shaded row indicates initial conditions used in simulation studies are the same with those in ORd model (O'Hara et al., 2011).

	$[Ca^{2+}]_i$ (mM)	Resting potential (mV)	APD_{SS} (ms)	B_{APD}	C_{APD}	Slope of APD restitution curve (DI=10ms)
	4.27	-88.9473	218.2	34.3695	-0.0085	0.2667
	5.978	-88.9481	218.2	34.2618	-0.0085	0.2674
	8.54	-88.9493	218.2	35.0667	-0.0088	0.283
	10.248	-88.95	218.2	34.2618	-0.0085	0.2674
	12.81	-88.951	218.2	34.2493	-0.0085	0.2671
	17.08	-88.9525	218.2	34.2271	-0.0085	0.2665
Mean	9.821	-88.9497	218.2	34.3894	-0.0086	0.2669
SD	4.6697	0.0019	0	0.3322	0.0001	0.0065

Table 4.4: Influence of intracellular Calcium ion concentration on APD restitution properties. SD: standard deviation; slope of APD restitution is calculated at DI=10ms. Shaded row indicates initial conditions used in simulation studies are the same with those in ORd model (O'Hara et al., 2011).

4.5.2 L-type calcium current (I_{CaL})

As discussed in section 2.2.2, L-type calcium current is responsible for maintaining the plateau of AP after the fast upstroke. Research showed that APD is mainly determined by currents that are sensitive to $[Ca^{2+}]_i$ (L-type Calcium current, Sodium/Calcium exchange current et al.)

(Zhong et al., 1997, Linz and Meyer, 1998, Goldhaber et al., 2005). In this section, effect of L-type calcium current on APD restitution properties was investigated. As discussed in section 4.1, slow development of Ca^{2+} dependent inactivation gate ($f_{Ca,slow}$) for Ca^{2+} current through the L-type Ca^{2+} channel is highly related with APD. Hence, studies made here mainly focused on changes of parameters in gate functions (equation 4.3-4.5).

	C_4	Resting potential (mV)	APD_{SS} (ms)	B_{APD}	C_{APD}	Slope of APD restitution curve (DI=10ms)
	7.832	-89.0505	235	26.4207	-0.0074	0.1827
	13.706	-89.0261	228.3	31.2343	-0.0086	0.2457
	19.58	-88.9493	218.2	35.0667	-0.0088	0.283
	39.16	-89.0179	226	53.8556	-0.0107	0.5157
	58.74	-89.0179	225.3	81.9507	-0.0123	0.8911
	78.32	-89.0134	220.5	111.2794	-0.0131	1.2785
Mean	36.223	-89.0125	225.55	56.6346	-0.0102	0.5661
SD	27.8491	0.037	5.944	33.639	0.0023	0.4349

Table 4.5: Influence of gate variable on APD restitution properties (C_4 in equation 4.3). SD: standard deviation; slope of APD restitution is calculated at DI=10ms. Shaded row indicates initial conditions used in simulation studies are the same with those in ORd model (O'Hara et al., 2011).

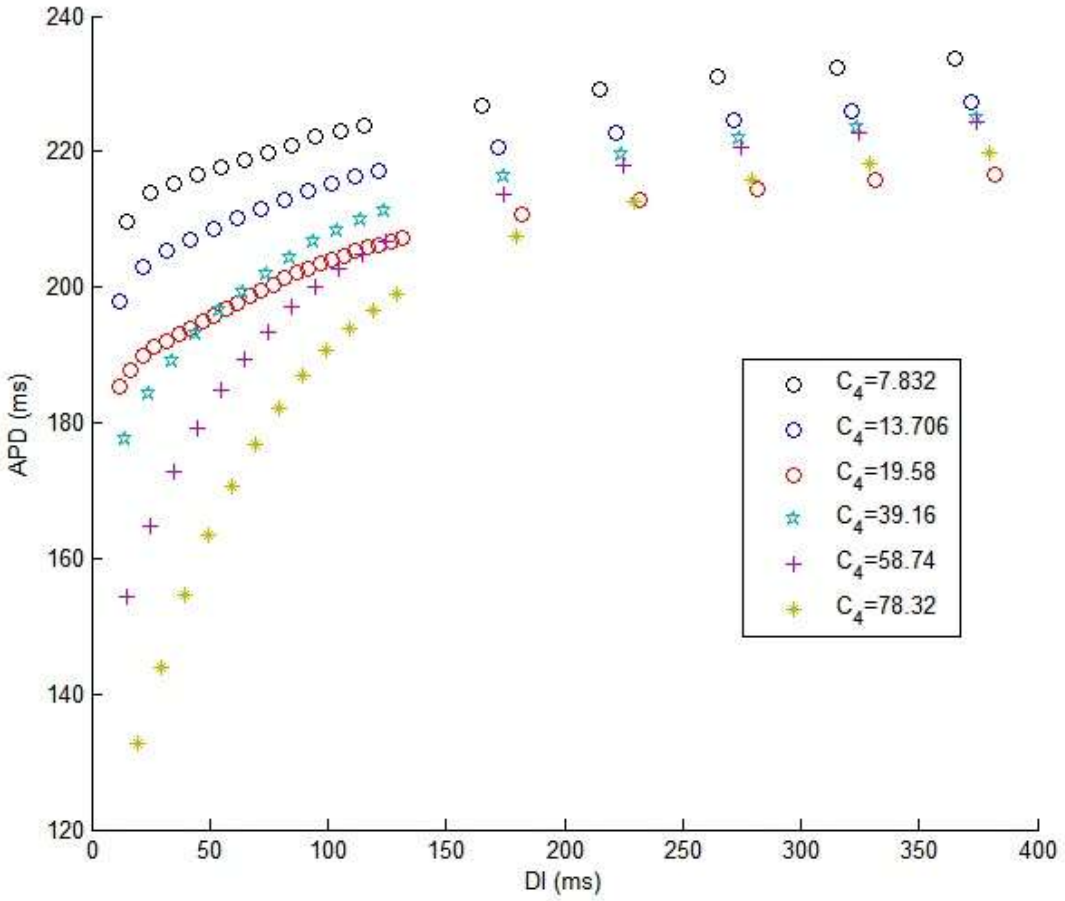

Figure 4.10: Influence of gate variable on APD restitution properties (C_4 in equation 4.3). Restitution simulation studies were carried out under S_1-S_2 protocol (steady-state coupling interval=600ms)

As shown in table 4.5 and 4.6, the two constants (C_4 and C_5) in equation 4.3 play different roles in determining APD restitution properties: C_4 are highly related with steepness of APD restitution curve (positive relationship between C_4 and the steepness of APD restitution curve as shown in figure 4.10); C_5 are responsible for change in steady-state APD (positive relationship between C_5 and APD_{SS}). Consequently, these two constants together with C_6-C_9 (see appendix) in equation 4.4 can be regarded as the key determinants of APD restitution properties, and be used to fit the ion channel model with APD experimental data.

	C_5	Resting potential (mV)	APD_{SS} (ms)	B_{APD}	C_{APD}	Slope of APD restitution curve (DI=10ms)
	1.848	-89.0196	226.7	34.8048	-0.009	0.2856
	3.696	-88.9493	218.2	35.0667	-0.0088	0.283
	5.544	-89.0245	228.0	35.6281	-0.0091	0.2959
	7.392	-89.0332	231.6	36.3096	-0.0093	0.3075
	11.088	-89.0654	247.1	35.9425	-0.0091	0.2978
	14.784	-89.1131	278	37.3857	-0.0091	0.3119
Mean	7.392	-89.0342	238.2708	35.8562	-0.0091	0.297
SD	4.819	0.0542	21.6452	0.9309	0.00016	0.0115

Table 4.6: Influence of gate variable on APD restitution properties (C_5 in equation 4.3). SD: standard deviation; slope of APD restitution is calculated at DI=10ms. Shaded row indicates initial conditions used in simulation studies are the same with those in ORd model (O'Hara et al., 2011).

4.6 Conclusion

The purpose of this chapter was to describe the development of restitution models and one-dimensional conduction model. The modelling method presented in this project is founded on the work of Gilmour's group (Otani, 2007, Fox et al., 2002, Fox et al., 2003, Gilmour et al., 2007). Research of this group provided initial validation of the use of one-dimensional conduction simulation in biological systems to predict whether large variations of long-short coupling intervals would induce VF. These models were enhanced in this project by fully deriving APD and CV restitution, which allows better approximation to the

activation wavefront and observation of the heterogeneity introduced by sequential extra-stimuli. Furthermore, a function describing condition for functional block was defined based on which a quantitative parameter could be obtained representing the likelihood of functional block initiation.

Validation of the restitution models on extra-stimuli was carried out by comparing simulation result with clinically acquired data (S_1-S_2-S_3 protocol), which showed that restitution models can well predict conduction time of extra-stimuli. Consequently, the function developed for condition of functional block as described in section 4.4 can be applied based on constructed restitution properties, demonstrating how interactions of restitution properties are related with initiation of functional block.

In this chapter, influences of cellular ionic properties on APD restitution were discussed aiming to provide an appropriate method to fit ion channel model with patient-specific APD restitution data. Although this process is far more computationally expensive than the one-dimensional conduction model, it has the potential of carrying out simulation studies on the inner surface of the ventricle, which can simulate formation of re-entry and spiral wave based on patient-specific data.

5 Modelling restitution properties based on experimental data

5.1 Introduction

The methods for modelling restitution properties based on experimental data have been described in chapter 4. This chapter presents the results of restitution modelling, aiming to demonstrate that the complex dynamic interactions between activation and repolarisation induced by sequential extrastimuli can be approximated in terms of APD and CV restitution. For APD restitution model, the derived exponential model was directly fitted with APD restitution obtained from waveform analysis of the electrograms using the method of least squares. For CV restitution, one-dimensional conduction model was used to fit the simulated conduction time from the stimulation site to the investigated site ($\sum_{j=0}^{i-1}\frac{\Delta x}{CV(x_j)}$) to the experimental data of conduction time (left-hand side of equation 4.21).

After restitution properties were constructed from experimental data, simulations of extra stimuli (S_3) were carried out and compared with experimental data of conduction time for extra stimuli in patient data undergoing extra stimuli experiment. This serves as a validation of the restitution models. Moreover, human ventricular ion model (ORd model) was used to simulate extra stimuli, which was compared with simulation result based on restitution models for the purpose of model validation.

Experimental data and restitution properties were visualised using three-dimensional colormap. This procedure provides a more vividly way to present the pattern of activation conduction and dispersion of repolarisation. Also, with the modelled restitution properties, three-dimensional visualisation can well demonstrate heterogeneity of restitution properties,

and be used to indentify regions that exists obvious difference compared with other parts of the ventricle.

5.2 Modelling APD restitution properties

Based on the experimental datasets, 44 patients were successfully modelled, which include 14 patients with Arrhythmogenic Right Ventricular Cardiomyopathy (ARVC), and 6 patients undergoing extra-stimuli (S_1-S_2-S_3) experiment. Table 5.1 showed modelling result of 6 patients (2 patients from each group) as an example. Detailed results for all 44 patients were listed in appendix. Standard deviation (SD) was calculated to show how much dispersion exists from the average value of investigated parameters. Coefficient of determination (R^2) and root mean squared error (RMSE) were used to evaluate the difference between the experimental data and modelled APD. Examples of restitution curves are given in figure 5.2.

Slopes of APD restitution curve were calculated based on equation 4.35 defining DI to be 10ms. The reason for using a fixed value for DI is that the minimum DI for different sites varies depending on their distances from the stimulation site (Hanson et al., 2009). Site close to the stimulation site has larger chance of reaching smaller DI compared with those far away from the stimulation site. Using a fixed value for DI ensures that the steepness of different curves can be compared under the same condition. Based on the results of APD restitution modelling, some simple analysis can be made. E.g., as shown in table 5.1, SD of APD_{SS} represents the heterogeneity of APD_{SS} across the investigated area. Comparing patient 1 with patient2, it can be seen that dispersion of APD_{SS} in patient 1 is larger than in patient 2. Similarly, the steepness of APD restitution curve varies more in patient 1 than in patient 2. According to restitution hypothesis, patient 1 is more risky than patient 2 in terms of wave-break initiation.

Patient ID		1	2	3	4	5	6
Number of electrode		93	93	24	24	28	28
APD_{SS} (ms)	Max	198.1	239.2	224.2	262.8	359.5	266.5
	Min	120.9	197.2	187.6	214.7	237.9	168.9
	Mean	164.9	218.5	207.1	233.2	264.8	212.9
	SD	18.5	11.0	9.8	9.5	30.4	20.3
slope of APD restitution curve (at DI=10ms)	Max	13.773	13.353	2.934	5.813	11.412	40.082
	Min	0.071	0.097	0.216	0.049	0.224	0.670
	Mean	2.098	1.044	1.212	0.971	1.501	9.281
	SD	3.195	1.940	0.854	1.672	2.496	10.070
Coefficient of Determination (R^2) for APD restitution modeling	Max	0.980	0.909	0.880	0.937	0.971	0.977
	Min	0.702	0.707	0.722	0.718	0.701	0.730
	Mean	0.867	0.807	0.802	0.819	0.883	0.905
	SD	0.091	0.065	0.067	0.080	0.092	0.074
Root Mean Squared Error (RMSE) for APD restitution modeling	Max	51.492	41.727	23.860	13.479	16.392	11.390
	Min	0.908	4.531	7.381	1.149	4.040	2.858
	Mean	10.828	11.923	12.158	5.612	8.536	4.763
	SD	10.468	5.804	3.329	3.940	3.464	1.984

Table 5.1: Examples of APD restitution modelling results. Patient 1 and 2 are normal patients undergoing cardiac studies; Patient 3 and 4 are patients with ARVC (Arrhythmogenic Right Ventricular Cardiomyopathy); patient 5 and 6 are patients undergoing S_1-S_2-S_3 experiment.

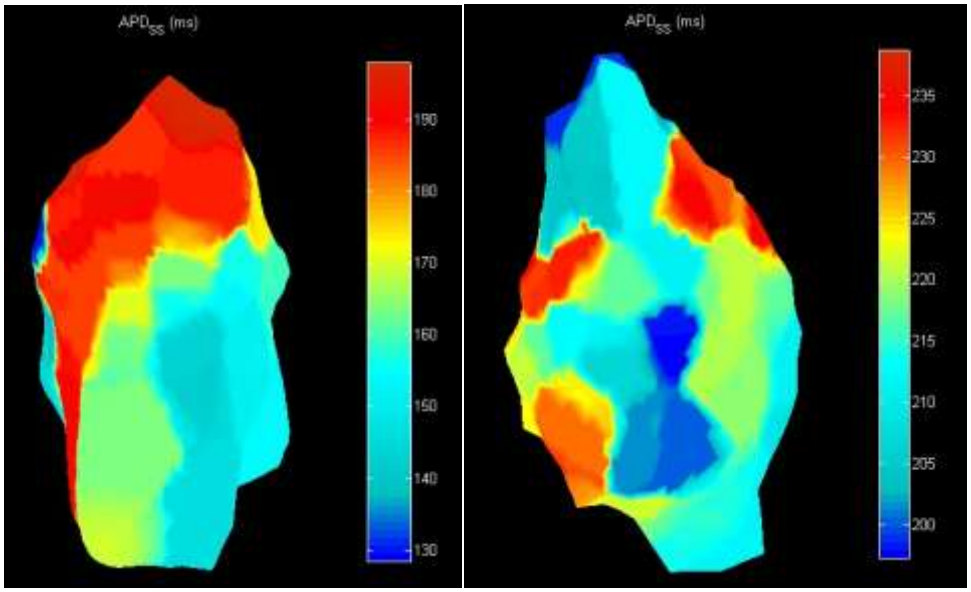

(a) (b)

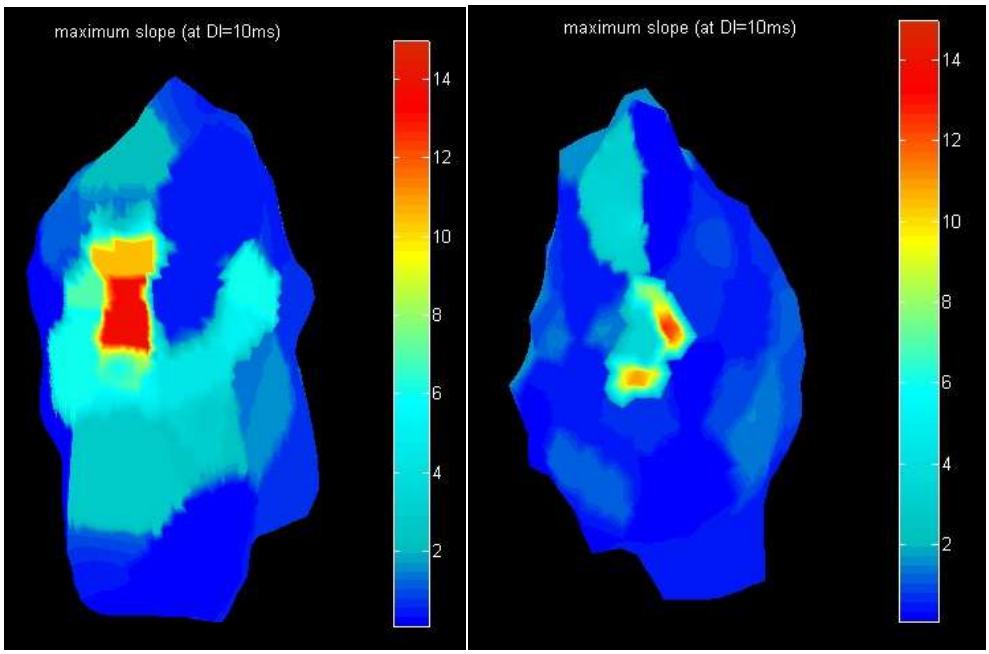

(c) (d)

Figure 5.1: Three-dimensional visualisation of APD restitution properties (steady-state APD and slope of APD restitution curve) across the endocardial surface from one ventricle. The slope of APD restitution curve is calculated at DI=10ms. (a) and (c) are three-dimensional colormaps of APD_{SS} and slope of APD restitution curve of patient 1 as listed in table 5.1; (b) and (d) are three-dimensional colormaps of APD_{SS} and slope of APD restitution curve of patient 2 as listed in table 5.1.

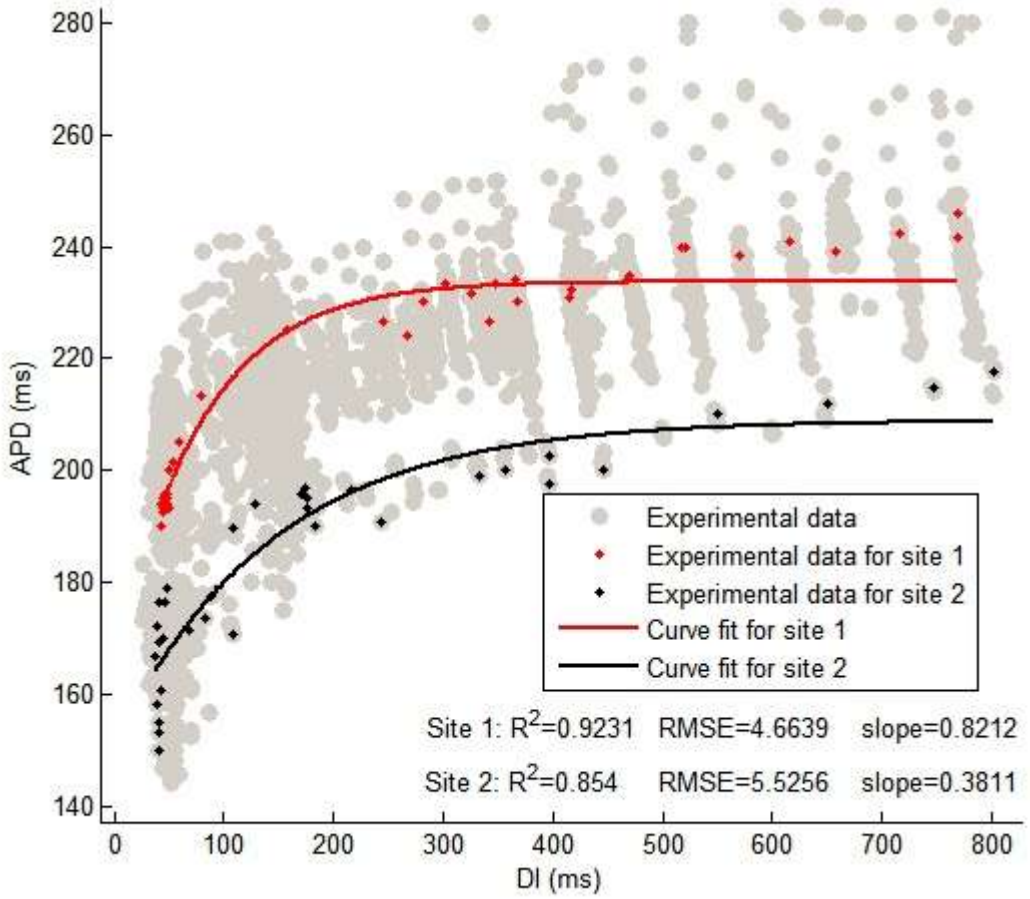

Figure 5.2: APD restitution curves. Gray points are APD restitution data for all the investigated sites; two sites were selected to demonstrate APD restitution curve fit (as indicated by red points and black points); slopes of APD restitution curves were calculated at DI=10ms.

Three-dimensional visualisation of APD restitution properties (as shown in figure 5.1) enabled identification of areas that are potentially risky for wave-break and re-entry. The individual patient's ventricular geometry has been obtained by a mapping catheter, which was stored and exported together with the electrogram data. Based on restitution hypothesis, steep APD restitution could lead to wave-break and re-entry. In figure 5.1, comparison can be made between two patients: in patient 1, there's a large area with steep APD restitution (figure 5.1(c)); in patient 2 the region of steep APD restitution is relatively smaller (figure 5.1(d)). Moreover, the dispersion of APD_{SS} in patient 1 (figure 5.1(a)) is larger than the one in patient 2

(figure 5.1(b)). Therefore, it can be concluded that patient 1 might be more risky in terms of wave-break initiation than patient 2.

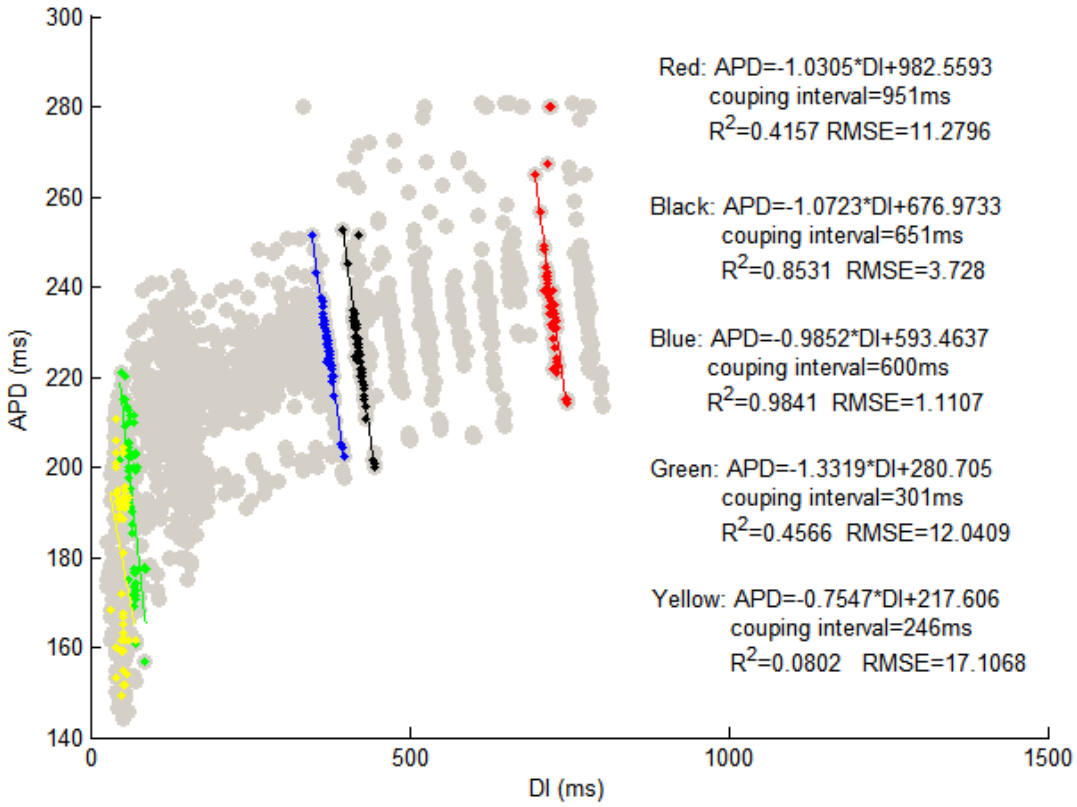

Figure 5.3: Relationship between APD and DI across the surface of the ventricle under same coupling interval. Linear regression lines are shown under five chosen coupling interval as example. Gray points demonstrate all the experimental data for APD restitution.

Analyses and visualisations made above were based on simple comparisons of APD restitution properties (APD_{SS}, steepness of APD restitution curve, and their dispersion), demonstrating mainly the effect of heterogeneity of APD restitution properties. In 2009, Hanson et al. (Hanson et al., 2009) presented a method for analysing the effect of APD restitution properties by investigating the relationship between APD and DI across the surface of the ventricle under the same coupling interval (as shown in figure 5.3). It has been shown that APD and DI for sites

across the surface of the ventricle possess a linear relationship, and the slope of linear regression line has a slope of -1 under the steady-state coupling interval; as the coupling interval shortened, the slope of regression line was progressively increased (Hanson et al., 2009).

As shown in figure 5.3, under the steady-state coupling interval (600ms), the regression line has a slope of -0.9852 (R^2=0.9841, RMSE=1.1107), and it can be approximated that the sum of ARI and DI equals to the steady-state coupling interval. As the coupling interval shortened, the coefficient of determination for linear regression decreased. This is a result of APD restitution properties: as DIs are decreased, reduction in APDs for different sites varies due to the difference of APD restitution properties. Consequently, this linear relationship is greatly influenced by the heterogeneity of APD restitution properties as DI shortens. R^2 and RMSE of linear regression under the smallest coupling interval can be used to evaluate the heterogeneity of APD caused by APD restitution: small R^2 and large RMSE indicate large heterogeneity of APD. Results for all patients are shown in figure 5.4.

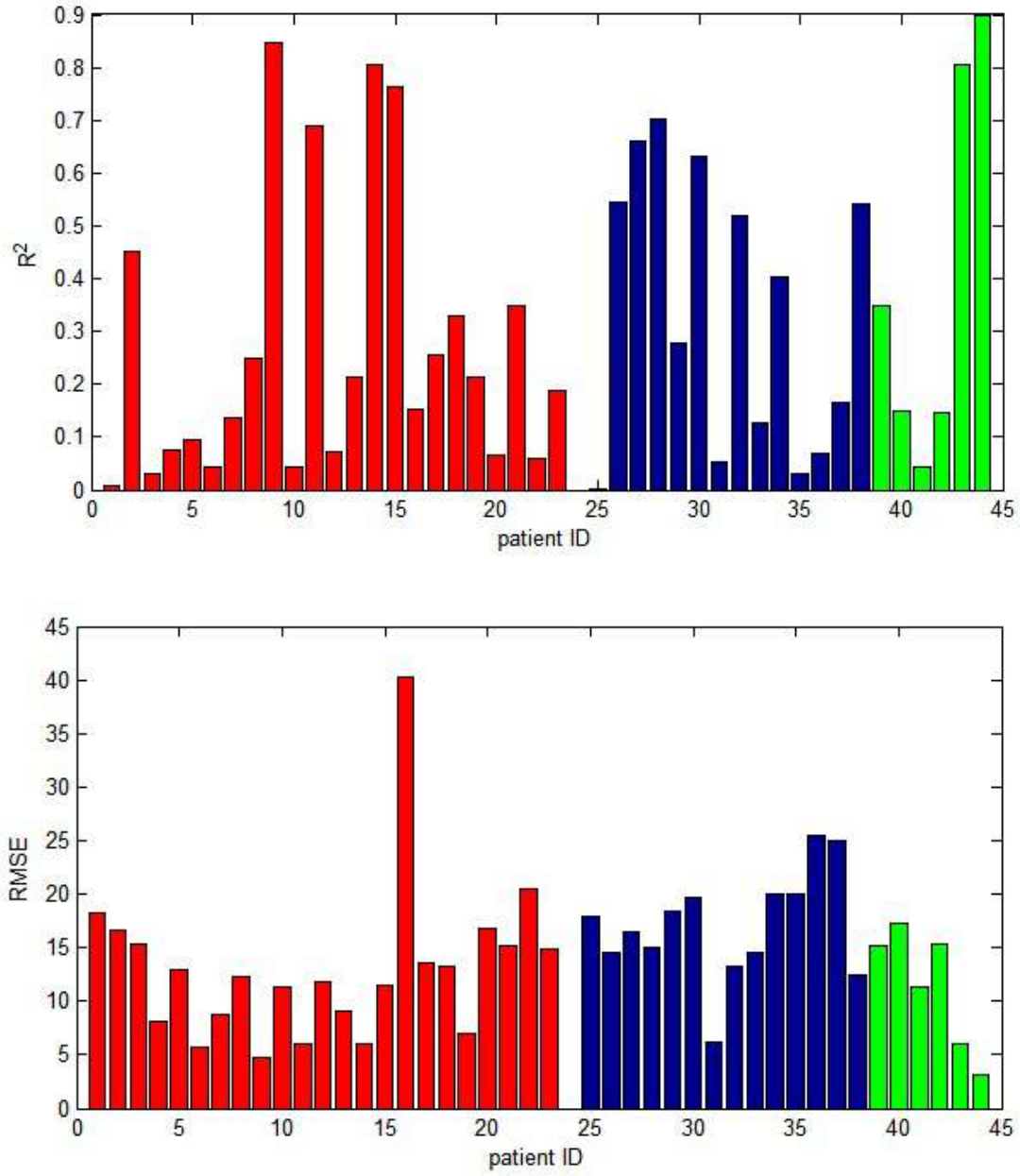

Figure 5.4: Bar graph of R^2 and RMSE of linear regression fit between APD and DI under the smallest coupling interval. Red: group of normal patient; blue: group of ARVC patient; green: patients undergoing extra-stimuli experiment; in the group of normal patient, calculation of one patient was ignored because there are only two sites.

5.3 Modelling CV restitution properties

The method used for modelling CV restitution has been discussed previously in section 4.2 and 4.3. Unlike APD restitution data that can be directly obtained from electrogram analysis, conduction velocity cannot be directly measured or calculated without knowing the anatomic structure of the ventricle and the exact conduction pathway from the stimulation site to the investigated site. In order to model CV restitution properties, it is assumed a one-dimensional conduction pathway from the stimulation site to the investigated site exists and remains constant for all activation conduction, and the CV restitution properties along this conduction pathway are uniform. Based on this assumption, CV restitution can be modelled using CV restitution model (equation 4.11) and one-dimensional conduction model (equation 4.21).

Despite the basic equations for CV restitution modelling as shown by equation 4.11 and 4.21, initial conditions for DI at the stimulation site ($DI_{S2}(x_0)$) need to be defined in order to calculate the simulated activation time. (Here, the activation time is defined to be the conduction time of activation signal from the stimulation site to the investigated site.) The minimum DI at the stimulation site under the smallest coupling interval is defined to be 2ms referring to previous research (Fox et al., 2002, Fox et al., 2003). Consequently, $DI_{S2}(x_0)$ under different coupling interval (CI) can be calculated as:

$$DI_{S2}(x_0) = CI - CI_{\min} + 2 \tag{5.1}$$

The cell length (Δx) is defined to be 0.1. Based on equation 4.28, DI at site x_i ($DI_{S2}(x_i)$) can be calculated as:

$$DI_{S2}(x_i) = DI_{S2}(x_{i-1}) + \frac{\Delta x}{CV_{S2}(x_{i-1})} - \frac{\Delta x}{CV_{SS}} \tag{5.2}$$

Consequently, under each coupling interval, simulated activation time for each investigated site ($\sum_{j=0}^{i-1}\frac{\Delta x}{CV(x_j)}$) can be calculated based on equation 5.1, 5.2, and CV restitution model (equation 4.11). By fitting this simulated activation time with experimental data (equation 4.21) using the method of least squares, CV restitution properties were modelled (examples were shown in figure 5.6).

As shown in table 5.2, 6 patients same as table 5.1 were listed as an example. Results for all patients are given in supplemental materials. Here, coefficient of determination (R^2) and root mean squared error (RMSE) were calculated by comparing simulated activation time with experimental data. The maximum and minimum values of steady-state activation times (AT_{SS}) and premature beat activation times (AT_{S2}) under the minimum coupling interval were listed for the purpose of comparison.

As shown in table 5.2, the maximum and minimum values of AT_{S2} are both larger than those of AT_{SS} (152.500ms and 100.833ms compared with 87.583ms and 54.118ms). This is a clear sign of the effect of CV restitution: as the coupling interval shortens, CV decreases, which lead to increase of conduction time. Figure 5.5 showed the three-dimensional visualisation of this phenomenon caused by CV restitution: as the coupling interval shortened, it took longer for the activation signal to be conducted across the surface.

Patient ID		1	2	3	4	5	6
AT_{SS} (ms)	Max	87.6	107.2	100.6	125.3	129.7	128.5
	Min	54.1	56.7	45.3	65.3	19.8	9.5
	Δ	33.5	50.5	55.3	60.1	109.8	119.0
AT_{S2} (ms) under the minimum coupling interval	Max	152.5	135.0	166.7	194.0	176.0	153.0
	Min	100.8	85.0	100.0	131.7	42.0	41.0
	Δ	51.7	50.0	66.7	62.3	134.0	112.0
Coefficent of Determination R^2	Max	0.962	0.949	0.934	0.959	0.976	0.979
	Min	0.796	0.706	0.816	0.715	0.724	0.709
	Mean	0.883	0.816	0.896	0.907	0.892	0.853
	SD	0.034	0.063	0.028	0.048	0.054	0.088
Root Mean Squared Error (RMSE)	Max	13.272	20.857	9.512	11.254	10.545	7.726
	Min	4.183	2.103	4.759	4.776	1.830	1.849
	Mean	7.021	5.601	6.187	6.745	7.486	5.134
	SD	1.793	3.328	1.045	1.453	2.509	1.872

Table 5.2: Examples of CV restitution modelling results. Δ represents the variance between the maximum activation time and minimum activation time for investigated sites; R^2 and RMSE were calculated by comparing the simulated activation time with experimental data of activation time; patients are the same with those listed in table 5.1.

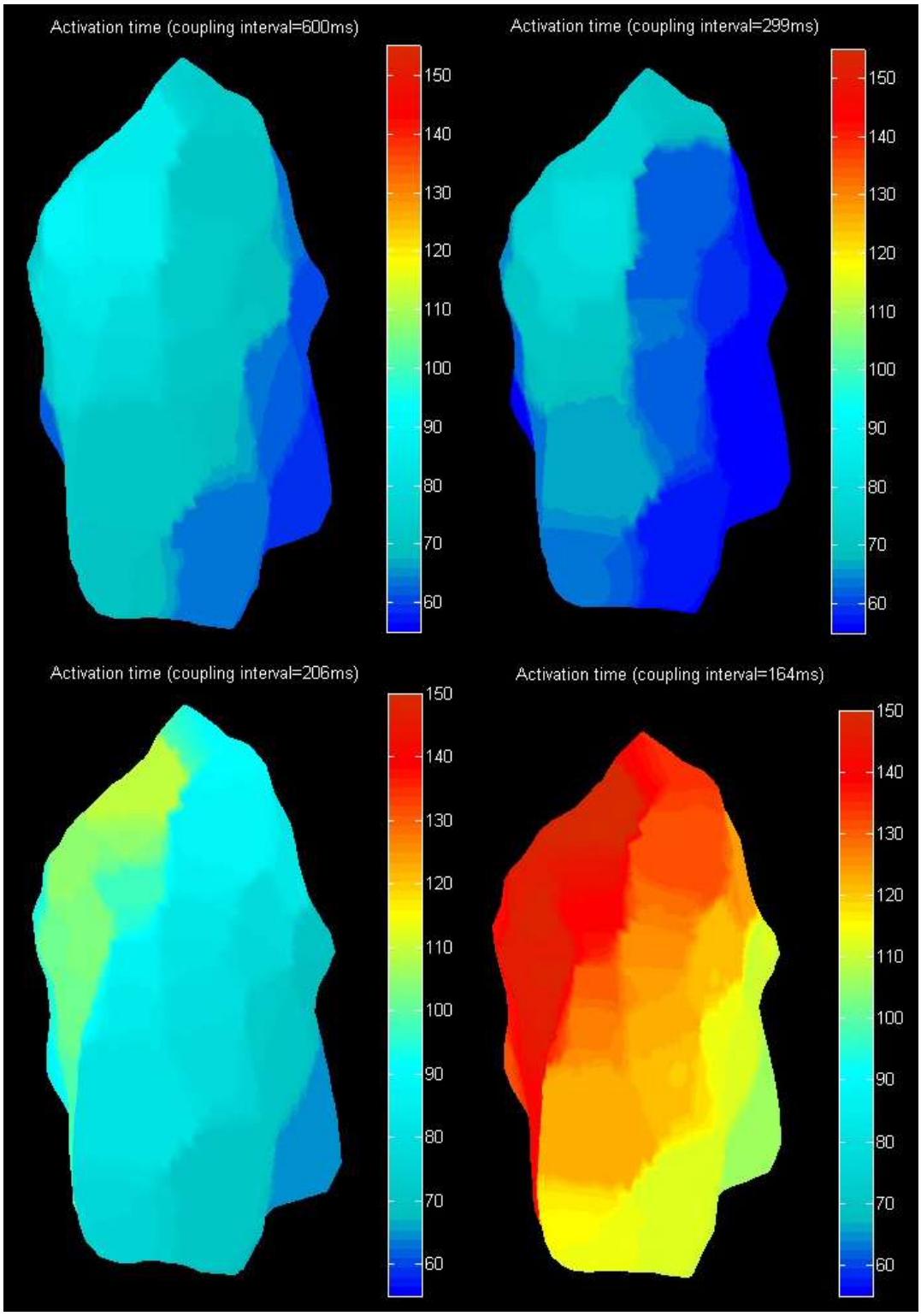

Figure 5.5: Three-dimensional visualisation of activation time under different coupling intervals (S_2, patient 1). Steady-state coupling interval is 600ms; the minimum coupling interval is 164ms.

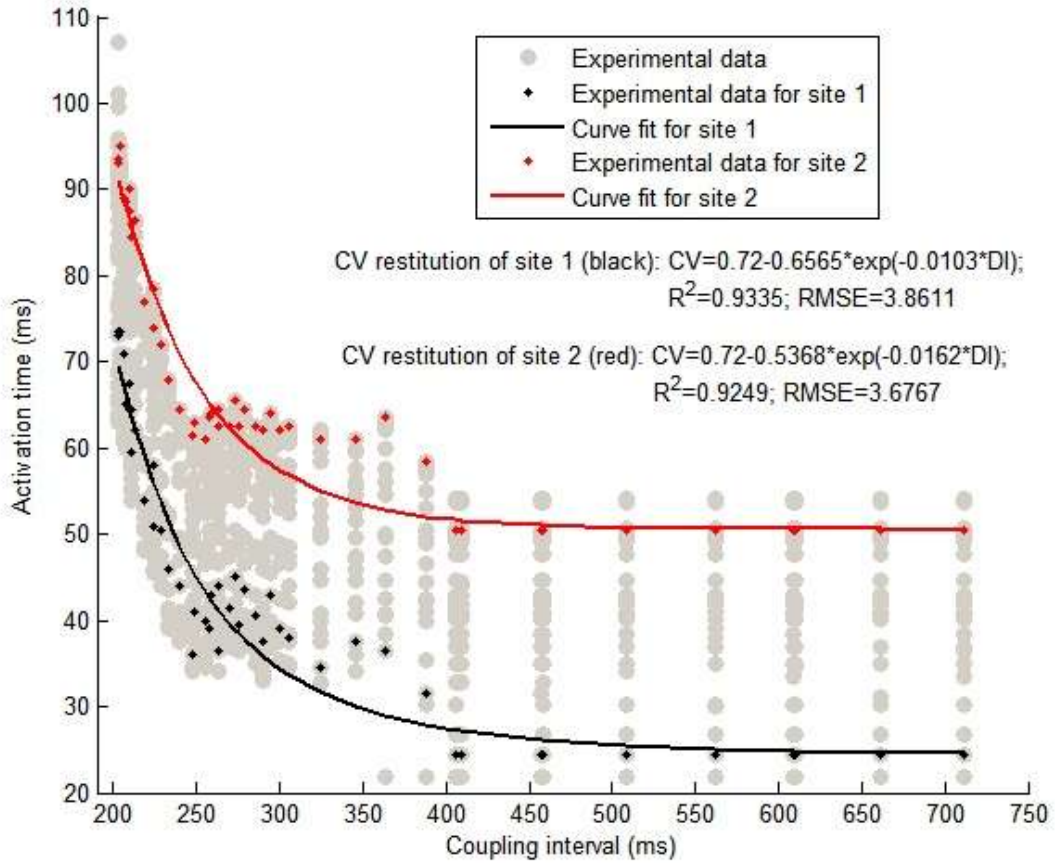

Figure 5.6: Modelling CV restitution properties. Gray points are experimental data of activation time under different coupling intervals for all investigated sites; site 1 (black) is an early activated site, while site 2 is a late activated site; R^2 and RMSE were calculated based on simulation results and experimental data of activation time.

The phenomenon discussed above results from reduction of conduction velocity due to CV restitution. Similar to APD restitution properties, heterogeneity of CV restitution property also plays an important role in determining stability of ventricular tissue. A direct result from heterogeneity of CV restitution is dispersion of activation time. However, the influence of CV restitution properties on dispersion of activation time is not as simple as increase in activation time under short coupling interval. Variation of activation time dispersion between steady-state beat and premature beat depends on distribution of CV restitution properties: e.g. for patient 1 listed in table 5.2, dispersion of activation time for premature beat is larger than

the one for steady-state beat; in the example shown in figure 5.6, dispersion of activation time for premature beat between site 1 and site 2 is smaller than the one for steady-state beat (21.463ms under the minimum coupling interval compared with 25.961ms under the steady-state coupling interval).

5.4 Validation of the restitution models on extra-stimuli

In section 5.2 and 5.3, the results of APD restitution modelling and CV restitution modelling were presented, demonstrating that restitution properties can be obtained by fitting the restitution models with experimental data for premature beat (under S_1-S_2 stimulation protocol). Based on the restitution properties, simulation studies can be carried out for the purpose of analyzing the influence of restitution properties on initiation of wave-break and re-entry. As discussed in section 4.4, condition for functional block can be quantified using the modelled restitution properties. This condition for functional block is under the precondition that activation and repolarisation of extra-stimulation (S_3) can be simulated using restitution models. Consequently, before the condition for functional block was investigated, validation of restitution models on extra-stimuli was presented in this chapter.

Validation of restitution models on extra-stimuli was achieved by two approaches: simulation result of activation time for extra-stimuli was compared with experimental data acquired from electrogram analysis on patients undergoing extra-stimulation (S_1-S_2-S_3) studies, which proved that the CV restitution model can well predict the activation conduction for extra-stimuli; the other approach was based on simulation studies using ion channel model to show that APD restitution model also applies on extra-stimuli. The reason for using simulation studies of ion channel model is that T waves for identifying repolarisation time of S_3 in most electrograms obtained from extra-stimulation experiments were not clear enough to analyse.

5.4.1 CV restitution model

Similar to the modelling process presented in section 5.2, DI at the stimulation site was defined based on equation 5.1 for simulation of activation conduction time for S_3. Here, the minimum coupling interval was the minimum coupling interval applied for S_3. DI along the conduction pathway can be defined based on equation 4.15 and 4.27:

$$DI_{S3}(x_i) = DI_{S3}(x_{i-1}) + \frac{\Delta x}{CV_{S3}(x_{i-1})} - (RT_{S2}(x_i) - RT_{S2}(x_{i-1})) \tag{5.3}$$

Equation 5.3 and 5.2 are the same from their physical meaning, the only difference is the repolarisation time variance in equation 5.2 can be replaced with $\frac{\Delta x}{CV_{SS}}$ because its previous beat is a steady-state beat, while in equation 5.3 this time variance is a result of combined effects of APD restitution and CV restitution ($RT_{S2}(x_i) - RT_{S2}(x_{i-1}) = \frac{\Delta x}{CV_{S2}(x_{i-1})} + APD_{S2}(x_i) - APD_{S2}(x_{i-1})$).

Based on electrogram analysis of patients undergoing extra-stimuli experiment, activation times for extra premature beats were obtained. As discussed before, the activation time depends on CV restitution along the conduction pathway from the stimulation site to the investigated site. Therefore, by comparing these experimental data of activation times with simulation results of activation times for the extra premature beat using CV restitution properties (acquired based on experimental data of the first premature beat), it was proved that CV restitution properties obtained from experimental data of the first premature beat can well be used on predicting activation time for extra premature beat. The results of comparison were presented in table 5.3, and the comparisons of simulated activation time and experimental data were shown in figure 5.7.

Patient ID		a	b	c	d	e	f
R^2	Max	0.965	0.978	0.924	0.874	0.923	0.916
	Min	0.700	0.756	0.806	0.724	0.729	0.724
	Mean	0.847	0.852	0.859	0.795	0.832	0.825
	SD	0.083	0.077	0.050	0.075	0.083	0.068
RMSE	Max	36.489	14.504	11.115	16.375	14.858	22.643
	Min	4.366	2.670	2.845	4.407	4.300	7.987
	Mean	12.476	7.221	7.421	8.289	7.931	14.824
	SD	8.248	3.330	3.134	4.201	4.268	4.004

Table 5.3: Comparison of simulated activation time for extra-stimuli S_3 and experimental data. R^2 and RMSE were calculated for each investigated site demonstrating the variance between simulation results and experimental data; patient a and patient b are the same with patient 5 and patient 6 in table 5.1 and 5.2.

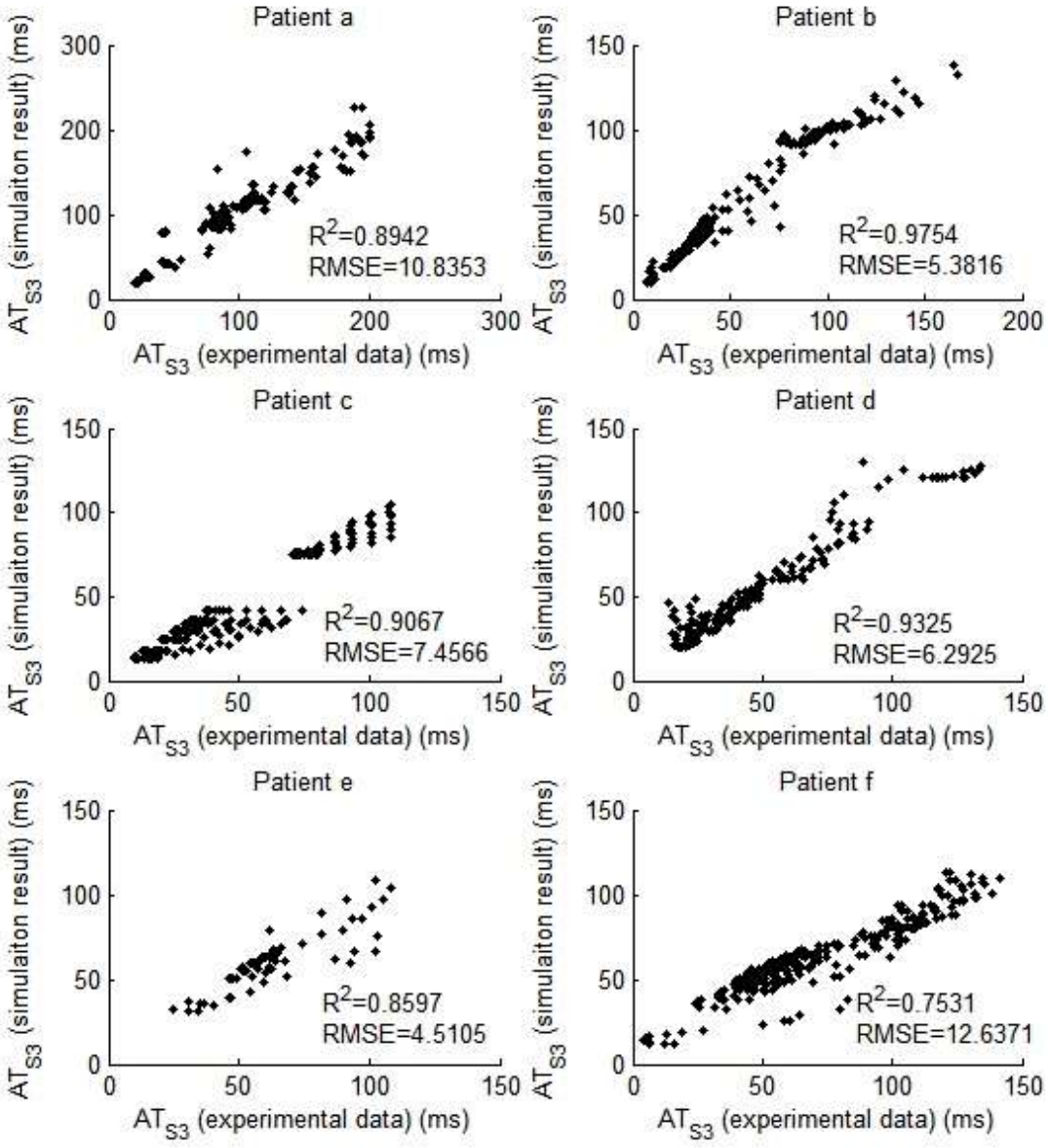

Figure 5.7: Comparison of simulation result of activation time for extra-stimuli S_3 and experimental data. R^2 and RMSE in the figure were calculated by comparing simulated activation time with experimental data for all the investigated sites.

5.4.2 APD restitution model

In the simulation studies based on ion channel models, the steady-state coupling interval was defined to be 600ms. Similar to the S_1-S_2-S_3 experimental arrangement, three steady-state beats (S_1) were introduced before the first premature beat (S_2) was initiated. The coupling intervals of S_2 were defined to be 240ms, 300ms, 400ms, and 600ms. Under each coupling interval of S_2, coupling interval of extra-stimuli (S_3) was decreased from 600ms to the minimum coupling interval close to the refractory period of S_2 (as shown in figure 5.8). Consequently, following each premature beat S_2, APD restitution data were obtained for the extra-stimuli S_3.

APD restitution model was obtained by fitting the model with APD restitution properties under S_2, after which APDs calculated from APD restitution models were compared with those simulated data under S_3, demonstrating that APD restitution model can well predict refractory periods under S_3 (Although, there were some variances between S2 restitution data and S3 restitution data as shown in figure 5.9, these variances did not have much influence on prediction of APD for S_3 using APD restitution model: R^2=0.9719, RMSE=1.5366 for CI_{S2}=400ms; R^2=0.9611, RMSE=1.5983 for CI_{S2}=300ms; R^2=0.9638, RMSE=1.4854 for CI_{S2}=240ms as shown in figure 5.9).

Therefore, the processes of validating the restitution models on extra-stimuli indicated that restitution models build on experimental data of S2 can well predict the conduction of activation and repolarisation of sequential premature beats. This validation provided the fundamental basis for analysis of functional block using simulation studies based on restitution models.

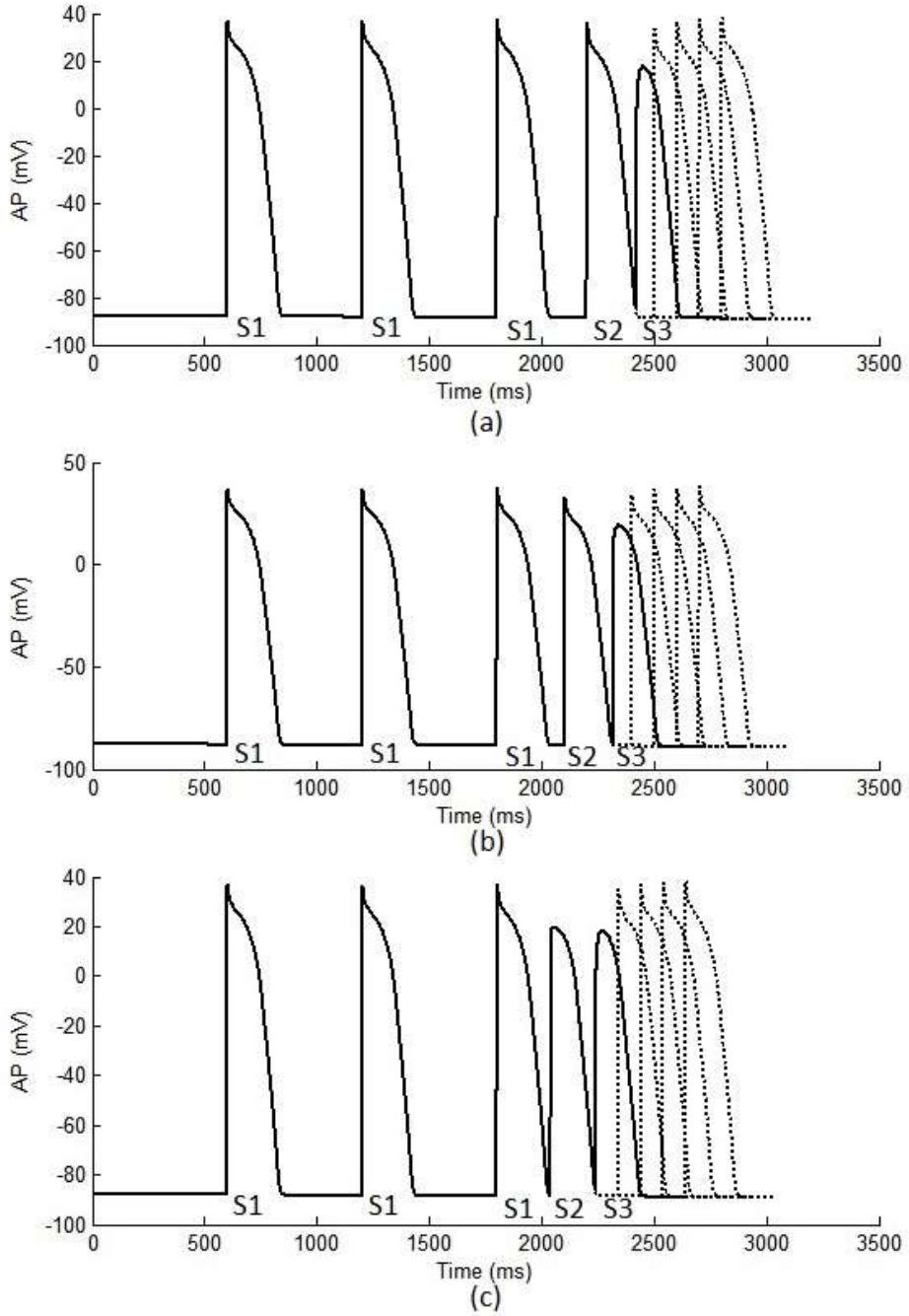

Figure 5.8: S_1-S_2-S_3 simulation studies based on ionic model. The dashed lines indicate simulations under different coupling intervals of S_3; (a): coupling interval (S_2)=400ms, for S_3, from left to right coupling intervals are 220ms, 300ms, 400ms, 500ms, and 600ms; (b): coupling interval (S_2)=300ms, for S_3, from left to right coupling intervals are 220ms, 300ms, 400ms, 500ms, and 600ms; (c): coupling interval (S_2)=240ms, for S_3, from left to right coupling intervals are 200ms, 300ms, 400ms, 500ms, and 600ms.

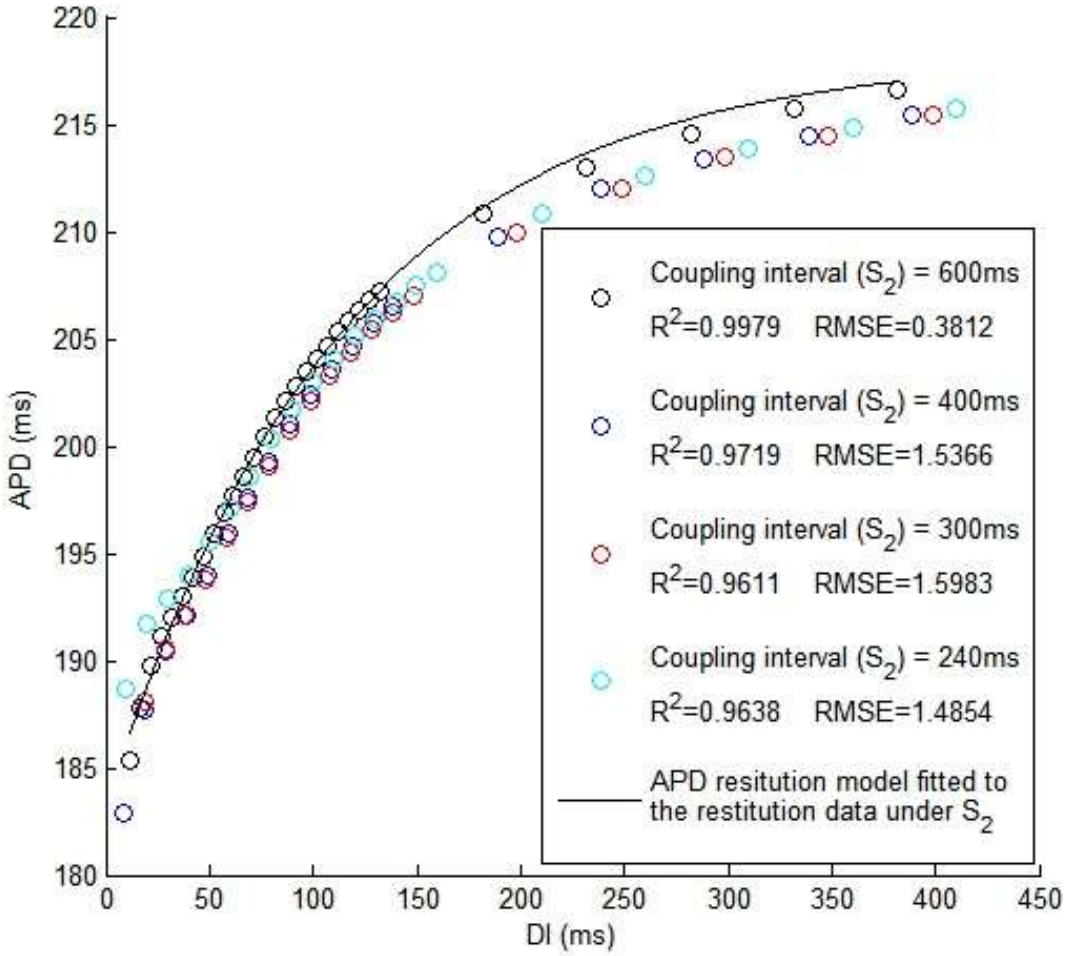

Figure 5.9: APD restitution data for extra-stimuli under different coupling intervals of S_2. APD restitution model were fitted with single premature stimuli (S_1-S_2) restitution data; for each group of data for extra-stimuli, R^2 and RMSE were calculated by comparing calculated APD from APD restitution model and ion channel model simulation results.

5.5 Discussion

As discussed in section 2.3, restitution hypothesis indicated that APD restitution with its slope larger than 1 can lead to wave-break and re-entry. According to the modelling results shown in section 5.2, all patients have regions of steep APD restitution curve (slope of APD restitution curve larger than 1): e.g. in patient 1 listed in table 5.1, 40.86% of all investigated sites (38 out

of 93 sites) have APD restitution with its slope larger than 1; in patient 2, 22.58% of all investigated sites have steep APD restitution (21 out of 93 sites). Obviously, patient 1 has larger percentage of steep APD restitution area than patient 2, which corresponds to what has been shown in figure 5.1 (c) and (d).

According to restitution hypothesis, there is another property that is highly related with wave-break and re-entry, which is heterogeneity of restitution properties. In section 5.2, it has been shown that R^2 and RMSE of linear regression for APDs and DIs under the smallest coupling interval can be used to evaluate the heterogeneity of APD caused by APD restitution. The calculated results indicated that patient 1 has smaller R^2 than patient 2 (0.0297 for patient 1 compared with 0.0668 for patient 2), which means heterogeneity of APD restitution properties in patient 1 is larger than in patient 2. Consequently, based on APD restitution hypothesis, it can be concluded that it is more likely to get wave-break and re-entry in patient 1 than in patient 2.

For CV restitution, its effect on initiation of wave-break and re-entry is accomplished through reduction of conduction velocity, which results in variance in DIs along the conduction pathway. Changes in DIs then influence repolarisation time depending on APD restitution properties. As shown in table 5.2, activation times for steady-state beat and premature beat indicated the slowing down effect of CV restitution. Comparison of dispersions of activation times for steady-state beat and premature beat showed that CV restitution leaded to larger dispersion of activation time in some patients (e.g. patient 1: 33.466ms for S_1 compared with 5.1667ms for S_2), while it can also result in smaller dispersion of activation time (e.g. patient 6: 118.987ms for S_1 compared with 112.000ms for S_2). As discussed in section 5.3, these effects depend on distribution of CV restitution properties across the investigated area.

5.6 Conclusion

In this chapter, the modelling results of APD restitution and CV restitution were presented, based on which some simple analysis can be made referring to restitution hypothesis. However, these analyses were not enough to demonstrate the effects of restitution properties on initiation of wave-break and re-entry. It has been discussed that occurrence of wave-break and re-entry is a result of complex interactions between CV restitution and APD restitution (activation and repolarisation). Validation of restitution model on extra-stimuli showed that activation and repolarisation of sequential premature beats can be predicted by simulation based on restitution models. Based on the validation, analyses were made by simulating functional block using the restitution data obtained from patient-specific experimental data, and condition for functional block as presented in section 4.4 was calculated to show the effect of restitution properties on initiation of functional block.

6 Simulation studies and results

6.1 Introduction

In the previous chapter, the restitution modelling results based on experimental data were presented. Analysis for initiation of wave-break and re-entry can be made referring to the restitution hypotheses. However, analyzing restitution properties (steepness of APD restitution curve, heterogeneity of APD restitution and CV restitution properties) is not clear enough to explain the relationship between restitution properties and initiation of wave-break and re-entry. In this chapter, simulation studies were carried out aiming to demonstrate the influence of restitution properties on unstable behaviour of cardiac tissue (functional block) using one-dimensional conduction model and restitution properties obtained from patient-specific experimental data.

The simulation studies included two parts. The first one is to use simulation to study the interactions of APD and CV restitution properties. One-dimensional conduction model combined with restitution properties obtained from patient-specific data was used to simulated occurrence of functional bock under specific coupling intervals aiming to explain how restitution properties are related with initiation of functional block. The second one is application of the condition for functional block as presented in section 4.4 based on patient-specific restitution properties. Comparisons were made between two example patients using three-dimensional visualisation technique.

At the end of this chapter, attempt was made to fit the ORd ion channel model with APD restitution data obtained from patient experiment. This simulation studies provided a possible method for deriving ventricular cellular electrophysiological properties based on

patient-specific data, which has the potential of simulating activation conduction across the surface of the ventricle and occurrence of wave-break and re-entry.

6.2 Interactions of APD and CV restitution properties

Two sites (site 1 and site 3) with different restitution properties (as shown in figure 6.1) were chosen from patient 2 as listed in table 5.1 and 5.2 to carry out one-dimensional conduction simulation studies. For each site, DIs for two continuous premature beats at the stimulation site were defined to be the same aiming to provide the same initial conditions for two simulations ($DI_{S2}(x_0) = 2ms, DI_{S3}(x_0) = 20ms$).

The simulation results were shown in figure 5.2, in which functional block was initiated in the conduction pathway of site 1, and no functional block occurred in the conduction pathway of site 3. Referring to their restitution properties, site 1 has steeper APD restitution and CV restitution than site 3. This means under the same amount of reduction in DI, change in APD is larger in site 1 than in site 3; also, change in CV is greater in conduction pathway of site 1 than in the one of site 3. The combined effect of APD restitution and CV restitution properties is that dispersion of repolarisation of S_2 is much larger in the conduction pathway of site 1 than in the one of site 3, which leads to more likelihood of functional block initiation. The simulation studies and discussion made above demonstrated that interaction of APD restitution and CV restitution properties plays an important role in initiation of functional block that is the key mechanism for wave-break and re-entry.

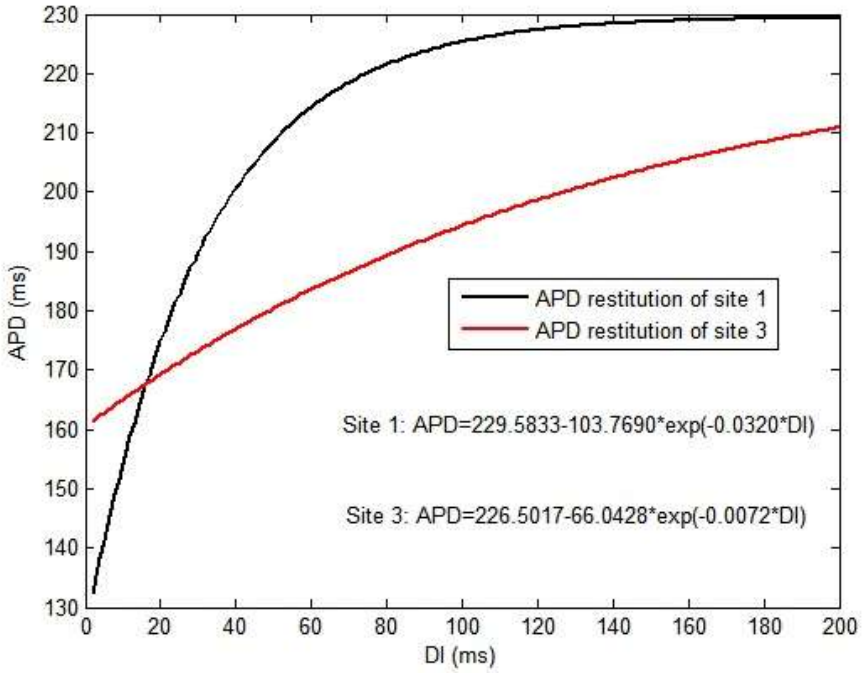

(a)

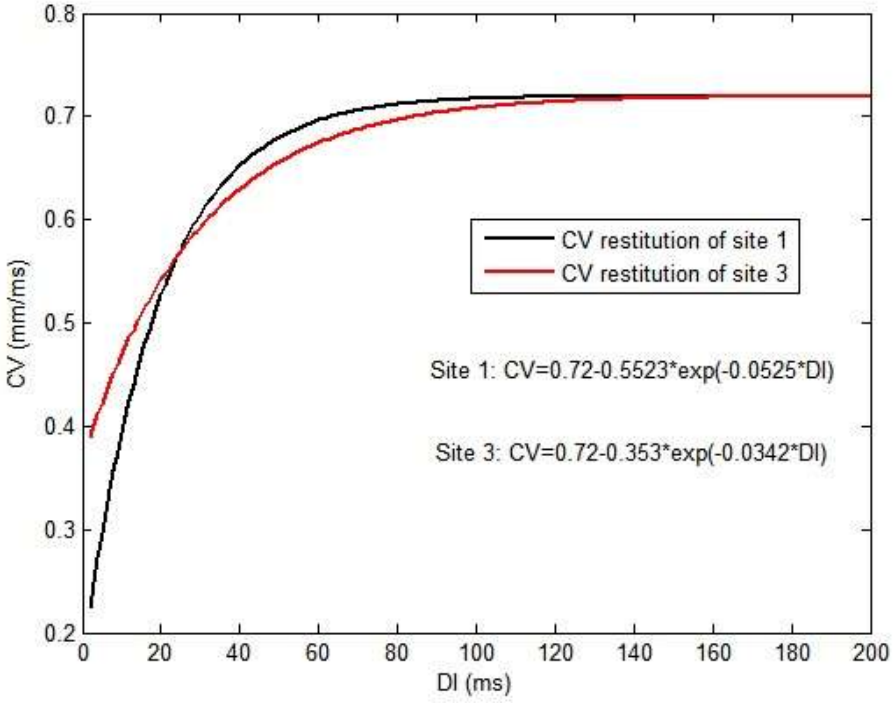

(b)

Figure 6.1: APD restitution curves and CV restitution curve for two sites (site 1 and site 3) from patient 2 as listed in table 5.1 and 5.2.

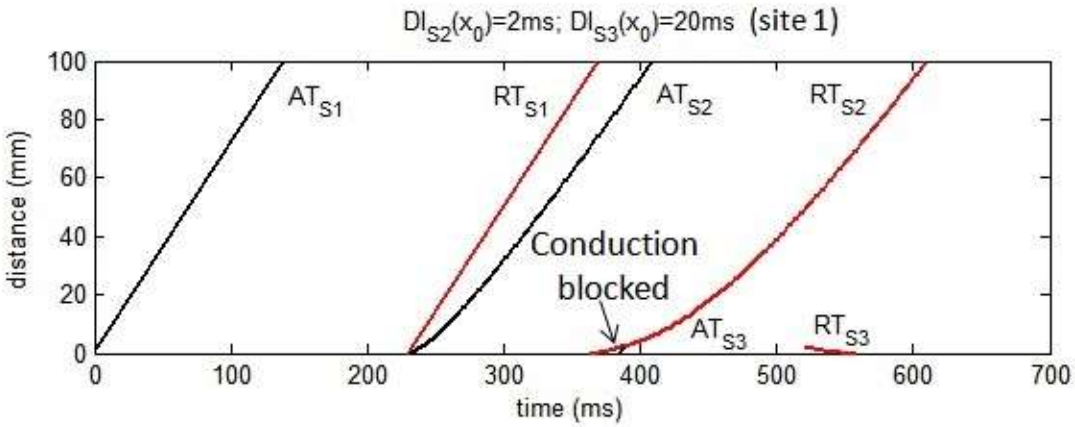

(a)

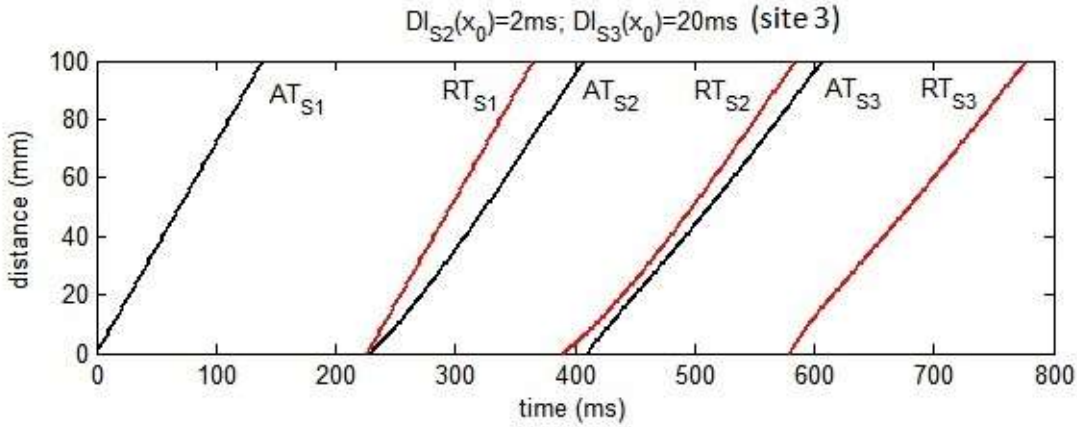

Figure 6.2: Simulation of functional block for two sites (site 1 and site 3) from patient 2. AT indicates activation time (black lines), while RT indicates repolarisation time (red lines); DI_{S2} at the stimulation site ($DI_{S2}(x_0)$) is defined to be 2ms, while DI_{S3} at the stimulation site ($DI_{S3}(x_0)$) is set to be 20ms for both simulations.

As discussed in section 5.3, heterogeneity of restitution properties also has great influence on occurrence of functional block. To demonstrate this effect, repolarisation time that is the combined effect of APD and CV restitution were investigated. It has been shown in section 5.3 that as coupling interval shortened, activation time from the stimulation site to the investigated site increased. Also, increase of activation time varied depending on distribution of CV restitution properties across the surface of the ventricle. An example of simulated

activation times was shown in figure 6.3 and 6.4. Three sites were chosen to show the effect of different CV restitution properties. As shown in figure 6.3, the variance between activation times of site 79 and 49 shortened as coupling interval was decreased (45.6441ms under CI_{S2}=381ms compared with 30.3617ms under CI_{S2}=234ms), while the absolute value of the variance between activation times of site 50 and 49 was decreased to 0 and then increased (5.6458ms under CI_{S2}=381ms, 0.1046ms under CI_{S2}=280ms, and 16.9644ms under CI_{S2}=234ms). Changes in variation of activation times between sites indicated that the pattern of activation conduction changed as coupling interval shortened: site 49 was activated earlier than site 50 under long coupling intervals; under short coupling interval, site 49 was activated later than site 50 (as shown in figure 6.4).

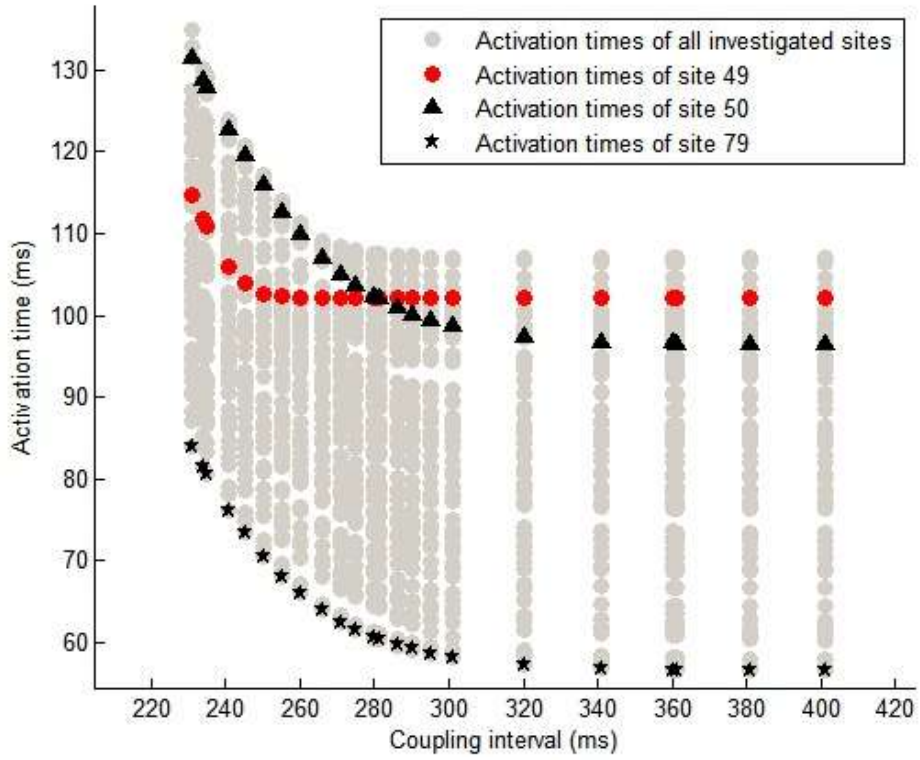

Figure 6.3: Changes in activation times due to heterogeneity of CV restitution properties. Activation times presented in the figure are simulated activation times of patient 2 as listed in table 5.1; gray points indicate activation times for all investigated sites; three sites (site 49, site 50, and site 79) were chosen to show the changes in activation times as coupling interval shortened.

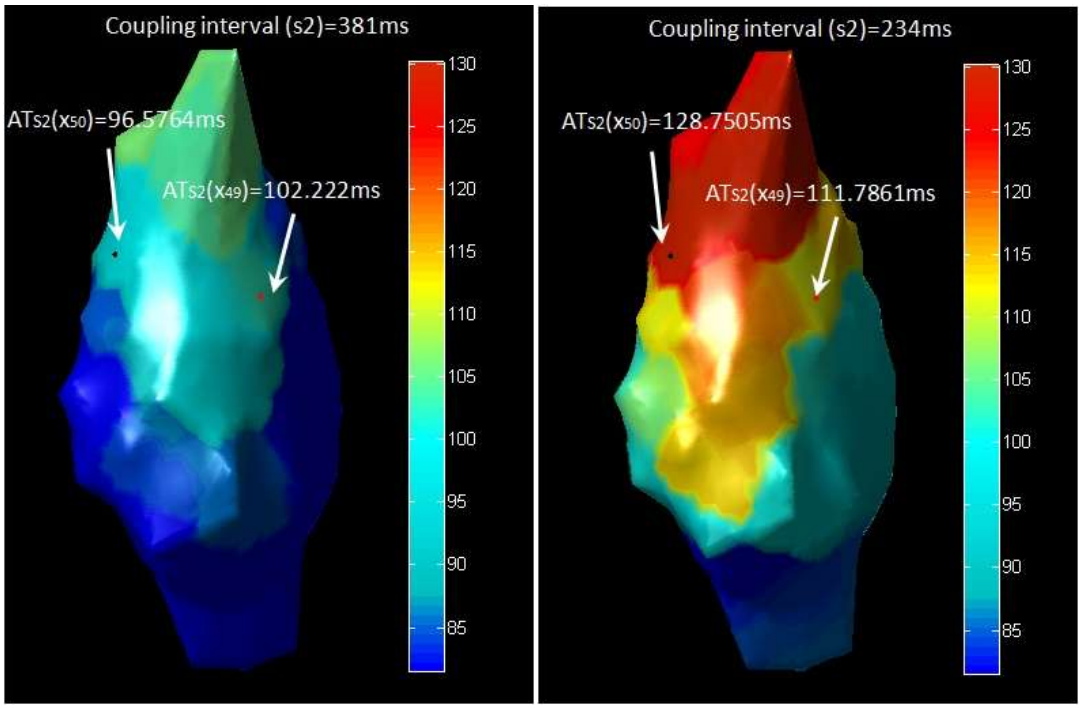

Figure 6.4: Three-dimensional visualisation of activation conductions across the ventricular surface under two different coupling intervals. Site 50 (black point) was activated earlier than site 49 (red point) under CI_{S2}=381ms (96.6ms for site 50 compared with 102.2ms for site 49); a reverse relationship existed between the activation times of the two sites under CI_{S2}=234ms (128.8ms for site 50 compared with 111.8ms for site 49).

These changes in activation conduction patterns result from different CV restitution properties. As coupling interval shortened, reduction of CV along the conduction pathway of site 49 is smaller than the one of site 50. This means conduction block might be initiated along the conduction pathway of site 50 if another premature beat is introduced, while no functional block occurs along the conduction pathway of site 49, in which case re-entry might be triggered. As discussed previously, reduction of CV leads to variations in DIs along the conduction pathway that consequently produce increased dispersion of repolarisation time with different extents depending on the APD restitution properties. Dispersions of repolarisation time under different coupling intervals were shown in figure 6.5.

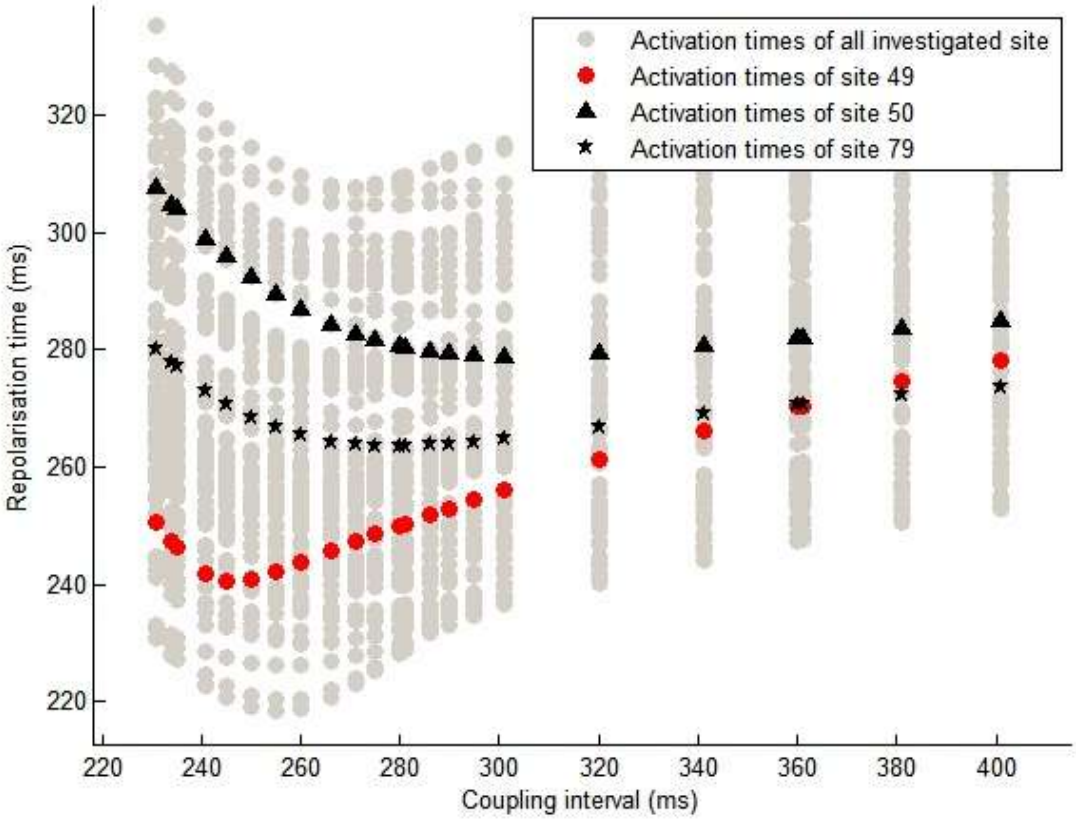

Figure 6.5: Dispersions of repolarisation times under different coupling intervals. Three different sites were chosen from patient 2 (same with sites shown in figure 6.3); time 0 is set to be the instant of stimulation for S_2; repolarisation time is calculated by adding the simulated activation time with APD calculated based on modelled APD restitution properties (DI is calculated using equation 4.25).

Figure 6.5 showed that interactions of APD restitution and CV restitution properties produced changes in dispersion of repolarisation times: as the coupling interval shortened, the sequence of repolarisation for three sites changes (272.4ms for site 79, 274.5ms for site 49, and 283.6ms for site 50 under CI_{S2}=381ms; 247.4ms for site 49, 277.9ms for site 79, and 304.9ms for site 50 under CI_{S2}=234ms). These analysis indicated that regions around site 49 were activated relatively late under long coupling intervals (compared with region around site 50 and 79). However, as the coupling interval decreased, this region became early repolarised area, which means it is quite possible that extra premature beat can be conducted through the conduction

pathway of site 49 while other regions are still in their refractory periods. In this case, re-entry might be initiated. Therefore, dispersion of repolarisation time cannot fully explain the effect of heterogeneity of restitution properties; it is change in pattern of activation time and repolarisation time that is more important in determining occurrence of re-entry.

6.3 Condition for functional block

In section 4.4, condition for functional block was discussed by presenting a function and a biomarker (DI_{bound}) to quantify the likelihood of functional block occurrence. The function for condition of functional block indicated that interaction of APD and CV restitution properties plays an important role in initiation of functional block. In this section, the biomarker (DI_{bound}) was calculated for all the investigated patients based on their restitution properties modelled from experimental data. Detailed results of all patients were presented in appendix. Table 6.1 showed examples of DI_{bound} calculated for the 6 patients listed in table 5.1. In the process of modelling CV restitution properties (as presented in section 5.3), the minimum DI is defined to be 2ms. Therefore, DI_{bound}=2ms indicates it is impossible to initiate functional block along the conduction pathway with two continuous premature beats (S_2 and S_3).

According to the results shown in table 6.1, comparison of different patients can be made on possibility of functional block initiation. E.g. DI_{bound} calculated in patient 1 is smaller than in patient 2 (averaged value of DI_{bound} is 2.31ms compared with 6.03 in patient 2). Also, three-dimensional visualisation of DI_{bound} on the patients (as shown in figure 6.6) indicated that patient 2 had larger areas with relatively bigger DI_{bound} compared with patient 1, which means that it is more likely to initiate functional block in patient 2 than in patient 1. This is opposite to the analyses made based on restitution hypothesis as discussed in section 5.2 and 5.3 (larger

area of steeper APD restitution curves in patient 1 than in patient 2; larger variances of APD restitution properties and activation time in patient 1 than in patient 2).

Patient ID		1	2	3	4	5	6
DI_{bound} (ms)	Max	4.5	20.9	3.4	11.3	5.2	33.7
	Min	2.0	2.0	2.0	2.0	2.0	2.0
	Mean	2.3	5.2	2.4	3.1	2.3	8.3
	SD	0.5	3.9	0.4	2.8	0.7	10.6

Table 6.1: DI_{bound} calculated for condition of functional block for six example patients. Patients are the same as listed in table 5.1.

In section 6.2, two example sites (site 1 and site 3) were chosen from patient 2 to show the effect of interaction of restitution properties on initiation of functional block. Based on their restitution properties (as shown in table 6.2), DI_{bound} was calculated (as shown in figure 6.7). In section 6.2, it was shown that under the same initial conditions (same DIs at the stimulation site) functional block was initiated along the conduction pathway of site 1, while no functional block occurred along the conduction pathway of site 3. The calculated results for DI_{bound} indicated that it is easier to initiate functional block along the conduction pathway of site 1 than the one of site 3 (DI_{bound}=12.08ms for site 1 compared with DI_{bound}=8.36ms for site 3).

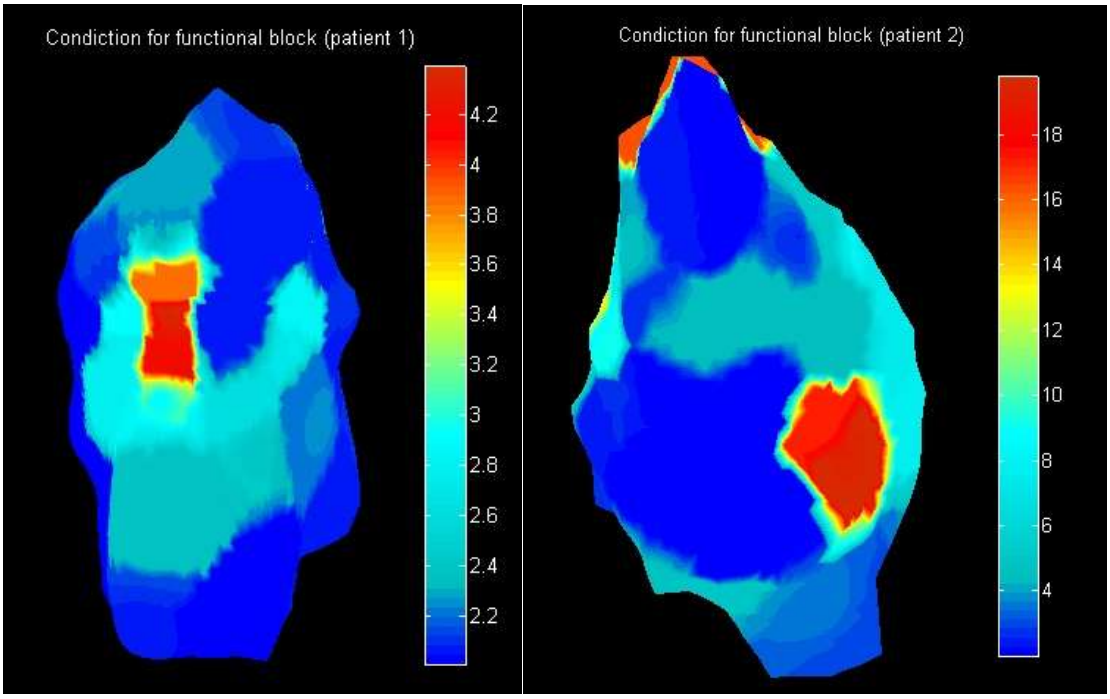

Figure 6.6: Three-dimensional visualisation of DI_{bound} for condition of functional block in two example patients.

Consequently, simulation studies presented in this section proved that APD/CV restitution hypothesis is not enough for analyzing the mechanism of functional block. Analyses made based on restitution hypothesis indicated that patient 1 is more risky than patient 2; while simulation studies of interactions of restitution properties produced an opposite conclusion. Restitution hypothesis is only true under the same conditions of other parameters (e.g. APD restitution hypothesis can well be used to analyse initiation of functional block under the assumption of same CV restitution properties). It is the interaction of APD and CV restitution properties that is the key determinant in initiating functional block. According to equation 4.31, parameters determining occurrence of functional block include: steepness of APD restitution curve, conduction velocity at given DI, minimum conduction velocity, and steady-state conduction velocity. Here, the influence of steady-state conduction velocity was not included in this project (CV_{SS} is defined to be 0.72mm/ms).

		Site 1	Site 3
APD restitution properties	B_{APD}	103.7690	66.0428
	C_{APD}	-0.0320	-0.0072
	Slope	2.411	0.442
CV restitution properties	B_{CV}	0.5523	0.3530
	C_{CV}	-0.0525	-0.0342
	CV_{min} (mm/ms)	0.223	0.390
DI_{bound} (ms)		12.08	8.36

Table 6.2: Restitution properties and DI_{bound} for condition of functional block for two sites (site 1 and site 3) in patient 2. Slopes of APD restitution curves were calculated at DI=10ms; minimum conduction velocity (CV_{min}) was calculated at DI=2ms.

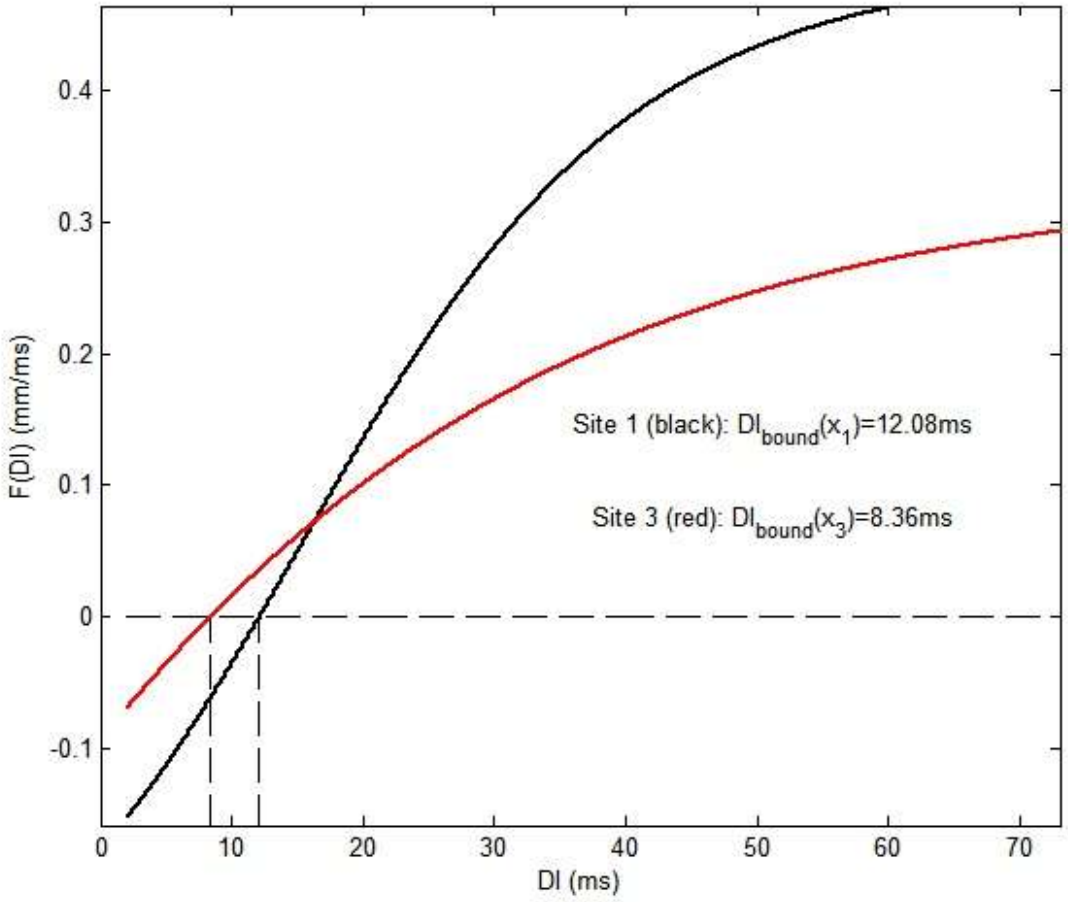

Figure 6.7: Function for condition of functional block and DI_{bound} calculated based on restitution properties from two example sites of patient 2.

6.4 Application of the simulation techniques on pharmaceutical testing

Based on the modelling techniques (APD restitution model, CV restitution model, one-dimensional conduction model, and function for condition of functional block) as discussed before, experimental data from 6 patients were analysed. Experimental data were obtained for each patient under two experimental arrangements (with or without taking ajmaline). The processes of restitution modelling and simulation studies were successfully carried out on 2 patients; unsuccessfully modelling on other patients was mostly due to poor quality of experimental data (electrogram).

Table 6.3 showed the experimental data (steady-state APD (APD_{SS}), and steady-state activation time (AT_{SS})) obtained from electrogram analysis. Comparisons made between these two properties indicated that ajmaline caused reduction in the steady-state APD (APD_{SS}) and increase in the steady-state activation time. According to the function for condition of functional block (equation 4.31), CV_{SS} is one of the parameters that determines occurrence of functional block. Increase in the steady-state activation time as observed in table 6.3 demonstrated that ajmaline resulted in reduction of CV_{SS} (as shown in table 6.4). Referring to equation 4.31, reduction of CV_{SS} leads to more possibility for initiation of functional block.

		Patient I		Patient II	
		Normal	Ajmaline	Normal	Ajmaline
number of electrodes		27		28	
APD_{SS}	Max	294.6	222.9	212.6	208.0
	Min	180.1	156.9	158.0	152.0
	Mean	202.2	180.0	178.4	176.6
	SD	22.1	15.7	11.4	14.9
AT_{SS}	Max	137.6	180.6	136.7	168.8
	Min	12.1	21.8	15.3	17.6
	Mean	82.3	110.1	91.0	112.6
	SD	40.9	48.3	36.0	44.9

Table 6.3: Steady-state APD (APD_{SS}) and steady-state activation time (AT_{SS}) under two experimental arrangements (with and without taking ajmaline)

		Patient I		Patient II	
		Normal	Ajmaline	Normal	Ajmaline
Slope of APD restitution curve (calculated at DI=10ms)	Max	10.427	38.677	743.915	1288.615
	Min	0.344	0.572	0.624	0.661
	Mean	4.318	12.446	101.919	106.199
	SD	2.549	17.651	192.001	328.488
R^2 (APD)	Max	0.958	0.939	0.954	0.878
	Min	0.820	0.712	0.723	0.720
	Mean	0.915	0.797	0.858	0.786
	SD	0.039	0.085	0.081	0.047
RMSE (APD)	Max	10.705	8.546	11.924	12.618
	Min	3.048	3.183	3.037	5.344
	Mean	5.581	6.556	6.775	7.834
	SD	2.073	2.267	3.047	1.706
CV_{SS} (mm/ms)		0.720	0.538	0.720	0.582
CV_{min} (mm/ms)	Max	0.010	0.490	0.164	0.432
	Min	0.002	0.005	0.003	0.003
	Mean	0.003	0.088	0.010	0.111
	SD	0.001	0.165	0.030	0.172
R^2 (CV)	Max	0.918	0.914	0.937	0.958
	Min	0.764	0.727	0.727	0.730
	Mean	0.853	0.796	0.850	0.836
	SD	0.047	0.049	0.068	0.072
RMSE (CV)	Max	8.662	4.110	6.743	9.217
	Min	6.331	1.404	3.444	1.054
	Mean	7.464	2.526	4.944	4.314
	SD	0.850	0.816	0.733	1.619

Table 6.4: Restitution properties modeled based on experimental data. Coefficient of determination (R^2) and root mean squared error (RMSE) were calculated to evaluate how well the restitution models fit with experimental data.

Assuming the conduction pathway from the stimulation site to the investigated site remains the same under two situations (the length of the conduction pathway is constant), the conduction velocity under the situation of taking ajmaline can be calculated as:

$$CV_{SSajmaline} = CV_{SS} \cdot AT_{SS} / AT_{SSajmaline} \quad (6.1)$$

Here, AT_{SS} and $AT_{SSajmaline}$ were the averaged activation times for the purpose of reducing influence from errors rising from experimental data.

As presented before, DI_{bound} can be calculated (as shown in table 6.5) using the restitution properties constructed from experimental data. The results showed that ajmaline leaded to an increase in DI_{bound}, which means it increased the possibility of initiating functional block. Notably, this increase in the possibility of initiating functional block does not mean increase in the risk of re-entry occurrence. It could also terminate propagation of re-entry. Due to the limitation of one-dimensional conduction model, this effect could not be further studied.

		Patient I		Patient II	
		Normal	Ajmaline	Normal	Ajmaline
DI_{bound} (ms)	Max	3.06	6.09	18.67	39.29
	Min	2	2	2	2
	Mean	2.4231	2.3617	5.6323	11.29833
	SD	0.3751	1.1334	4.8723	13.95607

Table 6.5: DI_{bound} for condition of functional block calculated based on modeled restitution properties under the two experimental arrangement (with and without taking ajmaline). DI_{bound}=2ms indicated that functional block cannot be initiated.

In this section the application of the simulation techniques using restitution models on examining effect of ajmaline was presented. Although it was concluded that ajmaline could possibly lead to more possibility of functional block initiation according to the results from two patients, it still needs large body of experimental data to demonstrate the effect of ajmaline.

6.5 Fitting ionic model with APD restitution data

In section 4.2, discussions have been made on the relationship between $f_{Ca,slow}$ (slow development of Ca^{2+} dependent inactivation gate for Ca^{2+} current through the L-type Ca^{2+} channel (I_{CaL})) and APD. Studies presented in section 4.5 showed that the intracellular ion concentrations only have limited effect on steepness of APD restitution. Under the consideration of the amount of calculations, three key parameters (C_4, C_5, and C_6 in equation 4.3 and 4.4) were selected to act as dependent variables for fitting the ion channel model with experimental data. Simulations were carried out with the same input of coupling intervals (S_1 and S_2) from experimental data.

APDs obtained from simulations were then compared with experimental data. The three variables were acquired using the method of least squares. The result of model fitting was shown in figure 6.8 (R^2=0.9186, RMSE=6.2709). The exponential model fitted to the experimental data was also presented in figure 6.8 (R^2=0.9251, RMSE=6.0144). Notably, R^2 for exponential model fitting is slightly higher than for ion channel model fitting. However, simulation results of ion channel model can describe the effect of increase in APD under coupling interval larger than steady-state coupling interval (CI_{SS}=600ms), which cannot be described by exponential model. Also, the process of model fitting presented in this section was carried out by adjusting three variables. Other parameters in the ion channel model can also be used as variables for model fitting, e.g. G_{to} (conductance of transient outward current (I_{to})) can also lead to change in APD

as shown in appendix (table A.1.3) (G_{to}=0.02nS/pF in ORd model (O'Hara et al., 2011), and G_{to}=0.073nS/pF in ten-Tusscher model (ten Tusscher et al., 2004)).

Although this technique has the potential of modelling re-entry across the inner surface of the ventricle using patient-specific data, it is too computationally expensive (it took more than 3 days to fit the ion channel model with experimental data from single site on a PC with Intel Core2 Duo CPU at 2.5GHz).

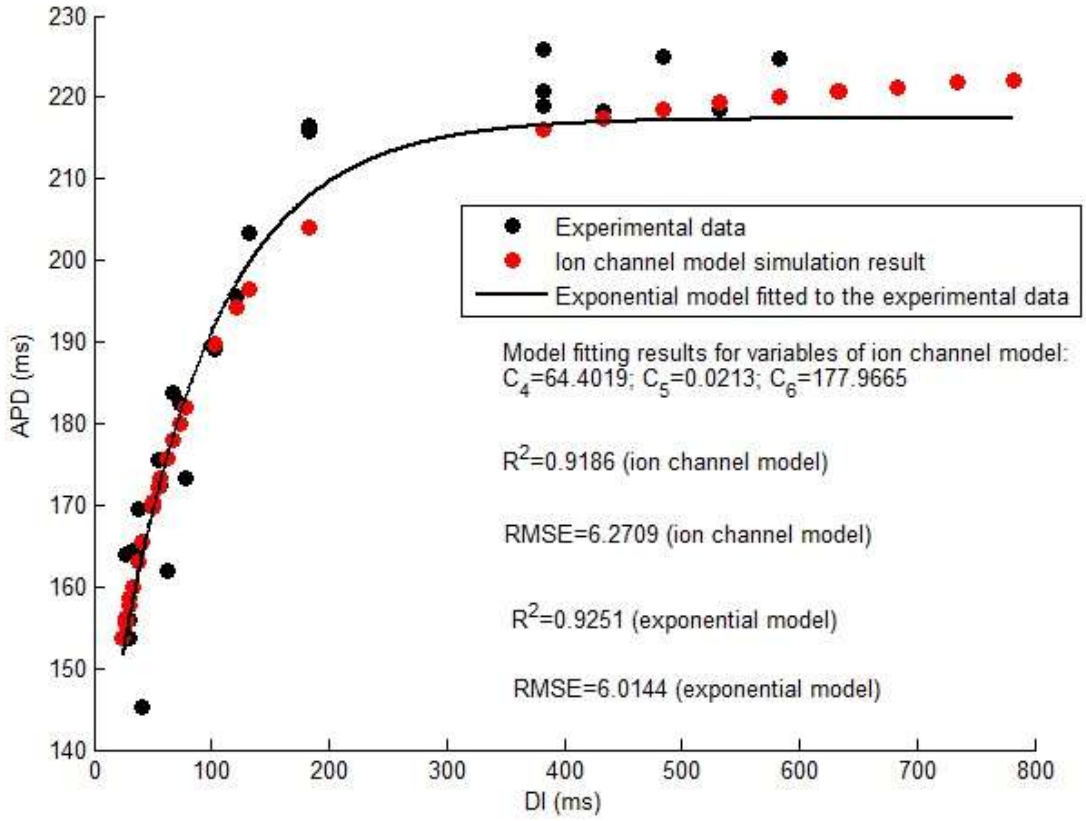

Figure 6.8: Results of fitting ion channel model with experimental data of one site (site 16) from patient 2. The exponential model fitted (as indicated by the black line) was also presented for comparison; R^2 and RMSE were calculated to quantify the quality of model fitting.

6.6 Conclusion

In this chapter, simulation studies were carried out using one-dimensional conduction model as presented in section 4.3 and restitution properties obtained from patient-specific experimental data as shown in section 5.2 and 5.3. Comparisons were made between simulation studies using different restitution properties, demonstrating interactions of APD restitution and CV restitution properties determine the occurrence of functional block that is the key mechanism for initiating wave-break and re-entry. Also, simulation studies showed distribution (heterogeneity) of APD restitution and CV restitution properties can result in change in the patterns of activation time and repolarisation time, which is potentially risky for initiation of re-entry.

It had been proved that APD restitution and CV restitution combined with one-dimensional conduction model could well predict activation conduction and repolarisation time for extra-stimuli S_3. Consequently, the function for condition of functional block as presented in section 4.4 can be used for quantifying the influence of interactions of restitution properties on functional block. DI_{bound} were calculated based on patient-specific restitution properties, based on which comparisons were made between patients and different sites. The results showed that APD restitution hypothesis and CV restitution hypothesis cannot fully explain the mechanism of wave-break and re-entry on their own. Likelihood of wave-break and re-entry occurrence can only be fully analysed by investigating the interactions of APD restitution and CV restitution properties.

7 Conclusion and future work

This work bridged the gap between theoretical models and patient-specific clinical studies by developing a simple and effective method to integrate experimental data acquired from human electrophysiological studies into patient-specific models. The presented modelling technique was founded on the work of Gilmour's group (Fox et al., 2002, Fox et al., 2003, Gilmour et al., 2007, Otani, 2007, Siso-Nadal et al., 2008). Their work provided initial validation of the application of one-dimensional conduction simulation in predicting whether large variations of long-short coupling intervals would induce VF (Gelzer et al., 2009). These models were enhanced by deriving restitution models based on ion channel model (ORd model (O'Hara et al., 2011)) and a biomarker (DI_{bound}) for quantifying risk of functional block initiation, which allowed better prediction of activation conduction wave-front and observation of the effect of interactions of restitution properties on initiation of functional block.

a) Modelling restitution properties:

The APD restitution model was deduced from ion channel model (ORd model) by investigating the relationship between APD and cellular ionic properties at the instance of stimulation for single cell. The deduced APD restitution model is similar to the ones used in previous studies (Banville and Gray, 2002, Berger, 2004, Keldermann et al., 2008, Hanson et al., 2009). Fitting this model with experimental data obtained from electrogram analysis produced APD restitution properties for each investigated site. A great number of arguments have been made on the relationship between the steepness of APD restitution curve and initiation of wave-break and re-entry (Kobayashi et al., 1992, Karma, 1994, Qu et al., 1999, Chudin et al., 1999, Garfinkel et al., 2000). Results presented in this project indicated that slopes of APD restitution curves for most patients are larger than 1 (only 2 out of 44 patients have an averaged slope of APD restitution curves smaller than 1 as shown in appendix 2-4).

Heterogeneity of APD restitution properties has been proved to be another important factor for causing instability of cardiac tissue (Sampson and Henriquez, 2001, Yuuki et al., 2004, Clayton and Taggart, 2005). This work showed that heterogeneity of APD increased as coupling interval shortened by investigating R^2 of linear regression between APD and DI under the same coupling interval for all investigated sites (section 5.2). The extent of change in heterogeneity of APD is determined by the variance in APD restitution properties for investigated sites (R^2 ranges from 0.00005 to 0.899 as shown in appendix 2-4).

CV restitution properties have been described as being important in determining initiation of VF (Cao et al., 1999, Jordan and Christini, 2004, Banville and Gray, 2002). Previous studies calculated conduction velocity by measuring the distance between investigated sites and the time it took for activation signal to travel between sites across the surface (Kleber et al., 1986, Bayly et al., 1998, Barnette et al., 2000, Mironov et al., 2008). This method may not be accurate enough considering the possibility of activation conduction through the ventricular wall (Rodriguez et al., 2006a). In this project, the exponential model used for CV restitution was taken from prior research (Banville and Gray, 2002), which was combined with one-dimensional conduction model (Fox et al., 2002) to simulate activation conduction for premature beat. Fitting the simulated activation time with experimental data generated CV restitution properties for investigated site. Investigation of experimental data of activation time and simulation results indicated that conduction latency increased as coupling interval shortened as a result of CV restitution. In some specific situation, heterogeneity of CV restitution properties could lead to change in pattern of activation conduction and repolarisation for investigated sites (figure 6.3-6.5).

b) Validation of the restitution models on extra-stimuli:

For validation of the APD restitution model, ion channel model was used to simulate extra-stimuli, based on which APD of extra-stimuli was calculated and compared with APD

calculated from APD restitution model (section 5.4.2). For validation of CV restitution model, simulation result for activation time of extra-stimuli was compared with experimental data obtained from patients undergoing extra-stimuli experiment (section 5.4.1). The results indicated that the simulation techniques based on restitution models can well predict time dynamics (activation conduction and repolarisation) for sequential premature beats, which is critical in determining susceptibility to arrhythmia (Lambiase et al., 2009, Nam et al., 2010).

c) Condition for functional block:

Based on the validation of restitution models on extra-stimuli, analysis of functional block occurrence can be made based on simulation studies. Similar works have been done by investigating the interactions between activation wave-front and repolarisation dispersion (Qu et al., 2000, Fox et al., 2002, Otani, 2007). Different from these studies, CV restitution properties were fully derived from experimental data in this project, based on which a function and a biomarker (DI_{bound}) were developed for the purpose of quantifying the likelihood of functional block initiation. Comparisons were made between different patients (table 6.1) and different sites (table 6.2), which showed that it is the interaction of APD restitution and CV restitution that determine the occurrence of functional block.

APD restitution hypothesis and CV restitution hypothesis cannot fully explain the mechanism of functional block: e.g. numbers of research have been made focusing on APD restitution slope larger than 1 (Bass, 1975, Marculs L. Koller, 1998, Qu et al., 1999, Huang et al., 2004), simulation studies presented in this project showed that this is not enough for investigating occurrence of wave-break and re-entry. To show the possible application of this biomarker (DI_{bound}), an example of application of the biomarker (DI_{bound}) on indentifying the effect of ajmaline was presented to demonstrate how this technique can be used on pharmaceutical testing (section 6.4).

d) Fitting ion channel model with patient-specific experimental data:

At the end of this thesis (section 6.5), an attempt was made on fitting the ion channel model (ORd model) with patient-specific APD restitution data. Although this modelling process was extremely time-consuming, it could provide a possible method for simulating activation conduction across the surface of the ventricle and occurrence of wave-break and re-entry based on patient-specific ionic properties.

7.1 Future work

In this thesis, it was assumed that restitution properties along the conduction pathway from the stimulation site to the investigate site were uniform. Future work for improving the numerical models can be made by defining the change in restitution properties along the conduction pathway according to its possible position across the ventricle. This will make the model closer to the realistic situation, and consequently produce more accurate simulation results and analyses of functional block. Following this direction, condition for functional block needs to be adjusted by defining the restitution properties of adjacent cells (equation 4.30 and 4.31).

All the experimental data used in this project were obtained by pacing from a fixed site. In this case, sites far away from stimulation site have little chance to reach very small DIs (bellow 10ms). Future experimental work can be made by pacing from different sites. These experimental data can be used to improve the quality of restitution modelling. Moreover, these experiments can demonstrate whether restitution properties change under the situation of stimulation signal rising from different locations.

Patient-specific models presented in this project could give valuable diagnostic information on quantifying the risk of arrhythmia in patients at risk of inherited ventricular arrhythmias, especially Brugada syndrome or arrhythmogenic right ventricular cardiomyopathy. Also, pharmaceutical testing may benefit from these techniques. Both of these applications need large body of experimental data.

Fitting the ion channel model with patient-specific experimental data needs more work and more powerful computer. At the moment, only the influence of I_{CaL} was partly included. Future work can be made by adding in other key parameters such as conductance of ion currents. Alternatively, simplified ion channel model (Cherry and Fenton, 2004) can be used for the purpose of reducing computational complexity. Also, two-dimensional conduction ionic model can also be fitted with activation conduction across small area of endocardial surface. With the fitted ionic model, formation of spiral-wave can be simulated based on patient-specific data.

7.2 Closing statement

The interactions of activation conduction and repolarisation can be described in terms of APD and CV restitution. Simulations based on clinically acquired data can be used to predict complex activation patterns following sequential extra-stimuli. Such modelling techniques provided insight of relationship between interactions of restitution properties and occurrence of functional block. It can be concluded that it is the interactions of APD and CV restitution properties that determines initiation of functional block. Restitution hypothesis cannot fully explain the mechanism of functional block. Incorporation of clinical data into predictive models allowed risk stratification for arrhythmia and pharmaceutical testing by using the biomarker (DI_{bound}) calculated based on modelled restitution properties for individual patients.

8 References

AHUJA, S. P., GUTIERREZ, M. R. & MANNING, G. W. 1968. Mode of onset of ventricular arrhythmias. *Acta Cardiol,* 23**,** 399-407.

AUSTIN, T. M., HOOKS, D. A., HUNTER, P. J., NICKERSON, D. P., PULLAN, A. J., SANDS, G. B., SMAILL, B. H. & TREW, M. L. 2006. Modeling cardiac electrical activity at the cell and tissue levels. *Interactive and Integrative Cardiology,* 1080**,** 334-347.

BAAN, J., VAN DER VELDE, E. T., DE BRUIN, H. G., SMEENK, G. J., KOOPS, J., VAN DIJK, A. D., TEMMERMAN, D., SENDEN, J. & BUIS, B. 1984. Continuous measurement of left ventricular volume in animals and humans by conductance catheter. *Circulation,* 70**,** 812-23.

BANVILLE, I. & GRAY, R. A. 2002. Effect of action potential duration and conduction velocity restitution and their spatial dispersion on alternans and the stability of arrhythmias. *J Cardiovasc Electrophysiol,* 13**,** 1141-9.

BARNETTE, A. R., BAYLY, P. V., ZHANG, S., WALCOTT, G. P., IDEKER, R. E. & SMITH, W. M. 2000. Estimation of 3-D conduction velocity vector fields from cardiac mapping data. *IEEE Trans Biomed Eng,* 47**,** 1027-35.

BASS, B. G. 1975. Restitution of the action potential in cat papillary muscle. *American Journal of Physiology,* 228**,** 1717-1724.

BAYLY, P. V., KENKNIGHT, B. H., ROGERS, J. M., HILLSLEY, R. E., IDEKER, R. E. & SMITH, W. M. 1998. Estimation of conduction velocity vector fields from epicardial mapping data. *IEEE Trans Biomed Eng,* 45**,** 563-71.

BEELER, G. W. & REUTER, H. 1977. Reconstruction of the action potential of ventricular myocardial fibres. *J Physiol,* 268**,** 177-210.

BERENFELD, O. & PERTSOV, A. M. 1999. Dynamics of intramural scroll waves in three-dimensional continuous myocardium with rotational anisotropy. *J Theor Biol,* 199**,** 383-94.

BERGER, R. D. 2004. Electrical restitution hysteresis: good memory or delayed response? *Circ Res,* 94**,** 567-9.

BHATIA, R. S., TU, J. V., LEE, D. S., AUSTIN, P. C., FANG, J., HAOUZI, A., GONG, Y. & LIU, P. P. 2006. Outcome of heart failure with preserved ejection fraction in a population-based study. *N Engl J Med,* 355**,** 260-9.

BURKHOFF, D., MIRSKY, I. & SUGA, H. 2005. Assessment of systolic and diastolic ventricular properties via pressure-volume analysis: a guide for clinical, translational, and basic researchers. *Am J Physiol Heart Circ Physiol,* 289**,** H501-12.

CAKULEV, I., EFIMOV, I. R. & WALDO, A. L. 2009. Cardioversion: past, present, and future. *Circulation,* 120**,** 1623-32.

CAO, J. M., QU, Z., KIM, Y. H., WU, T. J., GARFINKEL, A., WEISS, J. N., KARAGUEUZIAN, H. S. & CHEN, P. S. 1999. Spatiotemporal heterogeneity in the induction of ventricular fibrillation by rapid pacing: importance of cardiac restitution properties. *Circ Res,* 84**,** 1318-31.

CARMELIET, E. 1999. Cardiac ionic currents and acute ischemia: from channels to arrhythmias. *Physiol Rev,* 79**,** 917-1017.

CHERRY, E. M. & FENTON, F. H. 2004. Suppression of alternans and conduction blocks despite steep APD restitution: electrotonic, memory, and conduction velocity restitution effects. *Am J Physiol Heart Circ Physiol,* 286**,** H2332-41.

CHUDIN, E., GOLDHABER, J., GARFINKEL, A., WEISS, J. & KOGAN, B. 1999. Intracellular Ca(2+) dynamics and the stability of ventricular tachycardia. *Biophys J,* 77**,** 2930-41.

CLANCY, C. E. & RUDY, Y. 1999. Linking a genetic defect to its cellular phenotype in a cardiac arrhythmia. *Nature,* 400**,** 566-9.

CLANCY, C. E. & RUDY, Y. 2001. Cellular consequences of HERG mutations in the long QT syndrome: precursors to sudden cardiac death. *Cardiovasc Res,* 50**,** 301-13.

CLAYTON, R. H. & HOLDEN, A. V. 2002. A method to quantify the dynamics and complexity of re-entry in computational models of ventricular fibrillation. *Phys Med Biol,* 47**,** 225-38.

CLAYTON, R. H. & PANFILOV, A. V. 2008. A guide to modelling cardiac electrical activity in anatomically detailed ventricles. *Prog Biophys Mol Biol,* 96**,** 19-43.

CLAYTON, R. H. & TAGGART, P. 2005. Regional differences in APD restitution can initiate wave-break and re-entry in cardiac tissue: a compuational study. *BioMedical Engineering OnLine,* 4**,** 54.

CONRATH, C. E., WILDERS, R., CORONEL, R., BAKKER, J. M. T. D., TAGGART, P., GROOT, J. R. D. & OPTHOF, T. 2004. Intercellular coupling through gap junctions masks M cells in the human heart. *Cardiovascular Research,* 62**,** 407-414.

CORABOEUF, E. & WEIDMANN, S. 1949a. *Potentiel De Repos Et Potentiels Daction Du Muscle Cardiaque, Mesures a Laide Delectrodes Internes. *Comptes Rendus Des Seances De La Societe De Biologie Et De Ses Filiales,* 143**,** 1329-1331.

CORABOEUF, E. & WEIDMANN, S. 1949b. *Potentiels Daction Du Muscle Cardiaque Obtenus a Laide De Microelectrodes Intracellulaires - Presence Dune Inversion De Potentiel. *Comptes Rendus Des Seances De La Societe De Biologie Et De Ses Filiales,* 143**,** 1360-1361.

DIFRANCESCO, D. & NOBLE, D. 1985. A model of cardiac electrical activity incorporating ionic pumps and concentration changes. *Philos Trans R Soc Lond B Biol Sci,* 307**,** 353-98.

DOWNAR, E., HARRIS, L., MICKLEBOROUGH, L. L., SHAIKH, N. & PARSON, I. D. 1988. Endocardial mapping of ventricular tachycardia in the intact human ventricle: evidence for reentrant mechanisms. *J Am Coll Cardiol,* 11**,** 783-91.

FABER, G. M. & RUDY, Y. 2000. Action potential and contractility changes in [Na(+)](i) overloaded cardiac myocytes: a simulation study. *Biophys J,* 78**,** 2392-404.

FABIATO, A. 1992. Two kinds of calcium-induced release of calcium from the sarcoplasmic reticulum of skinned cardiac cells. *Adv Exp Med Biol,* 311**,** 245-62.

FENTON, F. H., CHERRY, E. M., HASTINGS, H. M. & EVANS, S. J. 2002. Multiple mechanisms of spiral wave breakup in a model of cardiac electrical activity. *Chaos,* 12**,** 852-892.

FOX, J. J., RICCIO, M. L., DRURY, P., WERTHMAN, A. & JR, R. F. G. 2003. Dynamic mechanism for conduction block in heart tissue. *New Journal o Physics,* 5**,** 101.1-101.14.

FOX, J. J., RICCIO, M. L., HUA, F., BODENSCHATZ, E. & GILMOUR, R. F., JR. 2002. Spatiotemporal transition to conduction block in canine ventricle. *Circ Res,* 90**,** 289-96.

GARFINKEL, A., KIM, Y. H., VOROSHILOVSKY, O., QU, Z., KIL, J. R., LEE, M. H., KARAGUEUZIAN, H. S., WEISS, J. N. & CHEN, P. S. 2000. Preventing ventricular fibrillation by flattening cardiac restitution. *Proc Natl Acad Sci U S A,* 97**,** 6061-6.

GARREY, W. E., FOSTER, M. S. & PHYSIOLOGICAL LABORATORY OF WASHINGTON UNIVERSITY, S. L. 1914. *The nature of fibrillary contraction of the heart : its relation to tissue mass and form,* Norwood, Mass., The Plimpton Press.

GELZER, A., OTANI, N., KOLLER, M., ENYEART, M., MOISE, N. & GILMOUR, R. 2009. Dynamically-Induced Spatial Dispersion of Repolarization and the Development of VF in an Animal Model of Sudden Death. *Comput Cardiol,* 2009**,** 309-312.

GILMOUR, R. F., JR., GELZER, A. R. & OTANI, N. F. 2007. Cardiac electrical dynamics: maximizing dynamical heterogeneity. *J Electrocardiol,* 40**,** S51-5.

GIMA, K. & RUDY, Y. 2002. Ionic current basis of electrocardiographic waveforms: a model study. *Circ Res,* 90**,** 889-96.

GOLDHABER, J. I., XIE, L. H., DUONG, T., MOTTER, C., KHUU, K. & WEISS, J. N. 2005. Action potential duration restitution and alternans in rabbit ventricular myocytes: the key role of intracellular calcium cycling. *Circ Res,* 96**,** 459-66.

GOMES, J., FINLAY, M., AHMED, A. K., CIACCIO, E. J., ASIMAKI, A., SAFFITZ, J. E., QUARTA, G., NOBLES, M., SYRRIS, P., CHAUBEY, S., MCKENNA, W. J., TINKER, A. & LAMBIASE, P. D. 2012. Electrophysiological abnormalities precede overt structural changes in arrhythmogenic right ventricular cardiomyopathy due to mutations in desmoplakin-A combined murine and human study. *Eur Heart J,* 33**,** 1942-53.

GRAY, R. A., JALIFE, J., PANFILOV, A. V., BAXTER, W. T., CABO, C., DAVIDENKO, J. M. & PERTSOV, A. M. 1995. Mechanisms of cardiac fibrillation. *Science,* 270**,** 1222-3; author reply 1224-5.

GRAY, R. A., PERTSOV, A. M. & JALIFE, J. 1998. Spatial and temporal organization during cardiac fibrillation. *Nature,* 392**,** 75-8.

HAN, J. & MOE, G. K. 1964. Nonuniform Recovery of Excitability in Ventricular Muscle. *Circ Res,* 14**,** 44-60.

HANSON, B., SUTTON, P., ELAMERI, N., GRAY, M., CRITCHLEY, H., GILL, J. S. & TAGGART, P. 2009. Interaction of activation-repolarization coupling and restitution properties in humans. *Circ Arrhythm Electrophysiol,* 2**,** 162-70.

HARPOLE, D. H., DAVIDSON, C. J., SKELTON, T. N., KISSLO, K. B., JONES, R. H. & BASHORE, T. M. 1990. Early and late changes in left ventricular systolic performance after percutaneous aortic balloon valvuloplasty. *Am J Cardiol,* 66**,** 327-32.

HARPOLE, D. H., RANKIN, J. S., WOLFE, W. G., SMITH, L. R., YOUNG, W. G., CLEMENTS, F. M. & JONES, R. H. 1989. Assessment of left ventricular functional preservation during isolated cardiac valve operations. *Circulation,* 80**,** III1-9.

HAWS, C. W. & LUX, R. L. 1990. Correlation between in vivo transmembrane action potential durations and activation-recovery intervals from electrograms. Effects of interventions that alter repolarization time. *Circulation,* 81**,** 281-8.

HODGKIN, A. L. 1954. A note on conduction velocity. *J Physiol,* 125**,** 221-4.

HODGKIN, A. L. & HUXLEY, A. F. 1952. A quantitative description of membrane current and its application to conduction and excitation in nerve. *J Physiol,* 117**,** 500-44.

HREN, R., NENONEN, J. & HORACEK, B. M. 1998. Simulated epicardial potential maps during paced activation reflect myocardial fibrous structure. *Ann Biomed Eng,* 26**,** 1022-35.

HUANG, J., ZHOU, X., SMITH, W. M. & IDEKER, R. E. 2004. Restitution Properties During Ventricular Fibrillation in the In Situ Swine Heart. *Circulation,* 110**,** 3161-3167.

HUND, T. J. & RUDY, Y. 2004. Rate dependence and regulation of action potential and calcium transient in a canine cardiac ventricular cell model. *Circulation,* 110**,** 3168-74.

JANSE, M. J., WILMS-SCHOPMAN, F. J. G. & CORONEL, R. 1995. Ventricular fibrillation is not always due to multiple wavelet reentry. *Journal of Cadiovascular Electrophysiology,* 6**,** 512-521.

JORDAN, P. N. & CHRISTINI, D. J. 2004. Determining the effects of memory and action potential duration alternans on cardiac restitution using a constant-memory restitution protocol. *Physiol Meas,* 25**,** 1013-24.

KARMA, A. 1993. Spiral breakup in model equations of action potential propagation in cardiac tissue. *Phys Rev Lett,* 71**,** 1103-1106.

KARMA, A. 1994. Electrical alternans and spiral wave breakup in cardiac tissue. *Chaos,* 4**,** 461-472.

KASS, D. A. & MAUGHAN, W. L. 1988. From 'Emax' to pressure-volume relations: a broader view. *Circulation,* 77**,** 1203-12.

KASS, D. A., MIDEI, M., GRAVES, W., BRINKER, J. A. & MAUGHAN, W. L. 1988. Use of a Conductance (Volume) Catheter and Transient Inferior Vena-Caval Occlusion for Rapid-Determination of Pressure-Volume Relationships in Man. *Catheterization and Cardiovascular Diagnosis,* 15**,** 192-202.

KELDERMANN, R. H., TEN TUSSCHER, K. H., NASH, M. P., HREN, R., TAGGART, P. & PANFILOV, A. V. 2008. Effect of heterogeneous APD restitution on VF organization in a model of the human ventricles. *Am J Physiol Heart Circ Physiol,* 294**,** H764-74.

KIM, B. S., KIM, Y. H., HWANG, G. S., PAK, H. N., LEE, S. C., SHIM, W. J., OH, D. J. & RO, Y. M. 2002. Action potential duration restitution kinetics in human atrial fibrillation. *J Am Coll Cardiol,* 39**,** 1329-36.

KLEBER, A. G., JANSE, M. J., WILMS-SCHOPMANN, F. J., WILDE, A. A. & CORONEL, R. 1986. Changes in conduction velocity during acute ischemia in ventricular myocardium of the isolated porcine heart. *Circulation,* 73**,** 189-98.

KOBAYASHI, Y., PETERS, W., KHAN, S. S., MANDEL, W. J. & KARAGUEUZIAN, H. S. 1992. Cellular mechanisms of differential action potential duration restitution in canine ventricular muscle cells during single versus double premature stimuli. *Circulation,* 86**,** 955-67.

KODAMA, I., WILDE, A., JANSE, M. J., DURRER, D. & YAMADA, K. 1984. Combined effects of hypoxia, hyperkalemia and acidosis on membrane action potential and excitability of guinea-pig ventricular muscle. *J Mol Cell Cardiol,* 16**,** 247-59.

KOHL, P. & SACHS, F. 2001. Mechanoelectric feedback in cardiac cells. *Philosophical Transactions of the Royal Society a-Mathematical Physical and Engineering Sciences,* 359**,** 1173-1185.

KRINSKY, V. I. 1966. Spread of excitation in an inhomogeneous medium (state similar to cardiac fibrillation). *Biophys.,* 11**,** 776-784.

KUO, C. S., MUNAKATA, K., REDDY, C. P. & SURAWICZ, B. 1983. Characteristics and possible mechanism of ventricular arrhythmia dependent on the dispersion of action potential durations. *Circulation,* 67**,** 1356-67.

KURAMOTO, Y. & KOGA, S. 1981. Turbulized rotating chemical waves. *Prog. Theor. Phys.,* 66**,** 1081-1085.

LAMBIASE, P. D., AHMED, A. K., CIACCIO, E. J., BRUGADA, R., LIZOTTE, E., CHAUBEY, S., BEN-SIMON, R., CHOW, A. W., LOWE, M. D. & MCKENNA, W. J. 2009. High-density substrate mapping in Brugada syndrome: combined role of conduction and repolarization heterogeneities in arrhythmogenesis. *Circulation,* 120**,** 106-17, 1-4.

LEVICK, J. R. 2003. *An introduction to cardiovascular physiology,* London, Arnold.

LINZ, K. W. & MEYER, R. 1998. Control of L-type calcium current during the action potential of guinea-pig ventricular myocytes. *J Physiol,* 513 (Pt 2)**,** 425-42.

LUO, C. H. & RUDY, Y. 1994. A dynamic model of the cardiac ventricular action potential. I. Simulations of ionic currents and concentration changes. *Circ Res,* 74**,** 1071-96.

MARCULS L. KOLLER, M. L. R., ROBERT F. GILMOUR 1998. Dynamic restitution of action potential duration during electrical alternans and ventricular fibrillation. *Am J Physiol Heart Circ Physiol,* 275**,** 1635-1642.

MASON, D. T., BRAUNWALD, E., COVELL, J. W., SONNENBLICK, E. H. & ROSS, J., JR. 1971. Assessment of cardiac contractility. The relation between the rate of pressure rise and ventricular pressure during isovolumic systole. *Circulation,* 44**,** 47-58.

MCALLISTER, R. E., NOBLE, D. & TSIEN, R. W. 1975. Reconstruction of the electrical activity of cardiac Purkinje fibres. *J Physiol,* 251**,** 1-59.

MCWILLIAM, J. A. 1887. Fibrillar Contraction of the Heart. *J Physiol,* 8**,** 296-310.

MCWILLIAM, J. A. 1889. Electrical Stimulation of the Heart in Man. *Br Med J,* 1**,** 348-50.

MINES, G. R. 1913. On dynamic equilibrium in the heart. *J Physiol,* 46**,** 349-83.

MIRONOV, S., JALIFE, J. & TOLKACHEVA, E. G. 2008. Role of conduction velocity restitution and short-term memory in the development of action potential duration alternans in isolated rabbit hearts. *Circulation,* 118**,** 17-25.

MOE, G. K., RHEINBOLDT, W. C. & ABILDSKOV, J. A. 1964. A Computer Model of Atrial Fibrillation. *Am Heart J,* 67**,** 200-20.

MOSS, A. J., ZAREBA, W., HALL, W. J., KLEIN, H., WILBER, D. J., CANNOM, D. S., DAUBERT, J. P., HIGGINS, S. L., BROWN, M. W. & ANDREWS, M. L. 2002. Prophylactic implantation of a defibrillator in patients with myocardial infarction and reduced ejection fraction. *N Engl J Med,* 346**,** 877-83.

NAM, G. B., KO, K. H., KIM, J., PARK, K. M., RHEE, K. S., CHOI, K. J., KIM, Y. H. & ANTZELEVITCH, C. 2010. Mode of onset of ventricular fibrillation in patients with early repolarization pattern vs. Brugada syndrome. *Eur Heart J,* 31**,** 330-9.

NEHER, E. & SAKMANN, B. 1976. Single-channel currents recorded from membrane of denervated frog muscle fibres. *Nature,* 260**,** 799-802.

NIELSEN, P. M., LE GRICE, I. J., SMAILL, B. H. & HUNTER, P. J. 1991. Mathematical model of geometry and fibrous structure of the heart. *Am J Physiol,* 260**,** H1365-78.

NOBLE, D., VARGHESE, A., KOHL, P. & NOBLE, P. 1998. Improved guinea-pig ventricular cell model incorporating a diadic space, IKr and IKs, and length- and tension-dependent processes. *Can J Cardiol,* 14**,** 123-34.

NOBLE, M. I. 1968. The contribution of blood momentum to left ventricular ejection in the dog. *Circ Res,* 23**,** 663-70.

NOLASCO, J. B. & DAHLEN, R. W. 1968. A graphic method for the study of alternation in cardiac action potentials. *J Appl Physiol,* 25**,** 191-6.

NYGREN, A. & HALTER, J. A. 1999. A general approach to modeling conduction and concentration dynamics in excitable cells of concentric cylindrical geometry. *J Theor Biol,* 199**,** 329-58.

O'HARA, T., VIRAG, L., VARRO, A. & RUDY, Y. 2011. Simulation of the undiseased human cardiac ventricular action potential: model formulation and experimental validation. *PLoS Comput Biol,* 7**,** e1002061.

OTANI, N. F. 2007. Theory of action potential wave block at-a-distance in the heart. *Phys Rev E Stat Nonlin Soft Matter Phys,* 75**,** 021910.

OWAN, T. E., HODGE, D. O., HERGES, R. M., JACOBSEN, S. J., ROGER, V. L. & REDFIELD, M. M. 2006. Trends in prevalence and outcome of heart failure with preserved ejection fraction. *N Engl J Med,* 355**,** 251-9.

PANFILOV, A. V. 1999. Three-dimensional organization of electrical turbulence in the heart. *Phys Rev E Stat Phys Plasmas Fluids Relat Interdiscip Topics,* 59**,** R6251-4.

PARMLEY, W. W., DIAMOND, G., TOMODA, H., FORRESTER, J. S. & SWAN, H. J. 1972. Clinical evaluation of left ventricular pressures in myocardial infarction. *Circulation,* 45**,** 358-66.

POTSE, M., VINET, A., OPTHOF, T. & CORONEL, R. 2009. Validation of a simple model for the morphology of the T wave in unipolar electrograms. *Am J Physiol Heart Circ Physiol,* 297**,** H792-801.

QU, Z., GARFINKEL, A., CHEN, P. S. & WEISS, J. N. 2000. Mechanisms of discordant alternans and induction of reentry in simulated cardiac tissue. *Circulation,* 102**,** 1664-70.

QU, Z., WEISS, J. N. & GARFINKEL, A. 1999. Cardiac electrical restitution properties and stability of reentrant spiral waves: a simulation study. *Am J Physiol,* 276**,** H269-83.

RASMUSSON, R. L., CLARK, J. W., GILES, W. R., ROBINSON, K., CLARK, R. B., SHIBATA, E. F. & CAMPBELL, D. L. 1990. A mathematical model of electrophysiological activity in a bullfrog atrial cell. *Am J Physiol,* 259**,** H370-89.

REUTER, H. 1983. Calcium channel modulation by neurotransmitters, enzymes and drugs. *Nature,* 301**,** 569-74.

REUTER, H. & SCHOLZ, H. 1968. [On the influence of the extracellular Ca concentration on membrane potential and contraction of isolated heart preparations during graded depolarization]. *Pflugers Arch Gesamte Physiol Menschen Tiere,* 300**,** 87-107.

RICCIO, M. L., KOLLER, M. L. & GILMOUR, R. F., JR. 1999. Electrical restitution and spatiotemporal organization during ventricular fibrillation. *Circ Res,* 84**,** 955-63.

RODRIGUEZ, B., EASON, J. C. & TRAYANOVA, N. 2006a. Differences between left and right ventricular anatomy determine the types of reentrant circuits induced by an external electric shock. A rabbit heart simulation study. *Progress in Biophysics & Molecular Biology,* 90**,** 399-413.

RODRIGUEZ, B., TRAYANOVA, N. & NOBLE, D. 2006b. Modeling cardiac ischemia. *Ann N Y Acad Sci,* 1080**,** 395-414.

ROGERS, J. M. 2002. Wave front fragmentation due to ventricular geometry in a model of the rabbit heart. *Chaos,* 12**,** 779-787.

ROGERS, J. M., HUANG, J., SMITH, W. M. & IDEKER, R. E. 1999. Incidence, evolution, and spatial distribution of functional reentry during ventricular fibrillation in pigs. *Circ Res,* 84**,** 945-54.

RUDY, Y. & SILVA, J. R. 2006. Computational biology in the study of cardiac ion channels and cell electrophysiology. *Q Rev Biophys,* 39**,** 57-116.

SAMPSON, K. J. & HENRIQUEZ, C. S. 2001. Simulation and prediction of functional block in the presence of structural and ionic heterogeneity. *Am J Physiol Heart Circ Physiol,* 281**,** H2597-603.

SATO, D., XIE, Y., WEISS, J. N., QU, Z., GARFINKEL, A. & SANDERSON, A. R. 2009. Acceleration of cardiac tissue simulation with graphic processing units. *Med Biol Eng Comput,* 47**,** 1011-5.

SELFRIDGE, O. 1948. Studies on flutter and fibrillation; some notes on the theory of flutter. *Arch Inst Cardiol Mex,* 18**,** 177-87.

SHAH, P. K., PICHLER, M., BERMAN, D. S., SINGH, B. N. & SWAN, H. J. 1980. Left ventricular ejection fraction determined by radionuclide ventriculography in early stages of first transmural myocardial infarction. Relation to short-term prognosis. *Am J Cardiol,* 45**,** 542-6.

SHAW, R. M. & RUDY, Y. 1997. Electrophysiologic effects of acute myocardial ischemia. A mechanistic investigation of action potential conduction and conduction failure. *Circ Res,* 80**,** 124-38.

SISO-NADAL, F., OTANI, N. F., GILMOUR, R. F., JR. & FOX, J. J. 2008. Boundary-induced reentry in homogeneous excitable tissue. *Phys Rev E Stat Nonlin Soft Matter Phys,* 78**,** 031925.

SPACCAVENTO, L. J., GRASSMAN, E. D., BRIESBLATT, W. M. & SCHWARTZ, R. S. 1990. Effect of ischemia on ventricular contractility in patients with coronary artery disease. *Angiology,* 41**,** 486-91.

SPIELMAN, S. R., FARSHIDI, A., HOROWITZ, L. N. & JOSEPHSON, M. E. 1978. Ventricular fibrillation during programmed ventricular stimulation: incidence and clinical implications. *Am J Cardiol,* 42**,** 913-8.

STARLING, M. R., GROSS, M. D., WALSH, R. A., MANCINI, G. B. J. & BLUMHARDT, R. 1988. Radionuclide Determination of the Relationship between Left-Ventricular Contractile State and Ejection Fraction. *American Heart Journal,* 116**,** 790-798.

STEVENS, C., REMME, E., LEGRICE, I. & HUNTER, P. 2003. Ventricular mechanics in diastole: material parameter sensitivity. *J Biomech,* 36**,** 737-48.

SWISSA, M., QU, Z., OHARA, T., LEE, M. H., LIN, S. F., GARFINKEL, A., KARAGUEUZIAN, H. S., WEISS, J. N. & CHEN, P. S. 2002. Action potential duration restitution and ventricular fibrillation due to rapid focal excitation. *Am J Physiol Heart Circ Physiol,* 282**,** H1915-23.

TABEREAUX, P. B., DOSDALL, D. J. & IDEKER, R. E. 2009. Mechanisms of VF maintenance: wandering wavelets, mother rotors, or foci. *Heart Rhythm,* 6**,** 405-15.

TAGGART, P., SUTTON, P. M., OPTHOF, T., CORONEL, R., TRIMLETT, R., PUGSLEY, W. & KALLIS, P. 2000. Inhomogeneous transmural conduction during early ischaemia in patients with coronary artery disease. *J Mol Cell Cardiol,* 32**,** 621-30.

TASAKI, I. & HAGIWARA, S. 1957. Capacity of muscle fiber membrane. *Am J Physiol,* 188**,** 423-9.

TAYLOR, D. E., WADE, J. D., SHISHODIA, M. S. & HIDER, C. F. 1968. Effects of selective myocardial inactivation on left ventricular function during the isovolumetric phase of systole. *Q J Exp Physiol Cogn Med Sci,* 53**,** 273-81.

TEN TUSSCHER, K. H., NOBLE, D., NOBLE, P. J. & PANFILOV, A. V. 2004. A model for human ventricular tissue. *Am J Physiol Heart Circ Physiol,* 286**,** H1573-89.

TRAYANOVA, N. 2006. Defibrillation of the heart: insights into mechanisms from modelling studies. *Experimental Physiology,* 91**,** 323-337.

VEENSTRA, R. D., JOYNER, R. W., WIEDMANN, R. T., YOUNG, M. L. & TAN, R. C. 1987. Effects of hypoxia, hyperkalemia, and metabolic acidosis on canine subendocardial action potential conduction. *Circ Res,* 60**,** 93-101.

VETTER, F. J. & MCCULLOCH, A. D. 1998. Three-dimensional analysis of regional cardiac function: a model of rabbit ventricular anatomy. *Prog Biophys Mol Biol,* 69**,** 157-83.

VIGMOND, E. J., AGUEL, F. & TRAYANOVA, N. A. 2002. Computational techniques for solving the bidomain equations in three dimensions. *IEEE Trans Biomed Eng,* 49**,** 1260-9.

VISWANATHAN, P. C., SHAW, R. M. & RUDY, Y. 1999. Effects of IKr and IKs heterogeneity on action potential duration and its rate dependence: a simulation study. *Circulation,* 99**,** 2466-74.

VON SCHEIDT, W., ZIEGLER, U., KEMKES, B. M. & ERDMANN, E. 1991. Heart transplantation: hemodynamics over a five-year period. *J Heart Lung Transplant,* 10**,** 342-50.

WALTON, M. K. & FOZZARD, H. A. 1983. The conducted action potential. Models and comparison to experiments. *Biophys J,* 44**,** 9-26.

WATANABE, M. A., FENTON, F. H., EVANS, S. J., HASTINGS, H. M. & KARMA, A. 2001. Mechanisms for discordant alternans. *J Cardiovasc Electrophysiol,* 12**,** 196-206.

WEIDMANN, S. 1952. The electrical constants of Purkinje fibres. *J Physiol,* 118**,** 348-60.

WEIDMANN, S. 1966. The diffusion of radiopotassium across intercalated disks of mammalian cardiac muscle. *J Physiol,* 187**,** 323-42.

WEIDMANN, S. 1970. Electrical constants of trabecular muscle from mammalian heart. *J Physiol,* 210**,** 1041-54.

WEISS, J. N., GARFINKEL, A., KARAGUEUZIAN, H. S., QU, Z. & CHEN, P. S. 1999. Chaos and the transition to ventricular fibrillation: a new approach to antiarrhythmic drug evaluation. *Circulation,* 99**,** 2819-26.

WIENER, N. & ROSENBLUETH, A. 1946. The mathematical formulation of the problem of conduction of impulses in a network of connected excitable elements, specifically in cardiac muscle. *Arch Inst Cardiol Mex,* 16**,** 205-65.

WIGGERS, C. J. 1940. The mechanism and nature of ventricular fibrillation. *American Heart Journal***,** 399-412.

WIGGERS, C. J., BELL, J. R. & PAINE, M. 2003. Studies of ventricular fibrillation caused by electric shock: II. Cinematographic and electrocardiographic observations of the natural process in the dog's heart. Its inhibition by potassium and the revival of coordinated beats by calcium. *Ann Noninvasive Electrocardiol,* 8**,** 252-61; discussion 251.

WIT, A. L. & JANSE, M. J. 1992. Experimental models of ventricular tachycardia and fibrillation caused by ischemia and infarction. *Circulation,* 85**,** I32-42.

WITKOWSKI, F. X., LEON, L. J., PENKOSKE, P. A., GILES, W. R., SPANO, M. L., DITTO, W. L. & WINFREE, A. T. 1998. Spatiotemporal evolution of ventricular fibrillation. *Nature,* 392**,** 78-82.

XIE, F., QU, Z., YANG, J., BAHER, A., WEISS, J. N. & GARFINKEL, A. 2004. A simulation study of the effects of cardiac anatomy in ventricular fibrillation. *J Clin Invest,* 113**,** 686-93.

YUE, A. M., PAISEY, J. R., ROBINSON, S., BETTS, T. R., ROBERTS, P. R. & MORGAN, J. M. 2004. Determination of human ventricular repolarization by noncontact mapping: validation with monophasic action potential recordings. *Circulation,* 110**,** 1343-50.

YUUKI, K., HOSOYA, Y., KUBOTA, I. & YAMAKI, M. 2004. Dynamic and not static change in ventricular repolarization is a substrate of ventricular arrhythmia on chronic ischemic myocardium. *Cardiovascular Research,* 63**,** 645-652.

ZHONG, J., HWANG, T. C., ADAMS, H. R. & RUBIN, L. J. 1997. Reduced L-type calcium current in ventricular myocytes from endotoxemic guinea pigs. *Am J Physiol,* 273**,** H2312-24.

ZIPES, D. P. & JALIFE, J. 2009. *Cardiac electrophysiology : from cell to bedside,* Philadelphia, Pa., Saunders/Elsevier.

ZORNOFF, L. A., SKALI, H., PFEFFER, M. A., ST JOHN SUTTON, M., ROULEAU, J. L., LAMAS, G. A., PLAPPERT, T., ROULEAU, J. R., MOYE, L. A., LEWIS, S. J., BRAUNWALD, E. & SOLOMON, S. D. 2002. Right ventricular dysfunction and risk of heart failure and mortality after myocardial infarction. *J Am Coll Cardiol,* 39**,** 1450-5.

Appendix 1

	C_6	Resting potential (mV)	APD_{SS} (ms)	B_{APD}	C_{APD}	Slope
	30	-88.9356	214.5	21.6472	-0.0074	0.1494
	50	-89.9424	215.8	27.3126	-0.0087	0.2173
	100	-88.9493	218.2	35.0667	-0.0088	0.283
	150	-88.9519	219.5	38.0789	-0.0084	0.2947
	200	-88.9533	220.1	39.2712	-0.0082	0.2978
	400	-88.9558	221	39.4604	-0.0077	0.2829
Mean	155	-89.1147	218.1833	33.47283	-0.0082	0.254183
SD	135.4622	0.405543	2.552972	7.362369	0.000555	0.059227

Table A.1.1: Influence of intracellular Calcium ion concentration on APD restitution properties (C_6 in equation 4.4). SD: standard deviation; slope of APD restitution is calculated at DI=10ms. Shaded row indicates initial conditions used in simulation studies are the same with those in ORd model

	C_7	Resting potential (mV)	APD_{SS} (ms)	B_{APD}	C_{APD}	Slope
	0.00012	-89.9493	218.2	35.0667	-0.0088	0.283
	0.0006	-88.9386	204.3	31.932	-0.0078	0.2296
	0.0012	-88.9342	200	32.4943	-0.0077	0.2322
	0.0024	-88.9307	197	33.1314	-0.0077	0.2368
	0.0036	-88.9291	195.8	33.5494	-0.0077	0.24
	0.012	-88.9262	193.8	34.3511	-0.0077	0.2459
Mean	0.00332	-89.1014	201.5167	33.42082	-0.0079	0.244583
SD	0.004436	0.415431	8.955538	1.161866	0.000443	0.019683

Table A.1.2: Influence of intracellular Calcium ion concentration on APD restitution properties (C_7 in equation 4.4). SD: standard deviation; slope of APD restitution is calculated at DI=10ms. Shaded row indicates initial conditions used in simulation studies are the same with those in ORd model

	G_{to}	Resting potential (mV)	APD_{SS} (ms)	B_{APD}	C_{APD}	Slope
	0.01	-88.9339	216.7	34.6227	-0.0086	0.2744
	0.02	-88.9493	218.2	35.0667	-0.0088	0.283
	0.04	-88.9779	221.4	34.0542	-0.0085	0.2648
	0.073	-89.0206	226.9	35.0969	-0.009	0.2896
	0.08	-89.0291	228.1	35.5201	-0.0092	0.2981
	0.12	-88.8986	234.8	35.2837	-0.0093	0.2976
Mean	0.057167	-88.9682	224.35	34.94072	-0.0089	0.284583
SD	0.041523	0.050846	6.852956	0.525478	0.000322	0.013228

Table A.1.3: Influence of intracellular Calcium ion concentration on APD restitution properties (G_{to} in equation A.11.55). SD: standard deviation; slope of APD restitution is calculated at DI=10ms. Shaded row indicates initial conditions used in simulation studies are the same with those in ORd model

Appendix 2

Patient ID		1	2	3	4	5	6
Number of electrode		15	62	93	31	28	62
APD_{SS} (ms)	Max	250.833	261.095	198.089	221.667	197.991	178.929
	Min	234.167	168.144	120.914	182.500	153.555	164.496
	Mean	242.044	207.467	164.906	204.199	175.770	170.631
	SD	4.943	22.091	18.507	10.871	10.640	3.268
Slope	Max	6.582	11.413	13.773	9.828	45.418	10.382
	Min	0.149	0.120	0.071	0.383	0.124	0.488
	Mean	2.103	3.229	2.098	2.157	6.266	4.525
	SD	1.779	2.714	3.195	1.936	13.781	1.984
R^2	Max	0.968	0.928	0.980	0.909	0.974	0.941
	Min	0.707	0.724	0.702	0.719	0.712	0.745
	Mean	0.921	0.820	0.867	0.841	0.894	0.875
	SD	0.070	0.054	0.091	0.051	0.069	0.058
RMSE	Max	13.075	33.091	51.492	12.482	13.253	17.463
	Min	3.598	3.117	0.908	5.676	2.420	3.889
	Mean	7.254	10.934	10.828	7.989	5.699	7.181
	SD	2.522	7.348	10.468	1.739	2.738	3.894
R^2 for linear regression under the minimum coupling interval		0.009	0.452	0.030	0.075	0.094	0.043
RMSE for linear regression under the minimum coupling interval		18.302	16.691	15.418	8.139	12.983	5.643

Table A.2.1: APD restitution modelling results (part 1). Slopes of APD restitution curves were calculate at DI=10ms.

Patient ID		7	8	9	10	11	12
Number of electrode		11	31	22	22	2	31
APD_{SS} (ms)	Max	210.955	199.156	212.841	183.724	223.333	235.964
	Min	154.020	139.902	153.443	135.296	217.500	185.102
	Mean	168.831	165.736	173.182	172.798	220.417	202.838
	SD	15.626	17.222	14.564	9.978	4.125	13.222
Slope	Max	2.251	16.659	25.594	48.581	2.985	11.071
	Min	0.730	0.064	0.842	0.262	1.041	0.024
	Mean	1.428	6.218	3.754	11.515	2.013	2.034
	SD	0.535	5.540	5.721	16.533	1.375	3.075
R^2	Max	0.907	0.890	0.923	0.772	0.838	0.837
	Min	0.791	0.723	0.731	0.716	0.727	0.707
	Mean	0.840	0.814	0.874	0.743	0.783	0.758
	SD	0.040	0.058	0.054	0.025	0.079	0.047
RMSE	Max	12.471	39.892	24.030	14.342	13.022	11.451
	Min	2.718	3.985	4.971	3.803	7.979	5.879
	Mean	5.112	13.747	9.545	6.309	10.501	7.449
	SD	3.002	9.152	6.092	3.019	3.566	1.132
R^2 for linear regression under the minimum coupling interval		0.136	0.249	0.847	0.044		0.690
RMSE for linear regression under the minimum coupling interval		8.798	12.221	4.807	11.294		6.100

Table A.2.2: APD restitution modelling results (part 2). Slopes of APD restitution curves were calculate at DI=10ms.

Patient ID		13	14	15	16	17	18
Number of electrode		62	17	31	31	12	28
APD_{SS} (ms)	Max	253.095	305.053	408.994	216.198	179.924	241.774
	Min	204.091	164.188	114.598	142.739	156.344	167.634
	Mean	227.936	190.656	215.813	183.333	168.825	214.270
	SD	8.715	31.553	51.525	21.552	7.572	17.546
Slope	Max	9.978	33.932	19.097	2.351	4.766	44.930
	Min	0.154	0.503	0.452	0.359	1.229	0.520
	Mean	0.986	8.747	4.011	1.102	2.447	9.272
	SD	1.416	10.969	5.173	0.549	0.871	12.065
R^2	Max	0.944	0.964	0.885	0.976	0.908	0.923
	Min	0.718	0.770	0.711	0.719	0.725	0.756
	Mean	0.867	0.903	0.818	0.888	0.838	0.837
	SD	0.060	0.068	0.053	0.092	0.061	0.042
RMSE	Max	31.070	13.813	15.077	43.785	47.271	28.747
	Min	1.511	4.078	5.402	2.144	4.325	4.947
	Mean	7.267	7.689	8.682	19.532	16.304	10.215
	SD	5.632	2.585	2.786	12.590	15.777	4.170
R^2 for linear regression under the minimum coupling interval		0.074	0.215	0.806	0.765	0.151	0.255
RMSE for linear regression under the minimum coupling interval		11.838	9.015	6.070	11.526	40.328	13.569

Table A.2.3: APD restitution modelling results (part 3). Slopes of APD restitution curves were calculate at DI=10ms.

Patient ID		19	20	21	22	23	24
Number of electrode		14	31	93	28	28	28
APD_{SS} (ms)	Max	194.237	232.127	239.167	359.486	266.538	257.146
	Min	163.449	175.923	197.157	237.930	168.927	215.368
	Mean	181.293	201.270	218.503	264.824	212.882	235.088
	SD	11.418	11.221	10.962	30.403	20.313	14.241
Slope	Max	31.112	3.105	13.353	11.412	40.082	4.269
	Min	1.572	0.645	0.097	0.224	0.670	0.214
	Mean	10.725	1.569	1.044	1.501	9.281	2.146
	SD	10.534	0.779	1.940	2.496	10.070	1.530
R^2	Max	0.945	0.912	0.909	0.971	0.977	0.992
	Min	0.787	0.712	0.707	0.701	0.730	0.705
	Mean	0.874	0.817	0.807	0.883	0.905	0.903
	SD	0.064	0.058	0.065	0.092	0.074	0.099
RMSE	Max	14.402	13.366	41.727	16.392	11.390	12.567
	Min	3.752	5.528	4.531	4.040	2.858	4.441
	Mean	8.141	7.983	11.923	8.536	4.763	7.219
	SD	2.982	1.732	5.804	3.464	1.984	2.071
R^2 for linear regression under the minimum coupling interval		0.330	0.215	0.067	0.347	0.059	0.188
RMSE for linear regression under the minimum coupling interval		13.302	6.964	16.821	15.205	20.547	14.872

Table A.2.4: APD restitution modelling results (part 4). Slopes of APD restitution curves were calculate at DI=10ms.

Appendix 3

Patient ID		1	2	3	4	5	6
Number of electrode		24	24	24	24	24	24
APD_{SS} (ms)	Max	217.359	224.198	220.086	251.364	247.045	241.888
	Min	176.159	187.593	149.440	181.052	184.070	157.238
	Mean	197.943	207.065	192.724	216.684	220.727	211.404
	SD	9.546	9.822	18.234	22.806	21.092	24.219
Slope	Max	29.179	2.934	8.689	17.943	34.299	12.421
	Min	0.488	0.216	0.539	0.642	0.528	0.404
	Mean	2.919	1.212	2.907	3.576	9.092	2.259
	SD	5.938	0.854	2.374	3.877	10.172	2.361
R^2	Max	0.906	0.880	0.860	0.892	0.929	0.772
	Min	0.719	0.722	0.729	0.715	0.703	0.732
	Mean	0.814	0.802	0.796	0.790	0.797	0.749
	SD	0.062	0.067	0.058	0.070	0.078	0.021
RMSE	Max	16.469	23.860	27.455	19.407	30.205	40.479
	Min	5.957	7.381	7.737	2.388	7.044	9.190
	Mean	9.832	12.158	10.992	10.516	13.862	19.231
	SD	2.909	3.329	4.371	4.407	5.375	7.506
R^2 for linear regression under the minimum coupling interval		0.00005	0.546	0.660	0.703	0.279	0.631
RMSE for linear regression under the minimum coupling interval		17.925	14.543	16.475	14.974	18.443	19.704

Table A.3.1: APD restitution modelling results for ARVC patients (part 1). Slopes of APD restitution curves were calculate at DI=10ms.

Patient ID		7	8	9	10	11	12
Number of electrode		24	24	24	24	24	24
APD_{SS} (ms)	Max	205.360	226.392	202.510	221.499	262.771	262.292
	Min	164.891	160.417	143.044	129.453	214.676	198.110
	Mean	182.841	201.621	186.224	191.514	233.195	222.638
	SD	13.151	13.727	12.740	21.120	9.495	19.213
Slope	Max	8.104	9.428	11.551	4.980	5.813	27.400
	Min	0.269	0.110	1.467	0.339	0.049	0.030
	Mean	2.075	3.225	3.290	1.865	0.971	4.591
	SD	1.997	2.084	2.352	1.317	1.672	7.923
R^2	Max	0.946	0.721	0.956	0.909	0.937	0.882
	Min	0.713	0.710	0.738	0.710	0.718	0.748
	Mean	0.814	0.716	0.872	0.817	0.819	0.815
	SD	0.075	0.006	0.065	0.070	0.080	0.094
RMSE	Max	18.249	19.149	23.163	18.399	13.479	26.213
	Min	4.392	13.138	5.399	2.821	1.149	6.270
	Mean	8.260	16.290	8.318	9.081	5.612	13.952
	SD	3.091	1.606	3.785	3.466	3.940	4.579
R^2 for linear regression under the minimum coupling interval		0.052	0.520	0.126	0.403	0.030	0.070
RMSE for linear regression under the minimum coupling interval		6.229	13.238	14.534	19.946	19.948	25.471

Table A.3.2: APD restitution modelling results for ARVC patients (part 2). Slopes of APD restitution curves were calculate at DI=10ms.

Patient ID		13	14
Number of electrode		24	24
APD_{SS} (ms)	Max	221.9904	247.1598
	Min	155.0698	202.0743
	Mean	197.3038	224.2289
	SD	17.97429	12.89896
Slope	Max	7.844717	27.20084
	Min	0.123123	0.020271
	Mean	2.437095	5.682128
	SD	2.131648	6.579462
R^2	Max	0.889724	0.935632
	Min	0.738708	0.766068
	Mean	0.827917	0.881743
	SD	0.050377	0.06042
RMSE	Max	39.14667	29.52199
	Min	4.49208	5.915981
	Mean	13.68896	11.03432
	SD	8.516751	6.944816
R^2 for linear regression under the minimum coupling interval		0.1657	0.54
RMSE for linear regression under the minimum coupling interval		25.0026	12.428

Table A.3.3: APD restitution modelling results for ARVC patients (part 3). Slopes of APD restitution curves were calculate at DI=10ms.

Appendix 4

Patient ID		1	2	3	4	5	6
Number of electrode		28	28	22	17	31	25
APD_{SS} (ms)	Max	359.486	266.538	183.724	305.053	408.994	217.885
	Min	237.930	168.927	135.296	164.188	114.598	76.896
	Mean	264.824	212.882	172.798	190.656	215.813	182.093
	SD	30.403	20.313	9.978	31.553	51.525	25.413
Slope	Max	11.412	40.082	48.581	33.932	19.097	10.592
	Min	0.224	0.670	0.262	0.503	0.452	0.760
	Mean	1.501	9.281	11.515	8.747	4.011	2.928
	SD	2.496	10.070	16.533	10.969	5.173	2.040
R^2	Max	0.971	0.977	0.772	0.964	0.885	0.976
	Min	0.701	0.730	0.716	0.770	0.711	0.776
	Mean	0.883	0.905	0.743	0.903	0.818	0.913
	SD	0.092	0.074	0.025	0.068	0.053	0.061
RMSE	Max	16.392	11.390	14.342	13.813	15.077	11.054
	Min	4.040	2.858	3.803	4.078	5.402	2.898
	Mean	8.536	4.763	6.309	7.689	8.682	5.408
	SD	3.464	1.984	3.019	2.585	2.786	2.275
R^2 for linear regression under the minimum coupling interval		0.347	0.148	0.044	0.148	0.806	0.899
RMSE for linear regression under the minimum coupling interval		15.205	17.311	11.294	15.388	6.070	3.200

Table A.4.1: APD restitution modelling results for patients undergoing extra-stimuli experiment.

Slopes of APD restitution curves were calculate at DI=10ms.

Appendix 5

Patient ID		1	2	3	4	5	6
AT_{SS} (ms)	Max	125.085	147.348	87.583	93.333	135.679	66.048
	Min	96.859	77.000	54.118	29.167	20.500	37.905
	Δ	28.226	70.348	33.466	64.167	115.179	28.143
AT_{S2} (ms)	Max	194.583	211.250	152.500	141.667	172.500	96.667
	Min	155.417	112.583	100.833	65.833	50.000	71.667
	Δ	39.167	98.667	51.667	75.833	122.500	25.000
R^2	Max	0.943	0.974	0.962	0.945	0.961	0.990
	Min	0.833	0.727	0.796	0.890	0.791	0.735
	Mean	0.887	0.890	0.883	0.927	0.895	0.907
	SD	0.030	0.071	0.034	0.015	0.055	0.045
RMSE	Max	6.909	28.483	13.272	26.686	6.422	7.356
	Min	4.398	1.905	4.183	3.135	2.571	0.525
	Mean	5.666	10.610	7.021	4.578	4.305	3.170
	SD	0.758	7.849	1.793	4.153	1.065	1.336

Table A.5.1: CV restitution modelling results (part 1). Δ represents the variance between the maximum activation time and minimum activation time for investigated sites; R^2 and RMSE were calculated by comparing the simulated activation time with experimental data of activation time.

Patient ID		7	8	9	10	11	12
AT_{SS} (ms)	Max	51.762	88.496	95.193	76.018	113.333	178.293
	Min	21.333	39.144	3.568	13.607	79.167	127.805
	Δ	30.429	49.353	91.625	62.411	34.167	50.488
AT_{S2} (ms)	Max	75.000	130.833	229.366	111.073	179.167	215.000
	Min	31.000	89.167	137.741	48.662	143.333	172.000
	Δ	44.000	41.667	91.625	62.411	35.833	43.000
R^2	Max	0.963	0.955	0.935	0.913	NaN	0.995
	Min	0.891	0.767	0.842	0.866	NaN	0.794
	Mean	0.936	0.900	0.910	0.900	NaN	0.974
	SD	0.020	0.045	0.022	0.014	NaN	0.037
RMSE	Max	1.691	7.634	11.081	3.065	50.873	6.209
	Min	1.238	2.661	7.090	2.475	43.743	0.477
	Mean	1.456	4.496	8.312	2.639	47.308	1.602
	SD	0.132	1.380	0.939	0.178	5.042	1.141

Table A.5.2: CV restitution modelling results (part 2). Δ represents the variance between the maximum activation time and minimum activation time for investigated sites; R^2 and RMSE were calculated by comparing the simulated activation time with experimental data of activation time.

Patient ID		13	14	15	16	17	18
AT_{SS} (ms)	Max	124.746	121.961	99.598	75.655	101.389	136.663
	Min	74.856	4.934	30.959	33.036	62.197	20.500
	Δ	49.891	117.026	68.639	42.619	39.192	116.163
AT_{S2} (ms)	Max	162.500	122.500	145.500	110.000	119.583	176.500
	Min	106.667	87.000	48.000	58.333	81.250	29.500
	Δ	55.833	35.500	97.500	51.667	38.333	147.000
R^2	Max	0.967	0.863	0.933	0.963	0.986	0.950
	Min	0.775	0.731	0.713	0.746	0.750	0.841
	Mean	0.858	0.797	0.859	0.906	0.946	0.885
	SD	0.048	0.035	0.058	0.051	0.038	0.038
RMSE	Max	6.754	7.677	6.617	6.416	3.580	9.096
	Min	1.711	3.377	0.809	1.649	0.422	0.751
	Mean	4.602	6.057	3.297	3.534	1.131	2.982
	SD	1.078	1.492	1.789	1.002	0.561	2.134

Table A.5.3: CV restitution modelling results (part 3). Δ represents the variance between the maximum activation time and minimum activation time for investigated sites; R^2 and RMSE were calculated by comparing the simulated activation time with experimental data of activation time.

Patient ID		19	20	21	22	23	24
AT_{SS} (ms)	Max	122.045	163.511	107.176	129.654	128.474	147.829
	Min	18.439	123.103	56.705	19.846	9.487	26.110
	Δ	103.606	40.407	50.471	109.808	118.987	121.720
AT_{S2} (ms)	Max	155.000	180.000	135.000	176.000	153.000	174.500
	Min	55.500	135.667	85.000	42.000	41.000	70.500
	Δ	99.500	44.333	50.000	134.000	112.000	104.000
R^2	Max	0.847	1.000	0.949	0.976	0.979	0.847
	Min	0.700	0.788	0.706	0.724	0.709	0.701
	Mean	0.777	0.885	0.816	0.892	0.847	0.762
	SD	0.040	0.047	0.063	0.054	0.090	0.052
RMSE	Max	7.515	2.219	20.857	10.545	7.726	10.328
	Min	2.998	0.000	2.103	1.830	1.849	4.028
	Mean	5.202	0.989	5.601	7.486	5.139	6.565
	SD	1.301	0.495	3.328	2.509	1.870	1.872

Table A.5.4: CV restitution modelling results (part 4). Δ represents the variance between the maximum activation time and minimum activation time for investigated sites; R^2 and RMSE were calculated by comparing the simulated activation time with experimental data of activation time.

Appendix 6

Patient ID		1	2	3	4	5	6
AT_{SS} (ms)	Max	94.2	100.6	123.3	122.3	143.2	115.5
	Min	51.1	45.3	63.1	40.2	82.8	56.5
	Δ	43.1	55.3	60.2	82.1	60.4	59.0
AT_{S2} (ms)	Max	145	166.7	134.2	200.8	196.6	172.5
	Min	86	100	77.5	107.5	123.3	122.5
	Δ	59	66.7	56.7	93.3	73.3	50
R^2	Max	0.975677	0.933503	0.908787	0.96119	0.978759	0.978731
	Min	0.772284	0.815577	0.703574	0.820173	0.723372	0.759092
	Mean	0.894456	0.895978	0.800659	0.910653	0.921421	0.93728
	SD	0.064961	0.028297	0.06001	0.046725	0.059493	0.052619
RMSE	Max	6.65716	9.51152	8.914711	10.49234	12.1346	6.51331
	Min	2.249933	4.75873	1.267747	2.781155	2.315492	2.558595
	Mean	4.086664	6.187041	2.734035	4.583335	5.698454	4.138922
	SD	1.138638	1.044756	1.732323	1.710512	2.702284	0.817925

Table A.6.1: CV restitution modelling results for ARVC patients (part 1). Δ represents the variance between the maximum activation time and minimum activation time for investigated sites; R^2 and RMSE were calculated by comparing the simulated activation time with experimental data of activation time.

Patient ID		7	8	9	10	11	12
AT_{SS} (ms)	Max	54.2	90.6	60.7	87.8	125.3	65.4
	Min	21.7	13.0	27.8	34.1	65.3	24.9
	Δ	32.5	77.6	32.9	53.7	60.0	40.5
AT_{S2} (ms)	Max	93.5	110.8	108.3	127	194	121.7
	Min	65	67.5	66.7	69.2	131.7	55.8
	Δ	28.5	43.3	41.6	57.8	62.3	65.9
R^2	Max	0.960795	0.958503	0.926123	0.948619	0.959401	0.938847
	Min	0.832647	0.707589	0.796796	0.801043	0.714503	0.746791
	Mean	0.928314	0.887875	0.890992	0.896132	0.907024	0.833749
	SD	0.025439	0.072511	0.028993	0.04124	0.048048	0.041095
RMSE	Max	4.626199	13.8172	7.187779	8.694287	11.25359	10.72248
	Min	2.103298	1.433209	3.379581	3.079748	4.776326	2.893126
	Mean	3.384045	4.055714	4.701926	4.901216	6.745278	5.515536
	SD	0.638785	3.12643	0.754959	1.277078	1.452928	1.795996

Table A.6.2: CV restitution modelling results for ARVC patients (part 2). Δ represents the variance between the maximum activation time and minimum activation time for investigated sites; R^2 and RMSE were calculated by comparing the simulated activation time with experimental data of activation time.

Patient ID		13	14
AT_{SS} (ms)	Max	80.8	115.5
	Min	31.8	69.7
	Δ	49.0	45.8
AT_{S2} (ms)	Max	117.5	167.5
	Min	61.7	127.5
	Δ	55.8	40
R^2	Max	0.966587	0.980928
	Min	0.789243	0.920398
	Mean	0.893663	0.958148
	SD	0.057568	0.012596
RMSE	Max	5.516918	4.56545
	Min	2.475538	3.225556
	Mean	4.066333	3.839635
	SD	0.968751	0.372606

Table A.6.3: CV restitution modelling results for ARVC patients (part 3). Δ represents the variance between the maximum activation time and minimum activation time for investigated sites; R^2 and RMSE were calculated by comparing the simulated activation time with experimental data of activation time.

Appendix 7

Patient ID		1	2	3	4	5	6
AT_{SS} (ms)	Max	129.7	128.5	76.0	121.9	99.6	95.2
	Min	19.8	9.5	13.6	4.9	31.0	3.6
	Δ	109.8	119.0	62.4	117.0	68.6	91.6
AT_{S2} (ms)	Max	176	153	111.1	122.5	145.5	157.4
	Min	42	41	48.7	87	48	65.8
	Δ	134	112	62.4	35.5	97.5	91.6
R^2	Max	0.976208	0.979479	0.912511	0.862871	0.93302	0.928458
	Min	0.724367	0.709324	0.865783	0.731148	0.71264	0.805017
	Mean	0.892282	0.853081	0.900108	0.796677	0.85918	0.89559
	SD	0.054283	0.08811	0.013722	0.034603	0.058319	0.028902
RMSE	Max	10.54451	7.72637	3.065296	7.677289	6.617266	9.391895
	Min	1.830463	1.849392	2.474832	3.376755	0.808853	5.688999
	Mean	7.486193	5.133821	2.638747	6.057233	3.297486	6.815913
	SD	2.509376	1.871604	0.177561	1.491764	1.788897	0.865537

Table A.7.1: CV restitution modelling results for patients undergoing extra-stimuli experiment. Δ represents the variance between the maximum activation time and minimum activation time for investigated sites; R^2 and RMSE were calculated by comparing the simulated activation time with experimental data of activation time.

Appendix 8

Patient ID		1	2	3	4	5	6
DI_{bound} (ms)	Max	4.63	23.18	4.48	5.79	22.81	46.63
	Min	2.11	2.01	2.01	2.04	2	2.05
	Mean	3.37	2.9382	2.3126	2.379	6.1004	18.5248
	SD	1.7819	3.3549	0.514	0.6734	6.0559	12.2497
Patient ID		7	8	9	10	11	12
DI_{bound} (ms)	Max	21.84	6.27	NaN	33.09	NaN	15.01
	Min	2	2.01	NaN	2	NaN	2.01
	Mean	9.987	3.0526	NaN	7.2745	NaN	3.12
	SD	7.4132	1.1435	NaN	7.9679	NaN	2.8296
Patient ID		13	14	15	16	17	18
DI_{bound} (ms)	Max	3.62	21.51	5.15	6.05	29.45	35.16
	Min	2.02	2	2	2.05	2	2.05
	Mean	2.1473	4.3644	2.7457	2.3726	4.1831	6.4808
	SD	0.2316	4.9355	0.9575	0.7242	5.5796	8.8845
Patient ID		19	20	21	22	23	24
DI_{bound} (ms)	Max	21.51	16.48	20.92	5.2	34.19	2.37
	Min	2	2.07	2.01	2	2	2.02
	Mean	4.3644	6.6556	6.0271	2.3135	8.3062	2.148
	SD	4.9355	3.5962	3.9839	0.7499	10.5341	0.1391

Table A.8.1: DI_{bound} calculated for condition of functional block.

Appendix 9

Patient ID		1	2	3	4	5	6
DI_{bound} (ms)	Max	4.71	3.4	37.98	2.19	30.53	18.62
	Min	2	2	2	2	2	2
	Mean	2.2657	2.3783	9.2216	2.0627	5.4195	3.3588
	SD	0.565	0.3717	10.6823	0.0728	7.2388	3.7665
Patient ID		7	8	9	10	11	12
DI_{bound} (ms)	Max	33.28	11.98	4.87	3.61	11.3	37.25
	Min	2	2	2	2	2	2
	Mean	11.3454	4.2543	2.7592	2.2533	3.0917	3.8962
	SD	9.6148	3.1662	0.6021	0.4129	2.8192	7.1594
Patient ID		13			14		
DI_{bound} (ms)	Max	9.96			15.42		
	Min	2			2		
	Mean	2.97			3.495		
	SD	1.708			2.9569		

Table A.9.1: DI_{bound} calculated for condition of functional block for ARVC patients.

Appendix 10

Patient ID		1	2	3	4	5	6
DI_{bound} (ms)	Max	5.2	33.67	33.09	21.51	5.15	NaN
	Min	2	2	2	2	2	NaN
	Mean	2.3118	8.2985	7.2745	4.3644	2.7457	NaN
	SD	0.7499	10.6385	7.9679	4.9355	0.9575	NaN

Table A.10.1: DI_{bound} calculated for condition of functional block for patients undergoing extra-stimuli experiment.

Appendix 11

Fast Na^+ current (I_{Na}):

$$m_\infty = \frac{1}{1+\exp\left(\frac{-(V+39.57)}{9.871}\right)} \tag{A.11.1}$$

$$\tau_m = \frac{1}{6.765\cdot\exp\left(\frac{V+11.64}{34.77}\right)+8.552\cdot\exp\left(\frac{-(V+77.42)}{5.955}\right)} \tag{A.11.2}$$

$$\frac{dm}{dt} = \frac{m_\infty - m}{\tau_m} \tag{A.11.3}$$

$$h_\infty = \frac{1}{1+\exp\left(\frac{V+82.9}{6.086}\right)} \tag{A.11.4}$$

$$\tau_{h,fast} = \frac{1}{1.432\cdot10^{-5}\cdot\exp\left(\frac{-(V+1.196)}{6.285}\right)+6.149\cdot\exp\left(\frac{V+0.5096}{20.27}\right)} \tag{A.11.5}$$

$$\tau_{h,slow} = \frac{1}{0.009764\cdot\exp\left(\frac{-(V+17.95)}{28.05}\right)+0.3343\cdot\exp\left(\frac{V+5.730}{56.66}\right)} \tag{A.11.6}$$

$$\frac{dh_{fast}}{dt} = \frac{h_\infty - h_{fast}}{\tau_{h,fast}} \tag{A.11.7}$$

$$\frac{dh_{slow}}{dt} = \frac{h_\infty - h_{slow}}{\tau_{h,slow}} \tag{A.11.8}$$

$$h = A_{h,fast}\cdot h_{fast} + A_{h,slow}\cdot h_{slow} \tag{A.11.9}$$

Where $A_{h,\,fast} = 0.99$, $A_{h,slow} = 0.01$.

$$j_\infty = h_\infty \tag{A.11.10}$$

$$\tau_j = 2.038 + \frac{1}{0.02136 \cdot \exp\left(\frac{-(V+100.6)}{8.281}\right) + 0.3052 \cdot \exp\left(\frac{V+0.9941}{38.45}\right)} \tag{A.11.11}$$

$$\frac{dj}{dt} = \frac{j_\infty - j}{\tau_j} \tag{A.11.12}$$

$$h_{CaMK,\infty} = \frac{1}{1+\exp\left(\frac{V+89.1}{6.086}\right)} \tag{A.11.13}$$

$$\tau_{h,CaMK,slow} = 3 \cdot \tau_{h,slow} \tag{A.11.14}$$

$$\frac{dh_{CaMK,slow}}{dt} = \frac{h_{CaMK,\infty} - h_{CaMK,slow}}{\tau_{h,CaMK,slow}} \tag{A.11.15}$$

$$h_{CaMK} = A_{h,CaMK,\,fast} \cdot h_{CaMK,\,fast} + A_{h,CaMK,slow} \cdot h_{CaMK,slow} \tag{A.11.16}$$

Where $A_{h,CaMK,\,fast} = A_{h,\,fast}$, $A_{h,CaMK,slow} = A_{h,slow}$, $h_{CaMK,\,fast} = h_{fast}$.

$$\frac{dj_{CaMK}}{dt} = \frac{j_{CaMK,\infty} - j_{CaMK}}{\tau_{j,CaMK}} \tag{A.11.17}$$

Where $j_{CaMK,\infty} = j_\infty$, $\tau_{j,CaMK} = 1.46 \cdot \tau_j$.

$$\phi_{INa,CaMK} = \frac{1}{1+\frac{K_{m,CaMK}}{CaMK_{active}}} \tag{A.11.18}$$

Where $K_{m,CaMK} = 0.15$.

$$I_{Na,fast} = \overline{G_{Na,fast}} \cdot (V - E_{Na}) \cdot m^3 \cdot ((1 - \phi_{INa,CaMK}) \cdot h \cdot j + \phi_{INa,CaMK} \cdot h_{CaMK} \cdot j_{CaMK}) \quad \text{(A.11.19)}$$

Where $\overline{G_{Na,fast}} = 75 mS / \mu F$.

$$m_{L,\infty} = \frac{1}{1 + \exp\left(\frac{-(V + 42.85)}{5.264}\right)} \quad \text{(A.11.20)}$$

$$\frac{dm_L}{dt} = \frac{m_{L,\infty} - m_L}{\tau_{m,L}} \quad \text{(A.11.21)}$$

Where $\tau_{m,L} = \tau_m$.

$$h_{L,\infty} = \frac{1}{1 + \exp\left(\frac{V + 87.61}{7.488}\right)} \quad \text{(A.11.22)}$$

$$\frac{dh_L}{dt} = \frac{h_{L,\infty} - h_L}{\tau_{h,L}} \quad \text{(A.11.23)}$$

Where $\tau_{h,L} = 200 ms$.

$$h_{L,CaMK,\infty} = \frac{1}{1 + \exp\left(\frac{V + 93.81}{7.488}\right)} \quad \text{(A.11.24)}$$

$$\frac{dh_{L,CaMK}}{dt} = \frac{h_{L,CaMK,\infty} - h_{L,CaMK}}{\tau_{h,L,CaMK}} \quad \text{(A.11.25)}$$

Where $\tau_{h,L.CaMK} = 3 \cdot \tau_{h,L}$.

$$I_{Na,late} = \overline{G_{Na,late}} \cdot (V - E_{Na}) \cdot m_L \cdot ((1 - \phi_{INa,CaMK}) \cdot h_L + \phi_{INa,CaMK} \cdot h_{L,CaMK}) \quad \text{(A.11.26)}$$

Where $\overline{G_{Na,late}} = 0.0075 mS / \mu F$

$$I_{Na} = I_{Na,\,fast} + I_{Na,late} \tag{A.11.27}$$

Inward rectifier potassium current (I_{K1}):

$$x_{K1,\infty} = \frac{1}{1+\exp\left(-\dfrac{V+2.5538\cdot[K^+]_o+144.59}{1.5692\cdot[K^+]_o+3.8115}\right)} \tag{A.11.28}$$

$$\tau_{x,K1} = \frac{122.2}{\exp\left(\dfrac{-(V+127.2)}{20.36}\right)+\exp\left(\dfrac{V+236.8}{69.33}\right)} \tag{A.11.29}$$

$$\frac{dx_{K1}}{dt} = \frac{x_{K1,\infty}-x_{K1}}{\tau_{x,K1}} \tag{A.11.30}$$

$$R_{K1} = \frac{1}{1+\exp\left(\dfrac{V+105.8-2.6\cdot[K^+]_o}{9.493}\right)} \tag{A.11.31}$$

$$I_{K1} = \overline{G_{K1}}\cdot\sqrt{[K^+]_o}\cdot x_{K1}\cdot R_{K1}\cdot(V-E_K) \tag{A.11.32}$$

Where $\overline{G_{K1}} = 0.1908$.

Transient outward potassium current (I_{to}):

$$a_\infty = \frac{1}{1+\exp\left(\dfrac{-(V-14.34)}{14.82}\right)} \tag{A.11.33}$$

$$\tau_a = \frac{1.0515}{\frac{1}{1.2089 \cdot \left(1+\exp\left(\frac{-(V-18.41)}{29.38}\right)\right)} + \frac{3.5}{1+\exp\left(\frac{V+100}{29.38}\right)}} \quad \text{(A.11.34)}$$

$$\frac{da}{dt} = \frac{a_\infty - a}{\tau_a} \quad \text{(A.11.35)}$$

$$i_\infty = \frac{1}{1+\exp\left(\frac{V+43.94}{5.711}\right)} \quad \text{(A.11.36)}$$

$$\tau_{i,fast} = 4.562 + \frac{1}{0.3933 \cdot \exp\left(\frac{-(V+100)}{100}\right) + 0.08004 \cdot \exp\left(\frac{V+50}{16.59}\right)} \quad \text{(A.11.37)}$$

$$\tau_{i,slow} = 23.62 + \frac{1}{0.001416 \cdot \exp\left(\frac{-(V+96.52)}{59.05}\right) + 1.7808 \cdot 10^{-8} \cdot \exp\left(\frac{V+114.1}{8.079}\right)} \quad \text{(A.11.38)}$$

$$A_{i,fast} = \frac{1}{1+\exp\left(\frac{V+43.94}{5.711}\right)} \quad \text{(A.11.39)}$$

$$A_{i,slow} = 1 - A_{i,fast} \quad \text{(A.11.40)}$$

$$\frac{di_{fast}}{dt} = \frac{i_\infty - i_{fast}}{\tau_{i,fast}} \quad \text{(A.11.41)}$$

$$\frac{di_{slow}}{dt} = \frac{i_\infty - i_{slow}}{\tau_{i,slow}} \quad \text{(A.11.42)}$$

$$i = A_{i,fast} \cdot i_{fast} + A_{i,slow} \cdot i_{slow} \quad \text{(A.11.43)}$$

$$a_{CaMK,\infty} = \frac{1}{1+\exp\left(\frac{-(V-24.34)}{14.82}\right)} \quad \text{(A.11.44)}$$

$$\tau_{a,CaMK} = \tau_a \tag{A.11.45}$$

$$\frac{da_{CaMK}}{dt} = \frac{a_{CaMK,\infty} - a_{CaMK}}{\tau_{a,CaMK}} \tag{A.11.46}$$

$$i_{CaMK,\infty} = i_{\infty} \tag{A.11.47}$$

$$\delta_{CaMK,develop} = 1.354 + \frac{10^{-4}}{\exp\left(\frac{V-167.4}{15.89}\right) + \exp\left(\frac{-(V-12.23)}{0.2154}\right)} \tag{A.11.48}$$

$$\delta_{CaMK,recover} = 1 - \frac{0.5}{1 + \exp\left(\frac{V+70}{20}\right)} \tag{A.11.49}$$

$$\tau_{i,CaMK,fast} = \tau_{i,fast} \cdot \delta_{CaMK,develop} \cdot \delta_{CaMK,recover} \tag{A.11.50}$$

$$\tau_{i,CaMK,slow} = \tau_{i,slow} \cdot \delta_{CaMK,develop} \cdot \delta_{CaMK,recover} \tag{A.11.51}$$

$$\frac{di_{CaMK,fast}}{dt} = \frac{i_{CaMK,\infty} - i_{CaMK,fast}}{\tau_{i,CaMK,fast}} \tag{A.11.52}$$

$$\frac{di_{CaMK,slow}}{dt} = \frac{i_{CaMK,\infty} - i_{CaMK,slow}}{\tau_{i,CaMK,slow}} \tag{A.11.53}$$

$$i_{CaMK} = A_{i,CaMK,fast} \cdot i_{CaMK,fast} + A_{i,CaMK,slow} \cdot i_{CaMK,slow} \tag{A.11.54}$$

Where $A_{i,CaMK,fast} = A_{i,fast}$, $A_{i,CaMK,slow} = A_{i,slow}$.

$$I_{to} = \overline{G_{to}} \cdot (V - E_K) \cdot \left((1 - \phi_{Ito,CaMK}) \cdot a \cdot i + \phi_{Ito,CaMK} \cdot a_{CaMK} \cdot i_{CaMK}\right) \tag{A.11.55}$$

Where $\overline{G_{to}} = 0.02 mS/\mu F$, $\phi_{Ito,CaMK} = \phi_{INaL,CaMK}$.

Rapid delayed rectifier potassium current (I_{Kr}):

$$x_{r,\infty} = \frac{1}{1+\exp\left(\frac{-(V+8.337)}{6.789}\right)} \quad \text{(A.11.56)}$$

$$\tau_{xr,fast} = 12.98 + \frac{1}{0.3652\cdot\exp\left(\frac{V-31.66}{3.869}\right) + 4.123\cdot10^{-5}\cdot\exp\left(\frac{-(V-47.78)}{20.38}\right)} \quad \text{(A.11.57)}$$

$$\tau_{xr,slow} = 1.865 + \frac{1}{0.06629\cdot\exp\left(\frac{V-34.70}{7.355}\right) + 1.128\cdot10^{-5}\cdot\exp\left(\frac{-(V-29.74)}{25.94}\right)} \quad \text{(A.11.58)}$$

$$A_{xr,fast} = \frac{1}{1+\exp\left(\frac{V+54.81}{38.21}\right)} \quad \text{(A.11.59)}$$

$$A_{xr,slow} = 1 - A_{xr,fast} \quad \text{(A.11.60)}$$

$$\frac{dx_{r,fast}}{dt} = \frac{x_{r,\infty} - x_{r,fast}}{\tau_{xr,fast}} \quad \text{(A.11.61)}$$

$$\frac{dx_{r,slow}}{dt} = \frac{x_{r,\infty} - x_{r,slow}}{\tau_{xr,slow}} \quad \text{(A.11.62)}$$

$$x_r = A_{xr,fast}\cdot x_{r,fast} + A_{xr,slow}\cdot x_{r,slow} \quad \text{(A.11.63)}$$

$$R_{Kr} = \frac{1}{\left(1+\exp\left(\frac{V+55}{75}\right)\cdot\left(1+\exp\left(\frac{V-10}{30}\right)\right)\right)} \quad \text{(A.11.64)}$$

$$I_{Kr} = \overline{G_{Kr}}\cdot\sqrt{\frac{[K^+]_o}{5.4}}\cdot x_r\cdot R_{Kr}\cdot(V-E_K) \quad \text{(A.11.65)}$$

Where $\overline{G_{Kr}} = 0.046 mS/\mu F$.

Slow delayed rectifier potassium current (I_{Ks}):

$$x_{s1,\infty} = \frac{1}{1+\exp\left(\frac{-(V+11.60)}{8.932}\right)} \tag{A.11.66}$$

$$\tau_{x,s1} = 817.3 + \frac{1}{2.326\cdot 10^{-4}\cdot\exp\left(\frac{V+48.28}{17.80}\right)+0.001292\cdot\exp\left(\frac{-(V+210)}{230}\right)} \tag{A.11.67}$$

$$\frac{dx_{s1}}{dt} = \frac{x_{s1,\infty}-x_{s1}}{\tau_{x,s1}} \tag{A.11.68}$$

$$x_{s2,\infty} = x_{s1,\infty} \tag{A.11.69}$$

$$\tau_{x,s2} = \frac{1}{0.01\cdot\exp\left(\frac{V-50}{20}\right)+0.0193\cdot\exp\left(\frac{-(V+66.54)}{31}\right)} \tag{A.11.70}$$

$$\frac{dx_{s2}}{dt} = \frac{x_{s2,\infty}-x_{s2}}{\tau_{x,s2}} \tag{A.11.71}$$

$$I_{Ks} = \overline{G_{Ks}}\cdot\left(1+\frac{0.6}{1+\left(\frac{3.8\cdot 10^{-5}}{[Ca^{2+}]_i}\right)^{1.4}}\right)\cdot x_{s1}\cdot x_{s2}\cdot(V-E_{Ks}) \tag{A.11.72}$$

Where $\overline{G_{Ks}} = 0.0034 mS/\mu F$.

Currents through the L-type calcium channel (I_{CaL} , I_{CaNa} , I_{CaK}):

$$d_\infty = \frac{1}{1+\exp\left(\frac{-(V+3.94)}{4.23}\right)} \quad \text{(A.11.73)}$$

$$\tau_d = 0.6 + \frac{1}{\exp(-0.05\cdot(V+6)) + \exp(0.09\cdot(V+14))} \quad \text{(A.11.74)}$$

$$\frac{dd}{dt} = \frac{d_\infty - d}{\tau_d} \quad \text{(A.11.75)}$$

$$f_\infty = \frac{1}{1+\exp\left(\frac{V-19.58}{3.696}\right)} \quad \text{(A.11.76)}$$

$$\tau_{f,fast} = 7 + \frac{1}{0.0045\cdot\exp\left(\frac{-(V+20)}{10}\right) + 0.0045\cdot\exp\left(\frac{V+20}{10}\right)} \quad \text{(A.11.77)}$$

$$\tau_{f,slow} = 100 + \frac{1}{0.000035\cdot\exp\left(\frac{-(V+5)}{4}\right) + 0.000035\cdot\exp\left(\frac{V+5}{6}\right)} \quad \text{(A.11.78)}$$

$$\frac{df_{fast}}{dt} = \frac{f_\infty - f_{fast}}{\tau_{f,fast}} \quad \text{(A.11.79)}$$

$$\frac{df_{slow}}{dt} = \frac{f_\infty - f_{slow}}{\tau_{f,slow}} \quad \text{(A.11.80)}$$

$$f = A_{f,fast}\cdot f_{fast} + A_{f,slow}\cdot f_{slow} \quad \text{(A.11.81)}$$

Where $A_{f,fast} = 0.6$, $A_{f,slow} = 0.4$

$$\tau_{f,Ca,fast} = 7 + \frac{1}{0.04\cdot\exp\left(\frac{-(V-4)}{7}\right) + 0.04\cdot\exp\left(\frac{V-4}{7}\right)} \quad \text{(A.11.82)}$$

$$\tau_{f,Ca,slow} = 100 + \frac{1}{0.00012 \cdot \exp\left(\frac{-V}{3}\right) + 0.00012 \cdot \exp\left(\frac{V}{7}\right)} \quad \text{(A.11.83)}$$

$$A_{f,Ca,fast} = 0.3 + \frac{0.6}{1 + \exp\left(\frac{V-10}{10}\right)} \quad \text{(A.11.84)}$$

$$A_{f,Ca,slow} = 1 - A_{f,Ca,fast} \quad \text{(A.11.85)}$$

$$\frac{df_{Ca,fast}}{dt} = \frac{f_{Ca,\infty} - f_{Ca,fast}}{\tau_{f,Ca,fast}} \quad \text{(A.11.86)}$$

$$\frac{df_{Ca,slow}}{dt} = \frac{f_{Ca,\infty} - f_{Ca,slow}}{\tau_{f,Ca,slow}} \quad \text{(A.11.87)}$$

$$f_{Ca} = A_{f,Ca,fast} \cdot f_{Ca,fast} + A_{f,Ca,slow} \cdot f_{Ca,slow} \quad \text{(A.11.88)}$$

$$\frac{dj_{Ca}}{dt} = \frac{j_{Ca,\infty} - j_{Ca}}{\tau_{j,Ca}} \quad \text{(A.11.89)}$$

Where $j_{Ca,\infty} = f_{Ca,\infty}$, $\tau_{j,Ca} = 75.0$, $f_{Ca,\infty} = f_{\infty}$.

$$\frac{df_{CaMK,fast}}{dt} = \frac{f_{CaMK,\infty} - f_{CaMK,fast}}{\tau_{f,CaMK,fast}} \quad \text{(A.11.90)}$$

Where $f_{CaMK,\infty} = f_{\infty}$, $\tau_{f,CaMK,fast} = 2.5 \cdot \tau_{f,fast}$.

$$f_{CaMK} = A_{f,CaMK,fast} \cdot f_{CaMK,fast} + A_{f,CaMK,slow} \cdot f_{CaMK,slow} \quad \text{(A.11.91)}$$

Where $A_{f,CaMK,fast} = A_{f,fast}$, $A_{f,CaMK,slow} = A_{f,slow}$, $f_{CaMK,slow} = f_{slow}$.

$$\frac{df_{Ca,CaMK,fast}}{dt} = \frac{f_{Ca,CaMK,\infty} - f_{Ca,CaMK,fast}}{\tau_{f,Ca,CaMK,fast}} \quad \text{(A.11.92)}$$

$$f_{Ca,CaMK} = A_{f,Ca,CaMK,fast} \cdot f_{Ca,CaMK,fast} + A_{f,Ca,CaMK,slow} \cdot f_{Ca,CaMK,slow} \quad \text{(A.11.93)}$$

Where $A_{f,Ca,CaMK,fast} = A_{f,Ca,fast}$, $A_{f,Ca,CaMK,slow} = A_{f,Ca,slow}$, $f_{Ca,CaMK,slow} = f_{Ca,slow}$, $\tau_{f,Ca,CaMK,fast} = 2.5 \cdot \tau_{f,Ca,fast}$.

$$\alpha_n = \frac{1}{\frac{k_{+2,n}}{k_{-2,n}} + \left(1 + \frac{K_{m,n}}{[Ca^{2+}]_{ss}}\right)^4} \quad \text{(A.11.94)}$$

Where $k_{+2,n} = 1000$, $k_{-2,n} = j_{Ca}$, $K_{m,n} = 0.002$.

$$\frac{dn}{dt} = \alpha_n \cdot k_{+2,n} - n \cdot k_{-2,n} \quad \text{(A.11.95)}$$

$$\Psi_{Ca} = z_{Ca}^{\ 2} \cdot \frac{VF^2}{RT} \cdot \frac{\gamma_{Cai} \cdot [Ca^{2+}]_{ss} \cdot \exp\left(\frac{z_{Ca} VF}{RT}\right) - \gamma_{Cao} \cdot [Ca^{2+}]_o}{\exp\left(\frac{z_{Ca} VF}{RT}\right) - 1} \quad \text{(A.11.96)}$$

$$\overline{I_{CaL}} = P_{Ca} \cdot \Psi_{Ca} \quad \text{(A.11.97)}$$

Where $P_{Ca} = 0.0001 cm/s$, $\gamma_{Cai} = 1$, $\gamma_{Cao} = 0.341$, $z_{Ca} = 2$.

$$\Psi_{CaNa} = z_{Na}^{\ 2} \cdot \frac{VF^2}{RT} \cdot \frac{\gamma_{Nai} \cdot [Na^{+}]_{ss} \cdot \exp\left(\frac{z_{Na} VF}{RT}\right) - \gamma_{Nao} \cdot [Na^{+}]_o}{\exp\left(\frac{z_{Na} VF}{RT}\right) - 1} \quad \text{(A.11.98)}$$

$$\overline{I_{CaNa}} = P_{CaNa} \cdot \Psi_{CaNa} \quad \text{(A.11.99)}$$

Where $P_{CaNa} = 0.00125 \cdot P_{Ca}$, $\gamma_{Nai} = 0.75$, $\gamma_{Nao} = 0.75$, $z_{Na} = 1$.

$$\Psi_{CaK} = z_{K}^{\ 2} \cdot \frac{VF^2}{RT} \cdot \frac{\gamma_{Ki} \cdot [K^{+}]_{ss} \cdot \exp\left(\frac{z_{K} VF}{RT}\right) - \gamma_{Ko} \cdot [K^{+}]_o}{\exp\left(\frac{z_{K} VF}{RT}\right) - 1} \quad \text{(A.11.100)}$$

$$\overline{I_{CaK}} = P_{CaK} \cdot \Psi_{CaK} \quad \text{(A.11.101)}$$

Where $P_{CaK} = 3.574 \cdot 10^{-4} \cdot P_{Ca}$, $\gamma_{Ki} = 0.75$, $\gamma_{Ko} = 0.75$, $z_K = 1$.

$$\overline{I_{CaL,CaMK}} = P_{Ca,CaMK} \cdot \Psi_{Ca} \quad \text{(A.11.102)}$$

$$\overline{I_{CaNa,CaMK}} = P_{CaNa,CaMK} \cdot \Psi_{CaNa} \quad \text{(A.11.103)}$$

$$\overline{I_{CaK,CaMK}} = P_{CaK,CaMK} \cdot \Psi_{CaK} \quad \text{(A.11.104)}$$

Where $P_{Ca,CaMK} = 1.1 \cdot P_{Ca}$, $P_{CaNa,CaMK} = 0.00125 \cdot P_{Ca,CaMK}$, $P_{CaK,CaMK} = 3.574 \cdot 10^{-4} \cdot P_{Ca,CaMK}$.

$$I_{CaL} = \overline{I_{CaL}} \cdot d \cdot (1 - \phi_{ICaL,CaMK}) \cdot (f \cdot (1-n) + f_{Ca} \cdot n \cdot j_{Ca}) + \overline{I_{CaL,CaMK}} \cdot d \cdot \phi_{ICaL,CaMK} \cdot (f_{CaMK} \cdot (1-n) + f_{Ca,CaMK} \cdot n \cdot j_{Ca}) \quad \text{(A.11.105)}$$

$$I_{CaNa} = \overline{I_{CaNa}} \cdot d \cdot (1 - \phi_{ICaL,CaMK}) \cdot (f \cdot (1-n) + f_{Ca} \cdot n \cdot j_{Ca}) + \overline{I_{CaNa,CaMK}} \cdot d \cdot \phi_{ICaL,CaMK} \cdot (f_{CaMK} \cdot (1-n) + f_{Ca,CaMK} \cdot n \cdot j_{Ca}) \quad \text{(A.11.106)}$$

$$I_{CaK} = \overline{I_{CaK}} \cdot d \cdot (1 - \phi_{ICaL,CaMK}) \cdot (f \cdot (1-n) + f_{Ca} \cdot n \cdot j_{Ca}) + \overline{I_{CaK,CaMK}} \cdot d \cdot \phi_{ICaL,CaMK} \cdot (f_{CaMK} \cdot (1-n) + f_{Ca,CaMK} \cdot n \cdot j_{Ca}) \quad \text{(A.11.107)}$$

Where $\phi_{ICaL,CaMK} = \phi_{INaL,CaMK}$.

Sodium/Calcium exchange current (I_{NaCa}):

For $Y \in \{i, ss\}$

$$h_{Ca} = \exp\left(\frac{0.5224VF}{RT}\right) \quad \text{(A.11.108)}$$

$$h_{Na} = \exp\left(\frac{0.167VF}{RT}\right) \quad \text{(A.11.109)}$$

$$h_1 = 1 + \frac{[Na^+]_Y}{k_{Na3}}(1 + h_{Na}) \quad \text{(A.11.110)}$$

$$h_2 = \frac{[Na^+]_Y \cdot h_{Na}}{k_{Na3} \cdot h_1} \quad \text{(A.11.111)}$$

$$h_3 = \frac{1}{h_1} \quad \text{(A.11.112)}$$

$$h_4 = 1 + \frac{[Na^+]_Y}{k_{Na1}}\left(1 + \frac{[Na^+]_Y}{k_{Na2}}\right) \quad \text{(A.11.113)}$$

$$h_5 = \frac{[Na^+]_Y{}^2}{h_4 \cdot k_{Na1} \cdot k_{Na2}} \quad \text{(A.11.114)}$$

$$h_6 = \frac{1}{h_4} \quad \text{(A.11.115)}$$

$$h_7 = 1 + \frac{[Na^+]_o}{k_{Na3}}\left(1 + \frac{1}{h_{Na}}\right) \quad \text{(A.11.116)}$$

$$h_8 = \frac{[Na^+]_o}{k_{Na3} \cdot h_{Na} \cdot h_7} \quad \text{(A.11.117)}$$

$$h_9 = \frac{1}{h_7} \quad \text{(A.11.118)}$$

$$h_{10} = k_{asymm} + 1 + \frac{[Na^+]_o}{k_{Na1}}\left(1 + \frac{[Na^+]_o}{k_{Na2}}\right) \quad \text{(A.11.119)}$$

$$h_{11} = \frac{[Na^+]_o{}^2}{h_{10} \cdot k_{Na1} \cdot k_{Na2}} \quad \text{(A.11.120)}$$

$$h_{12} = \frac{1}{h_{10}} \tag{A.11.121}$$

$$k_1 = h_{12} \cdot [Ca^{2+}]_o \cdot k_{Ca,on} \tag{A.11.122}$$

$$k_2 = k_{Ca,off} \tag{A.11.123}$$

$$k_3 = h_9 \cdot \omega_{Ca} + h_8 \cdot \omega_{NaCa} \tag{A.11.124}$$

$$k_4 = \frac{h_3 \cdot \omega_{Ca}}{h_{Ca}} + h_2 \cdot \omega_{NaCa} \tag{A.11.125}$$

$$k_5 = k_{Ca,off} \tag{A.11.126}$$

$$k_6 = h_6 \cdot [Ca^{2+}]_Y \cdot k_{Ca,on} \tag{A.11.127}$$

$$k_7 = h_5 \cdot h_2 \cdot \omega_{Na} \tag{A.11.128}$$

$$k_8 = h_8 \cdot h_{11} \cdot \omega_{Na} \tag{A.11.129}$$

$$x_1 = k_2 \cdot k_7 \cdot (k_7 + k_6) + k_5 \cdot k_7 \cdot (k_2 + k_3) \tag{A.11.130}$$

$$x_2 = k_1 \cdot k_7 \cdot (k_4 + k_5) + k_4 \cdot k_6 \cdot (k_1 + k_8) \tag{A.11.131}$$

$$x_3 = k_1 \cdot k_3 \cdot (k_7 + k_6) + k_6 \cdot k_8 \cdot (k_2 + k_3) \tag{A.11.132}$$

$$x_4 = k_2 \cdot k_8 \cdot (k_4 + k_5) + k_3 \cdot k_5 \cdot (k_1 + k_8) \tag{A.11.133}$$

$$E_1 = \frac{x_1}{x_1 + x_2 + x_3 + x_4} \tag{A.11.134}$$

$$E_2 = \frac{x_2}{x_1 + x_2 + x_3 + x_4} \tag{A.11.135}$$

$$E_3 = \frac{x_3}{x_1 + x_2 + x_3 + x_4} \quad \text{(A.11.136)}$$

$$E_4 = \frac{x_4}{x_1 + x_2 + x_3 + x_4} \quad \text{(A.11.137)}$$

$$allo_Y = \frac{1}{1 + \left(\frac{K_{mCaAct}}{[Ca^{2+}]_Y} \right)^2} \quad \text{(A.11.138)}$$

$$J_{NaCa,Na,Y} = 3 \cdot (E_4 \cdot k_7 - E_1 \cdot k_8) + E_3 \cdot h_2 \cdot \omega_{NaCa} - E_2 \cdot h_8 \cdot \omega_{NaCa} \quad \text{(A.11.139)}$$

$$J_{NaCa,Ca,Y} = E_2 \cdot k_2 - E_1 \cdot k_1 \quad \text{(A.11.140)}$$

$$I_{NaCa,i} = \overline{G_{NaCa}} \cdot 0.8 \cdot allo_i \cdot (J_{NaCa,Na,i} + 2 \cdot J_{NaCa,Ca,i}) \quad \text{(A.11.141)}$$

$$I_{NaCa,ss} = \overline{G_{NaCa}} \cdot 0.2 \cdot allo_{ss} \cdot (J_{NaCa,Na,ss} + 2 \cdot J_{NaCa,Ca,ss}) \quad \text{(A.11.142)}$$

$$I_{NaCa} = I_{NaCa,i} + I_{NaCa,ss} \quad \text{(A.11.143)}$$

Where $K_{Na1} = 15mM$, $K_{Na2} = 5mM$, $K_{Na3} = 88.12mM$, $K_{asymm} = 12.5$, $\omega_{Na} = 6 \cdot 10^4 Hz$, $\omega_{Ca} = 6 \cdot 10^4 Hz$, $\omega_{NaCa} = 5 \cdot 10^3 Hz$, $q_{Na} = 0.5224$, $q_{Ca} = 0.1670$, $\overline{G_{NaCa}} = 0.0008$.

Sodium/potassium ATPase current (I_{NaK}):

$$K_{Nai} = K_{Nai}^o \cdot \exp\left(\frac{\Delta \cdot V \cdot F}{3 \cdot R \cdot T} \right) \quad \text{(A.11.144)}$$

$$K_{Nao} = K_{Nao}^o \cdot \exp\left(\frac{(1 - \Delta) \cdot V \cdot F}{3 \cdot R \cdot T} \right) \quad \text{(A.11.145)}$$

$$[P] = \frac{[\Sigma P]}{1 + \frac{[H^+]}{K_{H,P}} + \frac{[Na^+]_i}{K_{Na,P}} + \frac{[K^+]_i}{K_{K,P}}} \tag{A.11.146}$$

$$\alpha_1 = \frac{k_1^+ \left(\frac{[Na^+]_i}{K_{Nai}} \right)^3}{\left(1 + \frac{[Na^+]_i}{K_{Nai}} \right)^3 + \left(1 + \frac{[K^+]_i}{K_{Ki}} \right)^2 - 1} \tag{A.11.147}$$

$$\beta_1 = k_1^- \cdot [MgADP] \tag{A.11.148}$$

$$\alpha_2 = k_2^+ \tag{A.11.149}$$

$$\beta_2 = \frac{k_2^- \left(\frac{[Na^+]_o}{K_{Nao}} \right)^3}{\left(1 + \frac{[Na^+]_o}{K_{Nao}} \right)^3 + \left(1 + \frac{[K^+]_o}{K_{Ko}} \right)^2 - 1} \tag{A.11.150}$$

$$\alpha_3 = \frac{k_3^+ \left(\frac{[K^+]_o}{K_{Ko}} \right)^2}{\left(1 + \frac{[Na^+]_o}{K_{Nao}} \right)^3 + \left(1 + \frac{[K^+]_o}{K_{Ko}} \right)^2 - 1} \tag{A.11.151}$$

$$\beta_3 = \frac{k_3^- \cdot [P] \cdot [H^+]}{1 + \frac{[MgATP]}{K_{MgATP}}} \tag{A.11.152}$$

$$\alpha_4 = \frac{k_4^+ \cdot \frac{[MgATP]}{K_{MgATP}}}{1 + \frac{[MgATP]}{K_{MgATP}}} \tag{A.11.153}$$

$$\beta_4 = \frac{k_4^- \left(\frac{[K^+]_i}{K_{Ki}} \right)^2}{\left(1 + \frac{[Na^+]_i}{K_{Nai}} \right)^3 + \left(1 + \frac{[K^+]_i}{K_{Ki}} \right)^2 - 1} \quad \text{(A.11.154)}$$

$$x_1 = \alpha_1 \cdot \alpha_2 \cdot \alpha_4 + \beta_2 \cdot \beta_3 \cdot \beta_4 + \alpha_2 \cdot \beta_3 \cdot \beta_4 + \alpha_1 \cdot \alpha_2 \cdot \beta_3 \quad \text{(A.11.155)}$$

$$x_2 = \beta_1 \cdot \beta_2 \cdot \beta_4 + \alpha_1 \cdot \alpha_2 \cdot \alpha_3 + \alpha_3 \cdot \beta_1 \cdot \beta_4 + \alpha_2 \cdot \alpha_3 \cdot \beta_4 \quad \text{(A.11.156)}$$

$$x_3 = \alpha_2 \cdot \alpha_3 \cdot \alpha_4 + \beta_1 \cdot \beta_2 \cdot \beta_3 + \beta_1 \cdot \beta_2 \cdot \alpha_4 + \alpha_3 \cdot \alpha_4 \cdot \beta_1 \quad \text{(A.11.157)}$$

$$x_4 = \beta_2 \cdot \beta_3 \cdot \beta_4 + \alpha_1 \cdot \alpha_3 \cdot \alpha_4 + \alpha_1 \cdot \alpha_4 \cdot \beta_2 + \alpha_1 \cdot \beta_2 \cdot \beta_3 \quad \text{(A.11.158)}$$

$$E_1 = \frac{x_1}{x_1 + x_2 + x_3 + x_4} \quad \text{(A.11.159)}$$

$$E_2 = \frac{x_2}{x_1 + x_2 + x_3 + x_4} \quad \text{(A.11.160)}$$

$$E_3 = \frac{x_3}{x_1 + x_2 + x_3 + x_4} \quad \text{(A.11.161)}$$

$$E_4 = \frac{x_4}{x_1 + x_2 + x_3 + x_4} \quad \text{(A.11.162)}$$

$$J_{NaK,Na} = 3 \cdot (E_1 \cdot \alpha_3 - E_2 \cdot \beta_3) \quad \text{(A.11.163)}$$

$$J_{NaK,K} = 2 \cdot (E_4 \cdot \beta_1 - E_3 \cdot \alpha_1) \quad \text{(A.11.164)}$$

$$I_{NaK} = 30 \cdot (J_{NaK,Na} + J_{NaK,K}) \quad \text{(A.11.165)}$$

Where $k_1^+ = 949.5Hz$, $k_1^- = 182.4mM^{-1}$, $k_2^+ = 687.2Hz$, $k_2^- = 39.4Hz$, $k_3^+ = 1899Hz$, $k_3^- = 79300Hz \cdot mM^{-2}$, $k_4^+ = 639Hz$, $k_4^- = 40Hz$, $K_{Nai}^o = 9.073mM$,

$K_{Nao}^{o} = 27.78mM$, $\Delta = -0.155$, $K_{Ki} = 0.5mM$, $K_{Ko} = 0.3582mM$, $[MgADP] = 0.05$, $[MgATP] = 9.8$, $KMgATP = 1.698 \cdot 10^{-7} mM$, $[H^{+}] = 10^{-7} mM$, $[\Sigma P] = 4.2mM$, $K_{H,P} = 1.698 \cdot 10^{-7} mM$, $K_{Na,P} = 224mM$, $K_{K,P} = 292mM$.

Background currents (I_{Nab} , I_{Cab} , I_{Kb}) and sarcolemmal calcium pump current (I_{pCa}):

$$I_{Nab} = P_{Nab} \cdot z_{Na}{}^{2} \cdot \frac{VF^{2}}{RT} \cdot \frac{[Na^{+}]_{i} \cdot \exp\left(\frac{z_{Na}VF}{RT}\right) - [Na^{+}]_{o}}{\exp\left(\frac{z_{Na}VF}{RT}\right) - 1} \quad \text{(A.11.166)}$$

Where $P_{Nab} = 3.75 \cdot 10^{-10} cm/s$, $z_{Na} = 1$.

$$I_{Cab} = P_{Cab} \cdot z_{Ca}{}^{2} \cdot \frac{VF^{2}}{RT} \cdot \frac{\gamma_{Cai} \cdot [Ca^{2+}]_{i} \cdot \exp\left(\frac{z_{Ca}VF}{RT}\right) - \gamma_{Cao} \cdot [Ca^{2+}]_{o}}{\exp\left(\frac{z_{Ca}VF}{RT}\right) - 1} \quad \text{(A.11.167)}$$

Where $P_{Cab} = 2.5 \cdot 10^{-8} cm/s$, $\gamma_{Cai} = 1$, $\gamma_{Cao} = 0.341$, $z_{Ca} = 2$.

$$x_{Kb} = \frac{1}{1 + \exp\left(\frac{-(V - 14.48)}{18.34}\right)} \quad \text{(A.11.168)}$$

$$I_{Kb} = G_{Kb} \cdot x_{Kb} \cdot (V - E_{K}) \quad \text{(A.11.169)}$$

$$I_{pCa} = G_{pCa} \cdot \frac{[Ca^{2+}]_{i}}{0.0005 + [Ca^{2+}]_{i}} \quad \text{(A.11.170)}$$

Where $G_{Kb} = 0.003mS/\mu F$, $G_{pCa} = 0.0005mS/\mu F$.

Calcium/calmodulin-dependent protein kinase ($CaMK$):

$$CaMK_{bound} = CaMK_0 \cdot \frac{1 - CaMK_{trap}}{1 + \frac{K_{mCaM}}{[Ca^{2+}]_{ss}}} \quad \text{(A.11.171)}$$

$$\frac{dCaMK_{trap}}{dt} = \alpha_{CaMK} \cdot CaMK_{bound} \cdot (CaMK_{bound} + CaMK_{trap}) - \beta_{CaMK} \cdot CaMK_{trap} \quad \text{(A.11.172)}$$

$$CaMK_{active} = CaMK_{bound} + CaMK_{trap} \quad \text{(A.11.173)}$$

Diffusion fluxes ($J_{diff,Na}$, $J_{diff,Ca}$, $J_{diff,K}$)

$$J_{diff,Na} = \frac{[Na^+]_{ss} - [Na^+]_i}{\tau_{diff,Na}} \quad \text{(A.11.174)}$$

$$J_{diff,Ca} = \frac{[Ca^{2+}]_{ss} - [Ca^{2+}]_i}{\tau_{diff,Ca}} \quad \text{(A.11.175)}$$

$$J_{diff,K} = \frac{[K^+]_{ss} - [K^+]_i}{\tau_{diff,K}} \quad \text{(A.11.176)}$$

Where $\tau_{diff,Na} = 2ms$, $\tau_{diff,Ca} = 0.2ms$, $\tau_{diff,K} = 2ms$.

SR calcium release flux via Ryanodine receptor (J_{rel}):

$$J_{rel,NP,\infty} = \frac{\alpha_{rel} \cdot (-I_{CaL})}{1 + \left(\frac{1.5}{[Ca^{2+}]_{jsr}} \right)^8} \quad \text{(A.11.177)}$$

$$\tau_{rel,NP} = \frac{\beta_\tau}{1+\left(\frac{0.0123}{[Ca^{2+}]_{jsr}}\right)} \quad \text{(A.11.178)}$$

Where $\tau_{rel,NP} \geq 0.001$, $\beta_\tau = 4.75ms$, $\alpha_{rel} = 0.5 \cdot \beta_\tau$.

$$\frac{dJ_{rel,NP}}{dt} = \frac{J_{rel,NP,\infty} - J_{rel,NP}}{\tau_{rel,NP}} \quad \text{(A.11.179)}$$

$$J_{rel,CaMK,\infty} = \frac{\alpha_{rel,CaMK} \cdot (-I_{CaL})}{1+\left(\frac{1.5}{[Ca^{2+}]_{jsr}}\right)^8} \quad \text{(A.11.180)}$$

$$\tau_{rel,CaMK} = \frac{\beta_{\tau,CaMK}}{1+\left(\frac{0.0123}{[Ca^{2+}]_{jsr}}\right)} \quad \text{(A.11.181)}$$

Where $\tau_{rel,CaMK} \geq 0.001$, $\beta_{\tau,CaMK} = 1.25 \cdot \beta_\tau$, $\alpha_{rel,CaMK} = 0.5 \cdot \beta_{\tau,CaMK}$.

$$\frac{dJ_{rel,CaMK}}{dt} = \frac{J_{rel,CaMK,\infty} - J_{rel,CaMK}}{\tau_{rel,CaMK}} \quad \text{(A.11.182)}$$

$$J_{rel} = (1-\phi_{rel,CaMK}) \cdot J_{rel,NP} + \phi_{rel,CaMK} \cdot J_{rel,CaMK} \quad \text{(A.11.183)}$$

Where $\phi_{rel,CaMK} = \phi_{INaL,CaMK}$.

Calcium uptake via SERCA pump (J_{up}):

$$J_{up,NP} = \frac{0.004375 \cdot [Ca^{2+}]_i}{0.00092 + [Ca^{2+}]_i} \quad \text{(A.11.184)}$$

$$J_{up,CaMK} = (1+\overline{\Delta J_{up,CaMK}}) \cdot \frac{0.004375 \cdot [Ca^{2+}]_i}{0.00092 - \overline{\Delta K_{m,PLB}} + [Ca^{2+}]_i} \quad \text{(A.11.185)}$$

Where $\overline{\Delta K_{m,PLB}} = 0.00017mM$, $\overline{\Delta J_{up,CaMK}} = 1.75$.

$$J_{leak} = \frac{0.0039375 \cdot [Ca^{2+}]_{nsr}}{15} \quad \text{(A.11.186)}$$

$$J_{up} = (1-\phi_{up,CaMK}) \cdot J_{up,NP} + \phi_{up,CaMK} \cdot J_{up,CaMK} - J_{leak} \quad \text{(A.11.187)}$$

Where $\phi_{up,CaMK} = \phi_{INaL,CaMK}$.

Calcium translocation from NSR to JSR (J_{tr}):

$$J_{tr} = \frac{[Ca^{2+}]_{nsr} - [Ca^{2+}]_{jsr}}{\tau_{tr}} \quad \text{(A.11.188)}$$

Where $\tau_{tr} = 100ms$.

Ion concentrations and buffers:

$$\frac{d[Na^+]_i}{dt} = -(I_{Na} + I_{NaL} + 3 \cdot I_{NaCa,i} + 3 \cdot I_{NaK} + I_{Nab}) \cdot \frac{A_{cap}}{F \cdot v_{myo}} + J_{diff,Na} \cdot \frac{v_{ss}}{v_{myo}} \quad \text{(A.11.189)}$$

$$\frac{d[Na^+]_{ss}}{dt} = -(I_{CaNa} + 3 \cdot I_{NaCa,ss}) \cdot \frac{A_{cap}}{F \cdot v_{ss}} - J_{diff,Na} \quad \text{(A.11.190)}$$

$$\frac{d[K^+]_i}{dt} = -(I_{to} + I_{Kr} + I_{Ks} + I_{K1} + I_{Kur} + I_{stim} - 2 \cdot I_{NaK}) \cdot \frac{A_{cap}}{F \cdot v_{myo}} + J_{diff,K} \cdot \frac{v_{ss}}{v_{myo}} \quad \text{(A.11.191)}$$

$$\frac{d[K^+]_{ss}}{dt} = -I_{CaK} \cdot \frac{A_{cap}}{F \cdot v_{ss}} - J_{diff,K} \quad \text{(A.11.192)}$$

$$\beta_{Cai} = \frac{1}{1 + \frac{\overline{[CMDN]} \cdot K_{m,CMDN}}{(K_{m,CMDN} + [Ca^{2+}]_i)^2} + \frac{\overline{[TRPN]} \cdot K_{m,TRPN}}{(K_{m,TRPN} + [Ca^{2+}]_i)^2}} \quad \text{(A.11.193)}$$

$$\frac{d[Ca^{2+}]_i}{dt} = \beta_{Cai} \cdot \left(-(I_{pCa} + I_{Cab} - 2 \cdot I_{NaCa,i}) \cdot \frac{A_{cap}}{2 \cdot F \cdot v_{myo}} - J_{up} \cdot \frac{v_{nsr}}{v_{myo}} + J_{diff,Ca} \cdot \frac{v_{ss}}{v_{myo}} \right) \quad \text{(A.11.194)}$$

$$\beta_{Cass} = \frac{1}{1 + \frac{\overline{[BSR]} \cdot K_{m,BSR}}{(K_{m,BSR} + [Ca^{2+}]_{ss})^2} + \frac{\overline{[BSL]} \cdot K_{m,BSL}}{(K_{m,BSL} + [Ca^{2+}]_{ss})^2}} \quad \text{(A.11.195)}$$

$$\frac{d[Ca^{2+}]_{ss}}{dt} = \beta_{Cass} \cdot \left(-(I_{CaL} - 2 \cdot I_{NaCa,ss}) \cdot \frac{A_{cap}}{2 \cdot F \cdot v_{ss}} + J_{rel} \cdot \frac{v_{jsr}}{v_{ss}} - J_{diff,Ca} \right) \quad \text{(A.11.196)}$$

$$\frac{d[Ca^{2+}]_{nsr}}{dt} = J_{up} - J_{tr} \cdot \frac{v_{jsr}}{v_{nsr}} \quad \text{(A.11.197)}$$

$$\beta_{Cajsr} = \frac{1}{1 + \frac{\overline{[CSQN]} \cdot K_{m,CSQN}}{(K_{m,CSQN} + [Ca^{2+}]_{jsr})^2}} \quad \text{(A.11.198)}$$

$$\frac{d[Ca^{2+}]_{jsr}}{dt} = \beta_{Cajsr} \cdot (J_{tr} - J_{rel}) \quad \text{(A.11.199)}$$

Where $\overline{[CMDN]} = 0.05mM$, $K_{m,CMDN} = 0.00238mM$, $\overline{[TRPN]} = 0.07mM$, $K_{m,TRPN} = 0.0005mM$, $\overline{[BSR]} = 0.047mM$, $K_{m,BSR} = 0.00087mM$, $\overline{[BSL]} = 1.124mM$, $K_{m,BSL} = 0.0087mM$, $\overline{[CSQN]} = 10mM$, $K_{m,CSQN} = 0.8mM$.

Cell geometry (approximated by a cylinder):

$L = 0.01cm$, $r = 0.0011cm$, $v_{cell} = 3.8 \cdot 10^{-5} \mu L$, $A_{geo} = 7.67 \cdot 10^{-5} cm^2$,

$A_{cap} = 1.534 \cdot 10^{-4} cm^2$, $v_{myo} = 2.584 \cdot 10^{-5} \mu L$, $v_{nsr} = 2.098 \cdot 10^{-6} \mu L$,

$v_{jsr} = 1.82 \cdot 10^{-7} \mu L$, $v_{ss} = 7.6 \cdot 10^{-7} \mu L$

V	-87.84mV	$[Na^+]_i$	7.23mM	$[Na^+]_{ss}$	7.23Mm
$[K^+]_i$	143.79mM	$[K^+]_{ss}$	143.79mM	$[Ca^{2+}]_i$	$8.54 \cdot 10^{-5}$mM
$[Ca^{2+}]_{ss}$	$8.43 \cdot 10^{-5}$mM	$[Ca^{2+}]_{nsr}$	1.61mM	$[Ca^{2+}]_{jsr}$	1.56mM
m	0.0074621	h_{fast}	0.692591	h_{slow}	0.692574
j	0.692574	$h_{CaMK,slow}$	0.448501	j_{CaMK}	0.692413
m_L	0.000194015	h_L	0.496116	$h_{L,CaMK}$	0.265885
a	0.00101185	i_{fast}	0.999542	i_{slow}	0.589579
a_{CaMK}	0.000515567	$i_{CaMK,fast}$	0.999542	$i_{CaMK,slow}$	0.641861
d	$2.43015 \cdot 10^{-9}$	f_{fast}	1	f_{slow}	0.910671
$f_{Ca,fast}$	1	$f_{Ca,slow}$	0.99982	j_{Ca}	0.999977
n	0.00267171	$f_{CaMK,fast}$	1	$f_{Ca,CaMK,fast}$	1
$x_{r,fast}$	$8.26608 \cdot 10^{-6}$	$x_{r,slow}$	0.453268	x_{s1}	0.270492
x_{s2}	0.0001963	x_{K1}	0.996801	$J_{rel,NP}$	$2.53943 \cdot 10^{-5}$mM/ms
$J_{rel,CaMK}$	$3.17262 \cdot 10^{-7}$mM/ms	$CaMK_{trap}$	0.0124065		

Table A.11.1: initial conditions for state variables in human ventricular ionic model.

Initial conditions for variables in the human ventricular ionic model are shown in table A.11.1 (41 state variables). Besides, the external ionic concentrations are defined as bellow:

$$[Na^+]_o = 140mM,\ [Ca^{2+}]_o = 1.8mM,\ [K^+]_o = 5.4mM$$

The amplitude of the external stimulus is defined as -80 $\mu A/\mu F$, the duration of the stimulus is defined to be 0.5ms.

Appendix 12

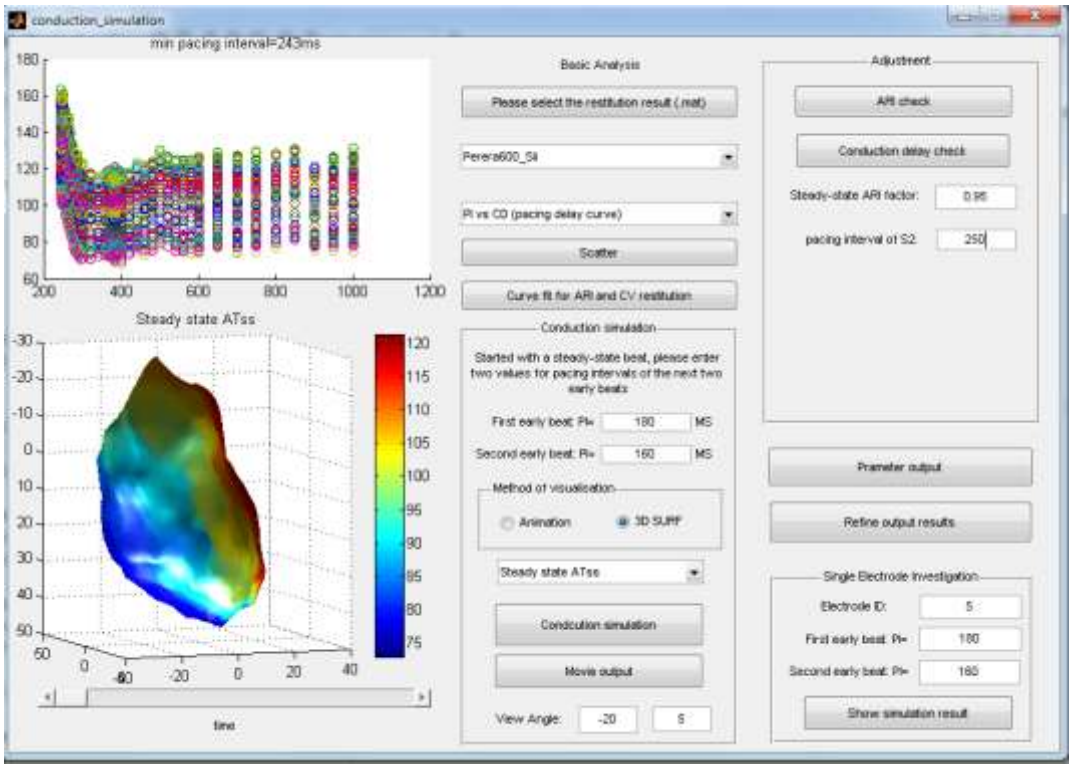

Figure A.12.1: Software designed for the study of interactions of restitution properties.

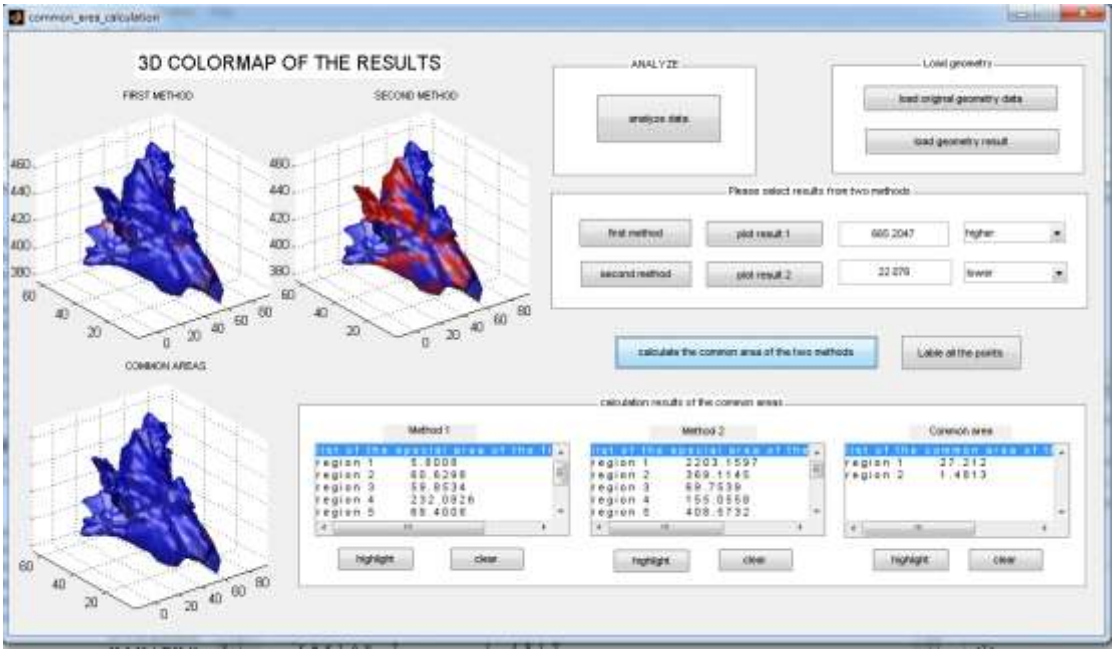

Figure A.12.2: Software designed for Atrial Fibrillation studies (common area identification between two different analyzing methods)

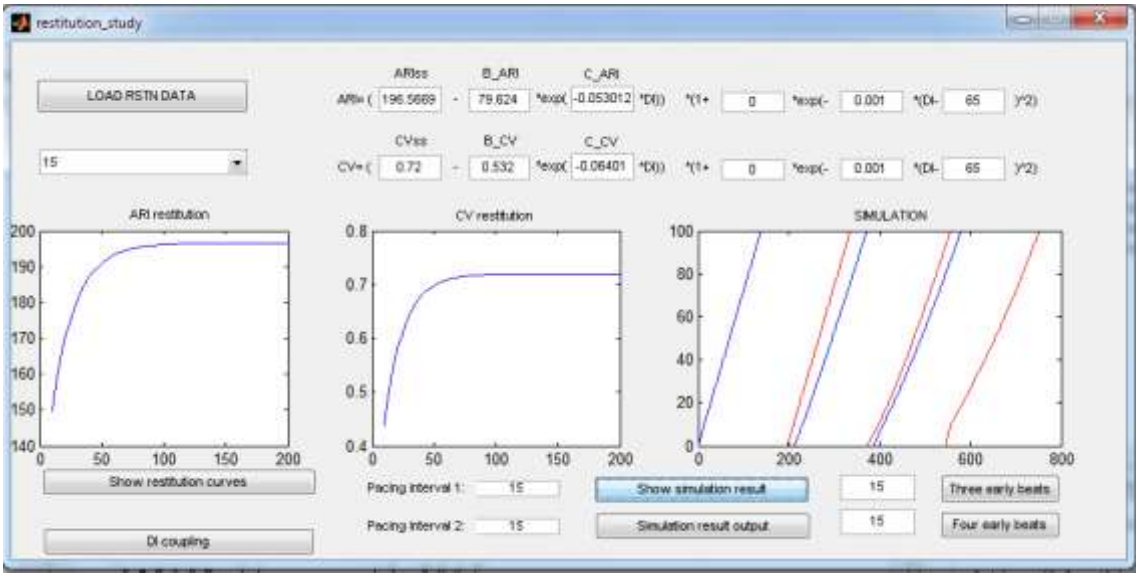

Figure A.12.3: Software designed for restitution studies (simulation of interactions of restitution properties, multi premature beats simulation)

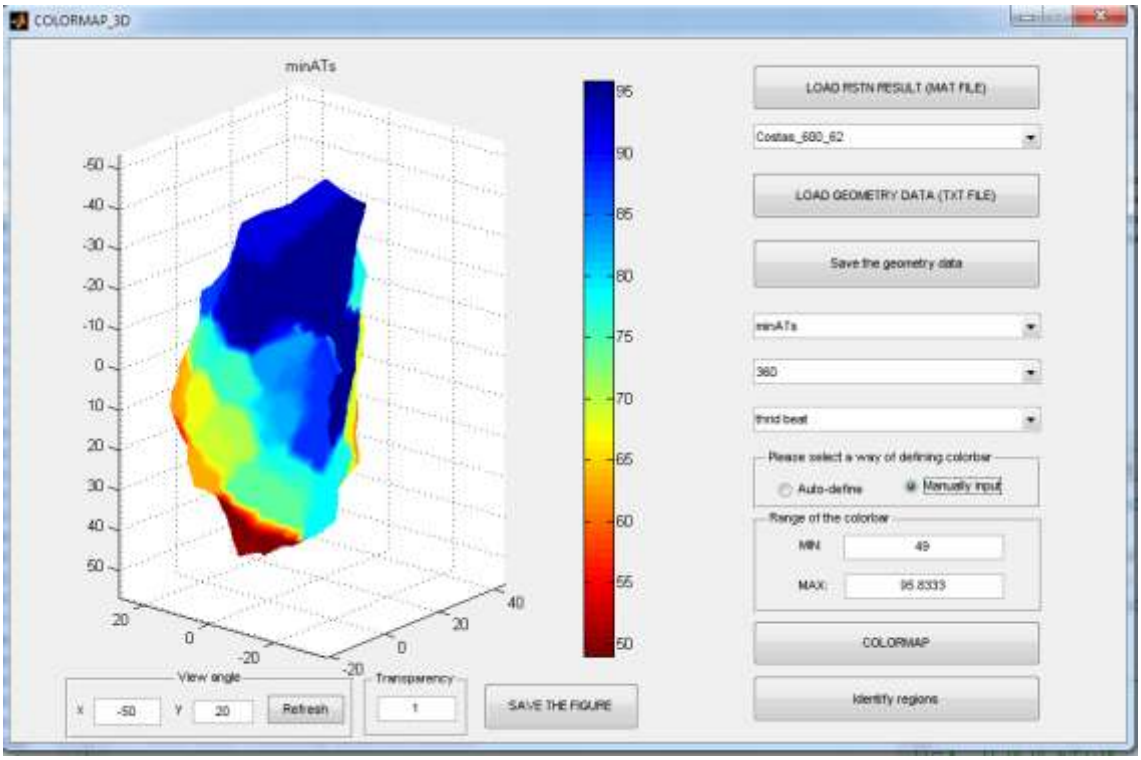

Figure A.12.4 Software designed for three-dimensional visualization

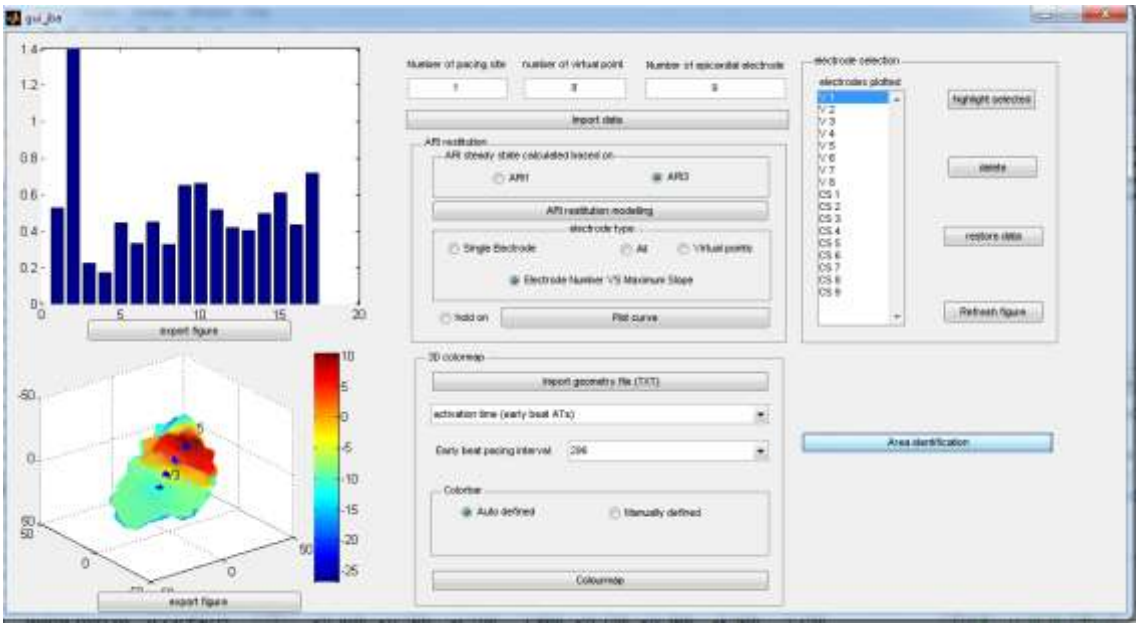

Figure A.12.5: Software designed for restitution property studies (APD restitution properties)